Study of Magnetic, Ferroelectric and Magnetoelectric properties in bulk and nanostructured Multiferroics

Thesis submitted for the degree of

Doctor of Philosophy (Science)

in

Physics (Experimental)

by

Rajasree Das

Department of Physics

University of Calcutta

Kolkata, India

SEPTEMBER 2013

To

My Grandmother, Lily Samaddar

... you say it best when you say nothing at all...

Acknowledgments

This four years I have spent at S N Bose National Centre for Basic Science, Kolkata, is the source of most valued experiences of my life. I take this opportunity to express my gratitude to all who have directly and indirectly helped me through this journey in my acknowledgment. Though it's very very tough to express my gratitude to all my close ones within 2-3 pages, I would like to mention about few people without whom I would never have been able to finish my dissertation.

I owe my deepest gratitude to my supervisor Prof. Kalyan Mandal for his expert advice and unparalleled guidance from the initial stage of this research. His wide knowledge and logical way of thinking have been of great value for me. Above all he provided me with constant encouragement and support. He has been as excellent mentor throughout the work and it would have not been possible for me to bring out this thesis without his help.

A part of my thesis work involved measurements which were taken at IOP Bhubaneswar, CGCRI, Kolkata and IISER, Kolkata. I am grateful to Prof Sikha Verma, A. Sen and Goutam Dev Mukherjee for their help in the measurements. Dr. Satya Prakash Pati has helped me a lot to do Mossbauer measurements of my samples.

A large part of this thesis work would not have been possible without the active involvement of Gogo da (Dr. Gobinda Gopal Khan). My collaboration with him started in a most fortuitous manner. I was discussing about some problem, I was facing to prepare my samples that time and he turned our light conversation into a concrete experimental proposal. Working with him was always a pleasure. One can spend a full month to listen his travel stories. Always wanted to go for a trek with him but unfortunately it's still a dream. He has fascinated me with his vast knowledge in physics. We share common hobbies like photography, travel and reading book. I will be always confused which side of his I admire most; Gogo da as a researcher or Gogo da as a charming friend.

I had the privilege to work with the very talented and charming group-mates, Madhuri di, Bipul da, Debu da, Arka da, Shyam, Debasish, Ashu, Arup, Rupali and Monalisa. Madhuri di has always amused me with her understanding in sample preparation. Arka Da has been an invaluable help throughout my PhD life. After he finished his PhD in SNB, I missed his presence in the lab not only for our discussion on Bismuth ferrite but because of his awesome singing voice with a very cheerful expression. I have always admired the dedication of Shyam towards work. Arup and Ashu are very enthusiastic juniors, always happy to help. Rupali and Monalisa are adorable with their sweet smiling face. I am extremely thankful to all of you for your kind supports in the course of my thesis work.

I am grateful to the technical assistants including Piyali, Shakti da, Surojit da, Dipankar, Urmi and Pallav da for helping me in carrying out the experimental characterizations of my samples. I am grateful to all the staff members of our centre for their unconditional support and help in the hour of need. I thank the entire SNB family for making me feel at home and making my stay memorable. I am also thankful to our librarian, Soumen da. I would like to acknowledge the security persons of the centre, they have always greeted me with a friendly smile and a hello every time I came across them. In the first few months of my stay at SNB, I have never imagined that this place is going to be so close to my heart. On this exciting period of my PhD life, I have got the opportunity to meet people from different background and culture. Saikat, Ruma, Debasish, Putul, Soma, Sukla, Arup are my first friends in SNB. Attending classes with them was a real fun. Saikat has always impressed me with his photography skill. I have always enjoyed gossip (about us) with Ruma, Putul, Soma, Anuradha, Tamishra, Sreemoyee. Time flies when we are deeply involved in intense topics like dress, shoes, and bags. I came in touch with a great group of seniors here; few of them will laugh if they hear me calling them senior. Abhinav, managed to attract the attention of all with his singing, dancing and his huge stock of stories about BHU. Though I believe that all the stories are not fully true, I enjoyed those. Rajiv, one of the most simple and charming friend, who kept us entertained all the time. Sandeep (Agarwall) is blessed with the talent to crack the most nonsense joke, no matter what is the situation; his words will either make u laugh or upset. Sing helped me a lot in Reitveld technique and was patient enough to answer all my stupid questions. Debraj da has been always a helping hand and I will miss the discussion about "Game of Thrones" with him. I will definitely miss the tea time with Bipul da. Tukun and Debolina are the cutest and sweetest juniors. Though I came in touch with Shamik while doing TEM measurements, he became a very good friend with the "north-bengal" connection. I have always enjoyed Milan's company. His good collection of shayari can make anyone happy.

Apart from achieving a THE 'Dr.' tag which I will be able to add before my name after few months, I have also got the most wonderful friend, Wasim, from SNB. Things would have never been the same in SNB without our friendship. Thanks for being with me and tolerating my 'ghan ghan' all the time. I must say thanks to you for checking my thesis chapters with such concentration. I know it was the most boring job you have ever done. I have always admired your depth of thinking, honesty and decisions. Though I don't know much about your work but I know you are the brilliant one. I

have learnt some very useful things from your "techaholic" nature. Don't know what I will miss more, may be our walk to the tea stall after dinner. Hope our small fights are not going to end here. We will continue doing the same for rest of our lives with a cup of tea may be not in Dulal da but somewhere else. Now I have written so much for you, don't forget to say nice things about me in your thesis. And finally please don't tease me for my poor english. My hindi has improved a lot because of you but have failed to teach me good english. So keep trying.

Urmi and Mousumi, you two are the blessings in my life. Hostel life of JU is one of the happiest days of my life. If I were ever to do my graduation again, in one condition I will do it if we can have those golden times once more, specially block day night, b'day nights and preparation time before exams. No mater wherever I will go, I will come to Kolkata to see you. You guys are best, love u two. @Arghya da: you are lucky to have the most fabulous girl and @Mainak: U are lucky too, to have the perfect wife in your life.

I would like to take this opportunity to recall few of my childhood friends Payel, Sourit, Chirantan, Piku, Pappu, Anwesha, Shaonlee, Reshmi, Pushpita, Tubul, Bapai, Gadai and Amlan. Their friendship is a boon that my heart will always cherish. I am thankful to my teachers, Kamal da, Sanju da, Runu Da and Amit sir for their constant encouragement to pursue higher studies.

I am lucky to have such a big family with so many cousins all around. My parents always encouraged me to learn as much as I want and to follow my dreams. My baba is the strictest and my ma is the most humble person in the world. My younger brother, Rahul who always tried to behave like a big brother, made my childhood dreamlike. I am really thankful to my in-laws for their support to balance my career and family life. Dada and Boudi have always treated me like a sister. Tupus added an extra flavour in my life. I am really blessed to have such a loving and caring family. How can I forget the new member of my family, Jim. You are the best.

Sometimes words are not enough to express the feeling for a person like dadabhai, Prasun Dutta. We have spent very small time together but never felt that you are far from me. I know I can take your love and care for granted. I have started loving photography after I saw your collection of photos in CTS. You have helped me get on the road to LATEX and provided an experienced ear for my doubts about writing this thesis.

Shamik da has always been my pillar of happiness. You are the most calm and honest

person I have ever known. You have always bear the brunt of my frustration and came up with some great idea to make my mood light. Never said thanks to you before and never want to. Leaving Singapore was a tough decision, I am happy that you were on my side all the time.

Finally, I would like to thank my husband, Subham Banerjee. He was always there cheering me up and stood by me through the good times and bad. I feel motivated and encouraged every time I discussed my work with him. I still laugh remembering the line you said once "cholo amra sabai mile sample banai". May be you have make fun of me the most but you are the most understanding and undemanding people on earth. You have never let me feel the need to think about anything else other than my work. I owe this thesis to you.

.....

(Rajasree Das)

List of Publications

In Journals :

- [†]**R. Das**, G. G. Khan, S. Varma, G. D. Mukherjee and K. Mandal,
"Effect of Quantum Confinement on Optical and Magnetic Properties of Pr-Cr co-doped Bismuth Ferrite Nanowires".
Journal of Physical Chemistry C(accepted).

- [†]**R. Das**, T. Sarkar and K Mandal
"Multiferroic properties of Ba^{2+} and Gd^{3+} co-doped bismuth ferrite: magnetic, ferroelectric and impedance spectroscopic analysis".
Journal of Physics D: Applied Physics, **45**, 455002 (2012).

- [†]G. G. Khan, **R. Das**, N. Mukherjee and K. Mandal.
"Effect of metal doping on highly efficient photovoltaics and switchable photovoltage in bismuth ferrite nanotubes".
Phys. Status Solidi RRL, **6**, 312 (2012).

- [†]**R. Das**, G. G. Khan and K. Mandal,
"Enhanced ferroelectric, magnetoelectric, and magnetic properties in Pr and Cr co-doped $BiFeO_3$ nanotubes fabricated by template assisted route".
Journal of Applied Physics , **111**, 104115 (2012).

- [†]**R. Das** and K. Mandal,
"Magnetic, ferroelectric and magnetoelectric properties of Ba-doped $BiFeO_3$".
Journal of Magnetism and Magnetic Materials , **324**, 19131918 (2012).

- [†]**R. Das** and K. Mandal,
"Effect of Barium substitution on ferroelectric and magnetic properties of Bismuth ferrite".
IEEE Transactions on Magnetics, **47**, 4054 (2011).

- D. Sarkar, M. Mandal, **R. Das** and Kalyan Mandal,
"Fabrication of Biologically Functionalized, Electrically Conducting and Aligned Magnetic Nanoparticles".
IEEE Transactions on Magnetics, **47**, 3163 (2011).

[†]Used for the present thesis

In Proceedings :

- [†]**R. Das**, G. G. Khan and K. Mandal,
  "Pr and Cr co-doped $BiFeO_3$ nanotubes: an advance multiferroic oxide material".
  EPJ Web of Conferences, **40**, 15015 (2013).

In Preparation :

- [†]**R. Das** and K. Mandal,
  "Influence of film thickness on ferroelectric and magnetic properties of $Bi_{0.85}Ba_{0.15}FeO_3$ thin films".

- [†]**R. Das**, S. Sharma and K. Mandal
  "Role of oxygen vacancy on conduction mechanism of Ba doped $BiFeO_3$".

[†]Used for the present thesis

Abstract

In this thesis bulk and nanostructures (thin film, nanotubes and nanowire) of multiferroic $BiFeO_3$ have been synthesized. Structural, magnetic, ferroelectric, thermal, dielectric and magnetodielectric properties of undoped and doped samples are systemically investigated.

$Bi_{1-x}Ba_xFeO_3(0 \leq x \leq 0.25)$ ceramics are prepared by chemical synthesis route. At room temperature, antiferromagnetic $BiFeO_3$ is converted to ferromagnetic on doping Ba. A large change in magnetization is also observed in the doped samples around 370°C which is the Néel Temperature (T_N) of the parent compound, $BiFeO_3$. Another magnetic transition is also observed near 600°C. Spin canting or impurity phase could be a probable reason for the origin of ferromagnetism in both cases. Ferroelectric and magnetic transition of the compounds shift towards higher temperature with Ba-doping concentration. Anomaly in the dielectric constant is also observed near the T_N of $BiFeO_3$. The composition x = 0.15 shows the maximum magnetic moment at room temperature while better fatigue resistance and maximum magnetoelectric coupling are observed for x = 0.20 composition.

Co-doped $BiFeO_3$ ceramics with nonmagnetic Ba and magnetic Gd ion replacing Bi and Fe respectively, are also prepared by chemical synthesis route. Enhanced magnetoelectric coupling is observed in co-doped samples. Distortion in Fe-O octahedra has a significant effect on magnetic properties of the samples. Ferromagnetic signature is found to enhance significantly in the co-doped samples with respect to the only Gd doped sample both at 80 K and 300 K. Co-doped samples show enhanced electric polarization as well as highest resistivity at room temperature which might be due to the reduction of leakage current and oxygen vacancy in the compositions. An interesting correlation between the T_N of $BiFeO_3$ and temperature dependent dielectric constant (ε) is observed in all samples. $Bi_{0.9}Ba_{0.1}Fe_{0.95}Gd_{0.05}O_3$ ceramic possesses maximum coupling between electric dipole and magnetic dipole with an estimated magnetodielectric effect, MD $[(\varepsilon_r(H)\text{-}\varepsilon_r(0))/\varepsilon_r(0)] \sim 380$ at an applied field 6 kOe. Impedance spectroscopy in the frequency range 40-10^7 Hz and temperature within 30°-300°C suggests that grain relaxation is dominant in the samples. Electrical parameters (such as capacitance and resistance) of the grains are determined using real and imaginary part of impedance (Z' and Z'') and electrical modulus (M' and M'') plot. The results of electrical conductivity indicate correlated barrier hopping (CBH) conduction mechanism in the samples.

Multiferroic $BiFeO_3$ and $Bi_{0.85}Ba_{0.15}FeO_3$ thin films are successfully prepared on Si-based substrate by PLD techniques. Ba doped film with thickness 113 nm shows better magnetic, ferroelectric and dielectric properties compare to the undoped $BiFeO_3$ film with thickness 115 nm. The thickness of the doped films is varied from 29 nm to 113 nm by changing the deposition time. The repetition rate of the laser source strongly affects the surface morphology of the synthesized films. Single-phase films, fabricated at 650°C, crystallize into a rhombohedral structure with a random orientation along (110) and $(110)/(1\bar{1}0)$ direction. The surface topography images obtained using an atomic force microscope show that RMS roughness and grain size of the films are strongly influenced by the film thickness. Ba doping improves ferroelectric and magnetic properties significantly. Ba doped films show saturated P-E hysteresis loop. Dense and homogeneous, 113 nm film shows maximum polarization and dielectric properties. Magnetic property can also be controlled by changing the film thickness. Film with thickness ~ 68 nm approximately equal with the wavelength of spin cycloidal structure ($\lambda = 62$-64 nm) of $BiFeO_3$ shows linear magnetization curve. On the other hand, 29 nm film exhibits well saturated M-H curve with a magnetization value ~ 41.1 emu/cm^3.

Arrays of single phase perovskite-type polycrystalline pure, Pr and Cr doped and Pr-Cr co-doped $BiFeO_3$ nanotubes (NTs) (~ 50 nm wall thickness) have been synthesized using simple template assisted wet chemical liquid phase deposition technique. Spontaneous enhancement in the ferroelectricity, magnetoelectricity and ferromagnetic ordering are evidenced in the Pr and Cr co-doped $BiFeO_3$ NTs. Significant increase in the ferroelectric characteristics in co-doped $BiFeO_3$ NTs suggests the lower leakage current due to the reduction of the oxygen vacancies in the structure. Strong magnetoelectric coupling is observed in co-doped $BiFeO_3$ NTs, where the increase of the dielectric constant is noticeable with the increase of the applied magnetic field. Substantial increase in the ferromagnetic signature in the co-doped $BiFeO_3$ NTs is believed to be due to the collapse of the space-modulated spin structure. Enhanced anomalous photovoltaic effects and switchable photovoltage generation in pure and Pr-Cr co-doped $BiFeO_3$ NTs have been also observed. Influence of metal-doping on short circuit current, open circuit voltage, power conversion efficiency and fill factor are investigated. The power conversion efficiency of pure $BiFeO_3$ NTs ($\sim 0.207\%$) is found to be enhanced by several orders of magnitude in comparison with the reported bulk effect. Pr-doped NTs provide highest value of power conversion efficiency ($\sim 0.5\%$).

The effect of the variation of diameter on optical, magnetic and magnetodielectric

properties of the Pr-Cr co-doped $BiFeO_3$ nanowires (NWs) is studied in detail. Pr-Cr co-doped $BiFeO_3$ NWs with different diameters (18, 35, 55, 100, 150 and 250 nm) have been also fabricated by wet chemical template assisted route. The effect of quantum confinement has found to have significant influence on the room-temperature photoluminescence and Raman spectra of the NWs. Interesting blue shift of the band-gap emission is observed in the photoluminescence spectra of the NWs due to quantum confinement. The position and the intensity of the Raman peaks are found to change significantly depending on the variation in the NW diameter. The room-temperature ferromagnetism of the co-doped $BiFeO_3$ NWs increases consistently with the decrease of the diameter of the NWs, because of the suppression of the spiral spin structure and the increase of the uncompensated spins at the NWs surface (as the surface to volume ratio increases with the decrease of the NWs diameter). Strong magnetoelectric coupling is evidenced in the co-doped $BiFeO_3$ NWs with the decrease of the NWs diameter. The tuning of the optical, magnetic and magnetodielectric properties of the doped $BiFeO_3$ NWs appear to be very promising to achieve multifunctionality in a single material.

Contents

List of Figures

List of Tables

1 Introduction

Complex oxides are one of the most appealing research area due to their rich range of properties like ferroelectricity [1, 2, 3], magnetism [4, 5, 6], magnetoresistance [7, 8], superconductivity [9, 10] etc. Ferromagnetic and ferroelectric materials are most studied compared to other complex oxides as their physical properties can be used to develop a wide range to devices, including sensors [11, 12], integrated circuits [13, 14] and data storage memories [15, 16]. But to achieve a rich functional material for the application purpose, it is very important to combine various physical properties in one material as this will provide an extra degree of freedom in the materials.

Ferromagnetism, ferroelectricity, ferrotoroidicity and ferroelasticity are the four basic order parameter in a material. Materials in which more than one order parameter coexist simultaneously are called multiferroics. In the multiferroic family only a few number of compound exhibit magnetic and electric order parameter simultaneously (Fig 1.1), i.e. ferromagnetic (FM) materials exhibit spontaneous magnetization and the spin ordering in the materials can be altered with an application of external electric field. Similarly, ferroelectric (FE) materials posses spontaneous polarization and the ordering of the electrical dipoles in the materials can be controlled by applying magnetic field externally. Initially the co-existence of FM and FE in a single material was thought to be two independent properties. However, in some multiferroic these two properties are coupled

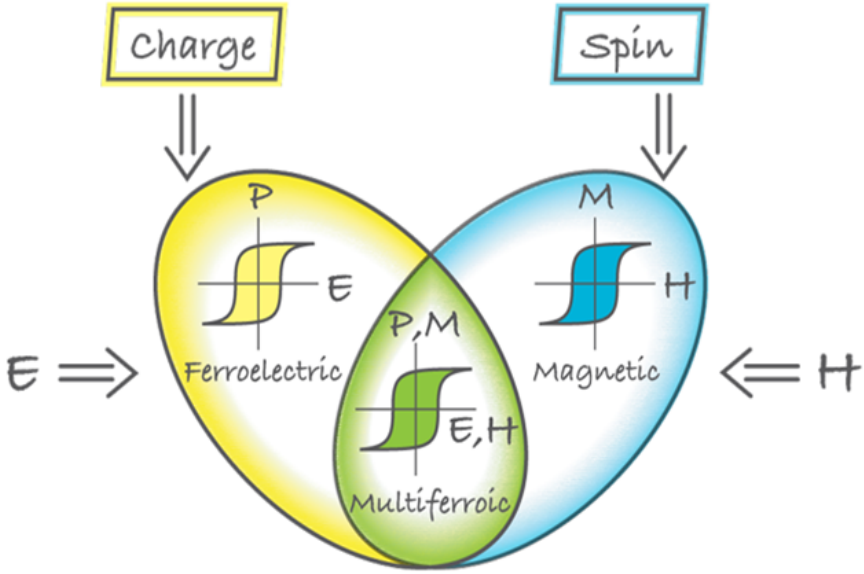

Figure 1.1: Multiferroics combine the properties of ferroelectrics and ferromagnets. In the ideal case, the magnetization of a ferromagnet in a magnetic field displays the usual hysteresis (blue), and ferroelectrics have a similar response to an electric field (yellow). If we manage to create multiferroics that are simultaneously ferromagnetic and ferroelectric (green), then there is a magnetic response to an electric field, or, vice versa, the modification of polarization by magnetic field. And, in principle we have here the basis for making a 4-state logic state: (P+M+), (+-), (-+), (–) [1].

with each other and this coupling interaction produces a promising functionality known as magnetoelectric (ME) effect. This coupling opens a extra degrees of freedom in the materials which enables a control on the magnetic properties by applying an external electric field and vice-versa, providing a possibility to develop new devices based on these materials. So in case of ME multiferroic an electric field not only induces polarization but also changes the spin direction, or magnetic field can control magnetization as well as the polarization.

1.1 A Brief Historical Background

It is well known that electricity and magnetism are intrinsically linked, their coupling was given by the four Maxwell-equations. Though the basic idea that crystals could be simultaneously FM and FE probably proposed by Pierre Curie in the 19th century but the real beginning of this field started in 1959 with a short remark by Landau and Lifshitz in a volume of their Course of Theoretical Physics [17]. But the situation changed drastically when at the same time Dzyaloshinskii predicted [18] time reversal symmetry in Cr_2O_3 and Astrov experimentally confirmed [19] the co-existence of two types of ordering in the same material in 1961. But unfortunately Cr_2O_3 was not suitable for practical use as in this material antiferromagnetism was coupled with paraelectricity. Afterwards, the attempts to combine FM and FE properties started in one material predominantly by two groups in then the Soviet Union: the group of Smolenskii in St. Petersburg (then Leningrad) [20, 21], and by Venevtsev in Moscow [22]. After that, for sometimes, there was no progress in this area of research. The term multiferroic was first used by H. Schmid in 1994 when he observed ferromagnetic ferroelectricity in boracite material [23]. His definition referred to multiferroics as single phase materials which simultaneously possess two or more primary ferroic properties. But boracites were also proved to be impractical material because of the ME coupling at very low temperature and low crystal symmetry in these materials. This finding of a strong ME coupling attracted enormous attention in researches due to both important potential applications and fundamental understanding of material physics. So soon several others multiferroics such as Cr_2O_3, Ti_2O_3, $GaFeO_3$, $PbFe_{0.5}Nb_{0.5}O_3$ etc. were either found in nature [24, 25, 26, 27] or synthesized artificially [28]. An upsurge of interest in these field started with the study on an important perovskite compound Bismuth ferrite ($BiFeO_3$), pioneered by Smolenskii and Chupis [28]. However, ceramic $BiFeO_3$ is too

conductive to be used for any devices and the growth of single crystal $BiFeO_3$ was also very difficult. Many years of research helped people to understand that the existence of oxygen vacancies, defects or mixed valance of Fe are the reason behind conductive properties in $BiFeO_3$. Along with the experimental studies many theoretical observations were also reported asking many questions about different real microscopic mechanisms of FM and FE in $BiFeO_3$. Thus, from the end of the 1990s there is significant progress in synthesis and characterization of high transition temperature multiferroics. Perovskites with the structure ABO_3 have drawn the extensive attention of many groups. Among these compounds some rare earth based materials shows multiferroic properties due to their frustrated structures [29, 30, 31, 32, 33, 34]. Some Bi based compounds like $BiFeO_3$ [35] and $BiMnO_3$ [36] show ME coupling at high temperature. Many review articles have been written on the recent developments, physics behind ME properties and difficulties for processing technologies.

1.2 Magnetoelectric Coupling in Multiferroics

Because ME multiferroics are ordered both magnetically and electrically, the question arises how the two order parameters magnetization (M) and polarization (P) are coupled. In general situations electric and magnetic fields are not intrinsically coupled, though a coupling might appear as a property of certain materials. A simple phenomenological approach to the ME effects is given by Landau- theory, an expansion of the free energy of the fields involved [37]

$$F(E,H) = F_0 - P_i^s E_i - M_i^s H_i - \frac{1}{2}\varepsilon_0\varepsilon_{ij}E_iE_j - \frac{1}{2}\mu_0\mu_{ij}H_iH_j - \alpha_{ij}E_iH_j - ..... \quad (1.1)$$

Where i and j denote spatial indices and summation over indices appearing twice in the term is assumed. The first term is the part of the free energy not associated with electromagnetism and the next four terms describe spontaneous polarization and magnetization, as well as the usual polarizations by electric and magnetic fields. The last term gives the lowest order ME coupling, and higher order terms, such as $\beta_{ijk}E_iH_jH_k$, have been omitted. For given electric and magnetic fields, polarization and magnetization can be obtained by minimizing the free energy, giving

$$P_i(E,H) = -\frac{\partial F}{\partial E_i} = P_i^s + \varepsilon_0\varepsilon_{ij}E_j + \alpha_{ij}H_j + ... \tag{1.2}$$

$$M_i(E,H) = -\frac{\partial F}{\partial M_i} = P_i^s + \mu_0\mu_{ij}H_j + \alpha_{ij}E_j + ... \tag{1.3}$$

The linear ME coefficient, α thus describes both the electric polarization resulting from a magnetic field and the magnetization resulting from an electric field. This effect can occur only in the materials where time-reversal symmetry is broken, and was first observed in 1960 in antiferromagnetic Cr_2O_3 [19]. However, the effects found were generally much too weak for technological applications. ME coupling is limited by the relation $\alpha_{ij} < \sqrt{\varepsilon_0\varepsilon_{ij}\mu_0\mu_{ij}}$, and since FE and FM materials have particularly high ε and μ, large ME coupling might be expected for ferromagnetic ferroelectrics , one type of "multiferroics".

Ginzburg-Landau's approach can be followed to deduced a phenomenological idea to understand many properties of the coupling. Taylor-expansion of the free energy contain the two order parameters and adding two terms describing the linear couplings of M and P. Spatially uniform order parameters are considered first. Only even powers of $\vec{M}$ appear, because time reversal transforms $\vec{M} \to -\vec{M}$, but the free energy has to be invariant under time-reversal. $\vec{P}$ will also appear in even power. The same arguments

with time-reversal and space-inversion also hold for any mixed terms. To lowest order the total expansion for the spatially uniform system is thus

$$F(\vec{P},\vec{M}) = F_0 + \alpha\vec{P}^2 + \frac{\beta}{2}\vec{P}^4 + \alpha\vec{M}^2 + \frac{\beta}{2}\vec{M}^4 + \gamma\vec{P}^2\vec{M}^2 - \vec{P}\vec{E} - \vec{M}\vec{H} \tag{1.4}$$

Where sixth term is the lowest order coupling of P and M and the last two terms describe the effects of the conjugate fields on electric and magnetic order parameters. The coupling term leads for example to a change in the dielectric constant ($\varepsilon \propto \frac{\partial^2 F}{\partial F^2}$) around the magnetic transition, proportional to γM^2. However the coupling term does not contribute to the stabilization of ferroelectricity, because it is off-set by the energy cost for a polar lattice distortion $\propto -P^2$.

To understand the basic phenomena of multiferroics, and appreciate the main achievements and remaining problems in this field, it is necessary to classify multiferroics by the microscopic mechanism that determines their properties.

1.3 Microscopic Origin of Ferromagnetic Ferroelectrics

As ferromagnetism and ferroelectricity is coupled in multiferroic materials, limiting the discussion on perovskite (ABO_3) materials, it is proposed that the microscopic origin of magnetism in multiferroics is basically the same as in all magnets: it is the presence of localized electrons, mostly in the partially filled d or f shells of transition-metal or rare-earth ions, which have a corresponding localized spin, or magnetic moment. Exchange interactions between the localized moments lead to magnetic order. The situation with ferroelectrics is quite different. FE polarization in a material comes from the distorted asymmetric crystal structure but a symmetric structure is needed for ferromagnetism. Researchers realised that there are several different microscopic sources of ferroelectric-

ity, and accordingly one can have different types of multiferroics. It is reported that for perovskite compounds, conventional mechanism for ferroelectricity is off centring of B-site d^0 electrons. For ferroelectricity and magnetism to coexist in a single phase, therefore, the atoms that move off centre to form the electric dipole moment should be different from those that carry the magnetic moment. In principle, this could be achieved through either an alternative (non-d-electron) mechanism for magnetism, or through an alternative mechanism for ferroelectricity; in practice only the latter route has been pursued (such as for ferroelectricity the centred Ti ions in $BaTiO_3$ (BTO) plays the key role while in $PbTiO_3$ (PTO) the effect of Pb lone-pair is dominant [38, 39, 40]), and the exploration of multiferroics with different forms of magnetism is an open area for future research. In the magnetic perovskite-structure oxides and related materials, multiferroism is most commonly achieved by making use of the stereochemical activity of the lone pair on the large (A-site) cation to provide the ferroelectricity, while keeping the small (B-site) cation magnetic.

1.4 Types of Multiferroics

Multiferroic materials can be separated into two groups. The first group, called type-I multiferroics, contains those materials in which ferroelectricity and magnetism have different sources and appear largely independent of one another, though there is some coupling between them. In these materials, ferroelectricity typically appears at higher temperatures than magnetism and the spontaneous polarization P is often rather large (of order 10 -100 $\mu C/cm^2$). The second group, which we can call type-II multiferroics, is the relatively recently discovered materials [41, 42], in which magnetism causes ferroelectricity, implying a strong coupling between the two. However, the polarization in these materials is usually much smaller ($\sim 10^{-2}\mu C/cm^2$). Also multiferroics can be

divided into two groups: (a) single phase multiferroic compounds and (b) multiferroic composite systems.

1.4.1 Single Phase Multiferroic Compounds

Single Phase multiferroic Compounds can be divided into several groups depending on the origin of their multiferroic properties or chemical formula. Here we will mention some important ones.

1.4.1.1 Bismuth ferrite ($BiFeO_3$)

Since 1960, $BiFeO_3$ has attracted much attention as it is one of the very few multiferroics material with a simultaneous coexistence of FE and antiferromagnetic order parameters in single phase. It is also the most commonly studied multiferroic material, in part because of its large FE and magnetic ordering temperatures, T_c = 1123 K and T_N = 643 K. Intensive studies are conducted on $BiFeO_3$ to understand the physical properties and the structure of this material to make it useful for device applications.

Crystal Structure

$BiFeO_3$ crystallizes in the perovskite rhombohedral structure with space group R3c [45]. The lattice parameter of $BiFeO_3$ unit cell is $a_{rhombohedral}$ = 3.965 Å and the rhombohedral angle α is 89.3°-89.4° at room temperature [46, 47]. The unit cell can also be described by hexagonal structure with the c axis parallel to the diagonals of the perovskite cube, namely $[001]_{hexagonal} \parallel [111]_{pseudocubic}$. In this case the reported lattice parameters are $a_{hexagonal}$ = 5.58 Å and $c_{hexagonal}$ = 13.89 Å [46, 48]. In case of a ideal cubic structure the rotation angle of the oxygen octahedra should be 0°, but for $BiFeO_3$ this angle is ω= 11°-14° around the polar $[111]_{pseudocubic}$ axis [45, 47]. This change in rotation angle

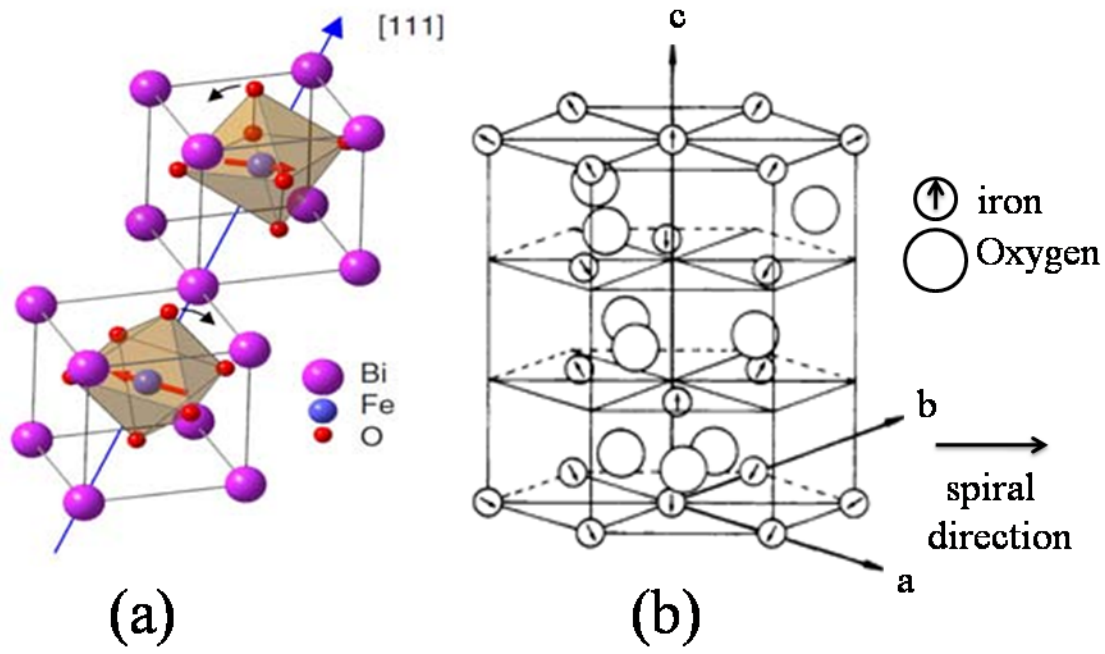

Figure 1.2: (a) Crystal structure of bulk $BiFeO_3$ [43] and (b) The part of the $BiFeO_3$ lattice with only iron and oxygen ions shown. The arrows indicate the Fe^{3+} moment direction [44].

distorts the oxygen octahedra which changes the Fe-O-Fe bond angle (θ =154° to 156° [47, 49]) which controls both the magnetic exchange and orbital overlap between Fe and O in $BiFeO_3$. Oxygen octahedra is tilted in $BiFeO_3$ can be concluded from the value of Goldschmid tolerance factor (t) defined as [50], $t = (r_{Bi} + r_O)/(r_{Fe} + r_O)^{1/2}$. For $BiFeO_3$, t=0.88 [51], with Bi ion in eightfold coordination and Fe ion in sixfold coordination and high spin, i.e. t value is less than one so the oxygen octahedra distorts in order to fit into a small unit cell.

Ferroelectricity

In general, all conventional FE perovskites contain transition metal (TM) ions with a empty d-shell i.e.d^0 configuration (of course not all such systems are FE, such as $SrTiO_3$). But $BiFeO_3$ does not contain any d^0 TM, the only magnetic TM it has is

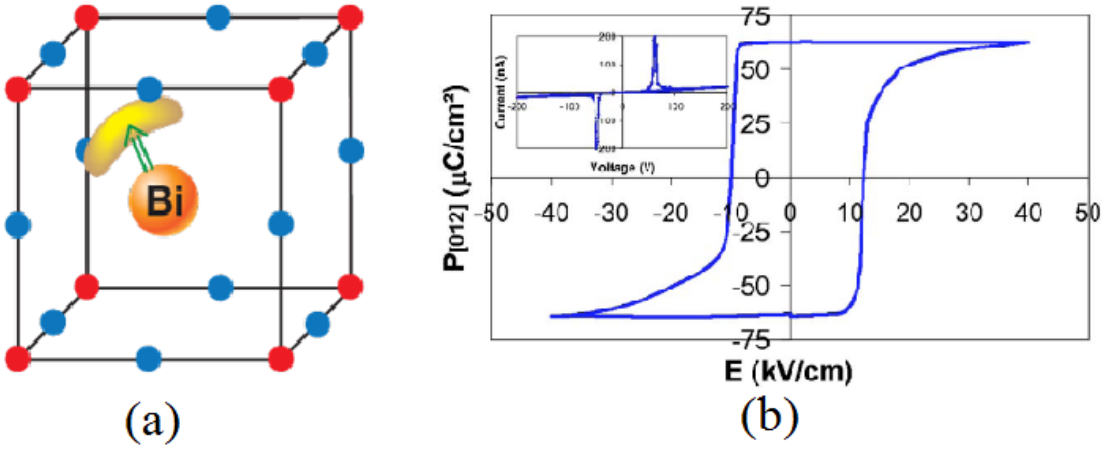

Figure 1.3: (a) In $BiFeO_3$ the ordering of lone pairs (yellow "lobes") of Bi^{3+} ions (orange), contributes to the polarization (green arrow) [52] and (b) First full P-E hysteresis loop of a single crystal of $BiFeO_3$ at room temperature. The remnant polarization $P_{[012]}$ is 60 $\mu C/cm^2$ and the coercive field is 12 kV/cm, Inset shows I-V data [53].

Fe^{3+} with a d^5 configuration. A more detailed analysis on $BiFeO_3$ shows that the FE in this system is not due to TM ions as, e.g. in $BaTiO_3$, but is rather occur by the A-ions, in this case Bi. Bi^{3+} contains active lone pair or two valence electrons, capable of participating in chemical bonds using sp^2 hybridized states but do not participate in such bonds. These lone pair s^2 electrons of Bi ions break local inversion symmetry. So the small B site cation, Fe in $BiFeO_3$ lowers its energy by shifting along one of the [111] directions (Fig 1.3(a)). So in bulk $BiFeO_3$ the FE polarization direction is along $[001]_{hexagonal}/[111]_{pseudocubic}$ of the perovskite structure. Early measurements of bulk ferroelectricity in the 1960s and 1970s yielded only small values of the polarization. Teague *et al.* reported the value of spontaneous polarization (P) is 3.5 $\mu C/cm^2$ along [100] direction and 6.1 $\mu C/cm^2$ in the [111] direction at 77 K [54]. However, the value of P was smaller than expected for a material with such a high Curie temperature. Teague *et al.* claimed that this small value of P was due to the leakage current in $BiFeO_3$ and the actual polarization value of $BiFeO_3$ should be an order of magnitude higher. Their

prediction proved right after more than 30 years by measurements on high-quality thin films [55], single crystals, [53] and ceramics [56]. All these findings enormously stimulated the research in this field. This large polarization of the $BiFeO_3$ thin films reported by Ramesh's group [55] was initially thought to be due to strain enhancement, but later this prediction was omitted by the facts that good single crystals shows remanant polarization value 60 $\mu C/cm^2$ along the direction normal to (001) and, therefore, approximately 100 $\mu C/cm^2$ along $[111]_{pseudocubic}$ [53, 57, 58]. Ab initio calculations also agreed with the obtained results [59]. Theses studies revealed that the defects are the main reason behind the low P value in $BiFeO_3$ [60, 61]. Further studies verified that oxygen deficiency in $BiFeO_3$ which leads to the leakage current problem can be reduced by short sintering time and rapid heating rate of the compound [62]. Other methods have been also employed to reduce the leakage current problem in $BiFeO_3$, including doping on A-sites and B-sites, growing high quality single crystals and in nanostructures [63, 64, 65, 66, 67].

Magnetism

Magnetism in $BiFeO_3$ can be ascribed to both long-range and short-range magnetic orderings. Sosnowska [44] reported that the short-range magnetic ordering in $BiFeO_3$ is G-type antiferromagnetic, i.e. each Fe^{3+} spin is surrounded by six antiparallel spins of the nearest neighbors Fe^{3+} ions. This means that the Fe^{3+} magnetic moments are coupled ferromagnetically within the pseudocubic (111) planes and antiferromagnetically between adjacent planes. Fig 1.2(b) shows the hexagonal representation of the spin structure of $BiFeO_3$. Due to the structural distortion, the arrangement of the neighbouring spins is in fact not perfectly antiparallel. The canted spins induce a weak magnetic moment that couples with the FE polarization. However, it is also found that the long range magnetic ordering in $BiFeO_3$ consists of an incommensurate spin cycloid of the antiferromagnetically ordered sublattices. The cycloid has a very long repeat distance of

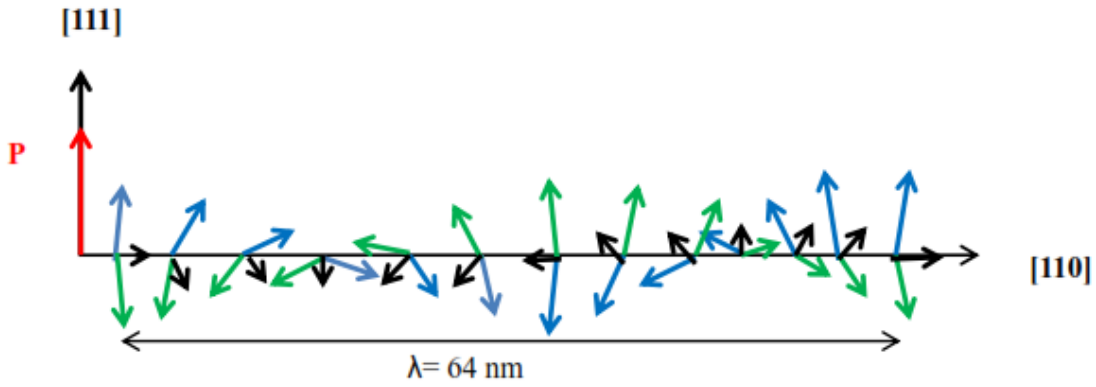

Figure 1.4: Schematic representation of the spin cycloid. The canted antiferromagnetic spins (blue and green arrows) give rise to a net magnetic moment (black arrows) that is specially averaged out to zero due to the cycloidal rotation. The spins are contained within the plane defined by the polarization vector (red) and the cycloidal propagation vector (black) [67].

62-64 nm as shown in Fig 1.4 and a propagation vector is along the [110] direction [67]. This leads to the cancellation of the magnetization. The linear magneto-electric effect is allowed by the average R3c space group but at the same time is excluded by the spin cycloid. This spin cycloidal ordering in $BiFeO_3$ structure was first proposed by Sosnowska *et al.* in 1982 [44]. However it was verified by a number of experiments afterwards, including XRD, neutron scattering, Mössbauer measurements, etc. [44, 68, 69, 70]. In recent years Zalesskii and co-workers proposed that the simple cycloid is distorted at low temperatures [71, 72]. But, they did not indicated any information about the phase transition temperature where the spin reorientation transition should occur. Recently, Cazayous *et al.* first reported a transition at 140 K [73] and, independently, Singh *et al.* found that one and an apparently stronger one at 200 K [74]. The possible origin for these transitions is considered to be spin reorientation.

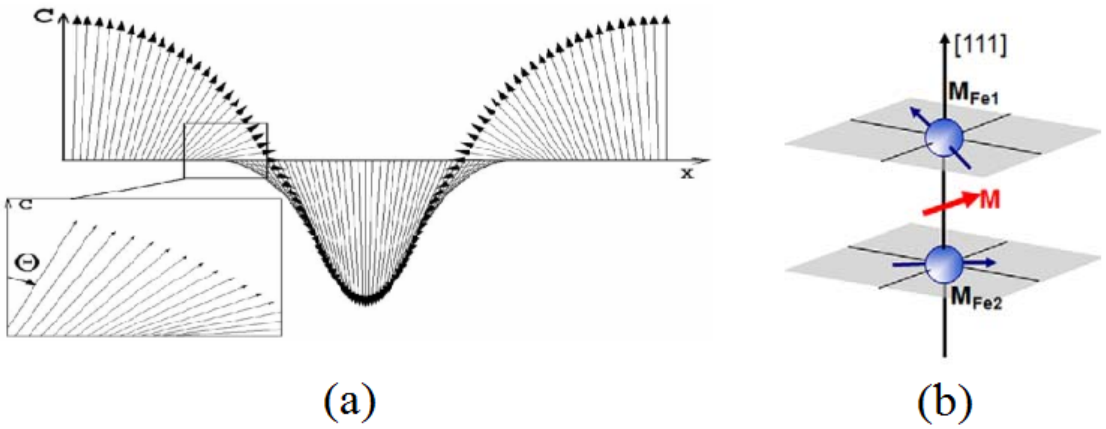

Figure 1.5: (a) Schematic antiferromagnetic structure of $BiFeO_3$ [75] and (b) $BiFeO_3$ might possess a weak ferromagnetic moment [77].

Magnetoelectric coupling

The reason behind ME coupling in $BiFeO_3$ is subtle. The sprial modulated spin structure allows the second order ME coupling in $BiFeO_3$. According to Dzyaloshinski-Moriya theory domain wall of $BiFeO_3$ might show very small net magnetic moment of 0.3 emu/g [76] if the moments are oriented in a direction perpendicular to [111] (Fig 1.5(b)) [77]. However this explanation has not been proved yet [65]. Furthermore, the coupling between magnetic and FE order parameter in $BiFeO_3$ is confirmed experimentally by using the X-ray photoelectron microscope and piezoelectric-force microscope together [78].

1.4.1.2 $REMnO_3$ (RE: Y, La, Pr, Nd etc.)

This class of single phase multiferroic includes rare earth (*RE*: Y, La, Pr, Nd etc.) perovskite manganites having hexagonal crystal structure. Studies on the magnetic properties and spin arrangements have done long time ago [79, 80, 81, 82, 83]. In this class of heavy rare-earth compound Jahn-Teller distortion is quite dominant with

a set temperature above 1000 K. This distortion is unchanged for Ho, Er and Y but increases from La to Tb [84]. So as the Mn ion ordering temperature (T_N), it is $\sim$ 40 K for Ho, Er and Y but increases with the ionic radius (T_N is 40 K for Tb and 141 K for La). Magnetic ordering in the R^{3+} cations occurs at lower temperatures [85, 86]. Neutron diffraction experiments show that $LaMnO_3$ and $PrMnO_3$ have a C-type antiferromagnetic structure with a FM $a-c$ layer antiferromagnetically coupled along the b direction [81, 87, 88]. $NdMnO_3$ also have a similar magnetic structure with a FM component along b direction associated with Mn ions [89]. $TbMnO_3$ and $HoMnO_3$ have a sinusoidal wave magnetic structure with a propagation vector $K = (K_x, 0, 0)$, only in case of $HoMnO_3$ magnetic ordering occurs below 40 K [79, 80, 90]. For La, Pr and Nd manganites the Mn magnetic moments are oriented along the a-axis direction [81, 87, 88, 89]. In $YMnO_3$ the Mn magnetic moments have helical orientation with the moments rotating in the $b-c$ plane.

It is a proven fact that compounds which have Jahn-Teller active orbital degrees of freedom cannot have off-center FE distortions [91]. So ferroelectricity in these compounds cannot arise from the off-centring of the lattice ion due to the structural distortion. Ferroelectricity here can be explained by the non-centrosymmetric space group with the P_r direction parallel to the c axis [92]. In $YMnO_3$ the corners of the MnO_5 polyhedra is linked to form a triangular layer. In each of this Mn layer trimerization of Mn^{3+} occurs by the distortion in this polyhedra. The unequal distribution of the upward (2/3 of the Y ions) and downward (1/3 of the Y ions) Y ions give rise to a net polarization in this compound. Firbig *et al.* [93] found that the coupling between antiferromagnetism and ferroelectricity in this compound originates from the interaction between the magnetic and FE domain walls. Similar type of interaction observed in $HoMnO_3$ as well [94]. Detailed study on $TbMnO_3$ showed that modulation in the magnetic structure induces magnetoelastic effect in this compound which leads to the

lattice distortion, reason behind the polarization in this compound. Here the magnetic field induced electric polarization leads to the ME effect [95].

1.4.1.3 Double Perovskite Compounds ($A_2BB'O_6$)

In ordered double perovskites two different B-site cations form a superlattice within the ABO_3 perovskite structure. This class of perovskites have attracted great interest recently as they may possess both FM and FE or FM and ferroelastic properties, and are therefore multiferroics [37, 96, 97]. Ferromagnetism in these compounds mainly governed by the 180° superexchange process. Whereas, ferroelctricity occurs form the structural distortion due to the different chemical valencies of the B and B′ site or due to the A site atom.

La_2CoMnO_6 (LCMO) [98], Bi_2CoMnO_6 (BCMO), Bi_2FeMnO_6 (BFMO) [99], Bi_2FeCrO_6 (BFCO) [100] and Bi_2NiMnO_6 (BNMO) [101] are some of the important members of this double perovskite group. Single-phase epitaxial LCMO films [102] on insulating $SrTiO_3$ (STO) shows a decreases in dielectric constant value as one cools them down in the FM regime. LCMO film shows 3% magnetodielectric effect in the FM phase regime and ferro-para phase transition properties above 250 K. Detail study shows that epitaxial BCMO films grown on STO and $LaAlO_3$ have large FM Curie temperature of about 800 K [103]. This large Curie temperature of this film is reported as the result of a strong coupling between the magnetization and the polarization order parameters. BFMO film synthesized on Si substrates by an electrospray method shows three peaks at 150 K, 260 K, and 440 K in the MT curve due to the inhomogeneous distribution of Fe^{3+} and Mn^{3+} ions [104]. These observed magnetic peaks are reported corresponds to orderings of the ferrimagnetic Fe-O-Mn, and antiferromagnetic Mn-O-Mn and Fe-O-Fe layers, respectively. $Nd_{0.1}Bi_{0.9}FeO_3$/BFMO bilayered films on Pt/Ti/SiO_2/Si substrate deposited by pulsed laser deposition method shows FM properties with the transition at 440 K [105].

The film is suggested to have a promising RT multiferroism due to the observed room temperature ferroelectric polarization along with FM properties. Similarly, BFCO thin film deposition on $LaAlO_3$ substrate by pulsed laser shows phase transition from FE to paraelectric phase above 900 K and a possible magnetic phase transition between 600 and 800 K [100]. Raman study of BNMO thin film grown on (001) STO by pulsed laser deposition [101] also shows multiferroic properties with a FE polarization of 5 $\mu C/cm^2$ and magnetic transition at 100 K. Synchrotron X−ray diffraction confirms that the Ni an Mn ions in this compounds are ideally ordered. So the high transition temperature for magnetic and electric orderings in these materials from the structural characteristics make them interesting.

1.4.1.4 $REMn_2O_5$ (RE = Gd, Tb, Dy, Ho etc.)

Recently, rare-earth manganese oxides belonging to $REMn_2O_5$ group are found to posses multiferroic properties [106, 107]. This family of oxides are known from the 1960s. All the compounds in this group (RE = Gd, Tb, Dy, Ho etc.) have orthorhombic crystal structure with slight difference in the lattice parameters. In these kind to structures Mn has 3+ and 4+ valance states. Mn^{3+} ion occupies the $4h$ sites and they are bonded by five oxygens, forming a distorted tetragonal pyramid, while the Mn^{4+} ions form octahedra with oxygen. Neutron diffraction data indicated an antiferromagnetic magnetic ordering [108, 109] in these compounds. Further detail study on magnetic ordering revealed a very complex arrangement in which the Mn atoms takes two different in the crystallographic position in the structure [110, 111, 112, 113]. The magnetic structure of most of the oxides of this family is defined by the propagation vector $\mathbf{k}$=(1/2,0,k_z), where K_z depends on the rare earth RE and also on the temperature. Whereas, in $LaMn_2O_5$ this structure is expressed as $\mathbf{k}$=(0,0,1/2) [114].

Recently, an external magnetic field induced and/or modified FE states is observed

in the $DyMn_2O_5$ magnetic material [115]. It shows three FE phases in the temperature ranging between 43 and 4 K. The zero-field lowest temperature phase (<8 K) induced by the Dy moment ordering is a reentrant paraelectric state, but with the increase in magnetic field it turned into a FE state. The phenomenon is closely related to the metamagnetic transitions of the Dy f moment, indicating that all the FE phases of this material are strongly tied to the antiferromagnetic Mn spin structure affected by the $f-d$ exchange interaction. The polarized Raman spectra of isostructural $HoMn_2O_5$ and $TbMn_2O_5$ measured between 7 and 300 K [116] shows that the A_g spectra provides no evidence for anomalies associated with magnetic and/or FE ordering in these samples. In $TbMn_2O_5$, it is observed that magnetic ordering temperature (10 K) play a significant role in the FE properties [117]. Magnetic resonance spectra of $GdMn_2O_5$ showed that the magnetic state of the material has a strong effect of on the FE properties [118].

1.4.1.5 Fluoride Multiferroics

Apart from oxides some of the fluorides and oxyfluorides also show FE properties and are potential multiferroic systems. $BaMnF_4$ shows spin canting induced ferroelectricity [119]. $K_3Fe_5F_{15}$ shows both ferroelastic and FE properties below T_c= 490 K [120]. Recent Mössbauer studies on this material shows spontaneous magnetic ordering at temperature below 30 K and dielectric anomaly, which is the characteristic of ME behaviour, at 122 K [121]. Also there are other magnetic fluorides which show FE switching such as $Sr_3(FeF_6)_2$, $Pb_2Cr_3F_{19}$ and $(NH_4)_3FeF_6$ [122, 123, 124].

1.4.2 Multiferroic Composite Systems

Natural multiferroic single-phase compounds are rare, and their magnetoelectric (ME) responses are either relatively weak or occurs at temperatures too low for practical

applications. In contrast, multiferroic composites, which incorporate both FE and ferri/ferromagnetic phases, typically yield giant ME coupling response above room temperature, which makes them ready for technological applications. Suchtelen [125] proposed the concept of a product property in two-phase composite materials in 1972, arising from an elastic coupling between two phases of different properties. After this, scientists in Philips Laboratory experimentally found a large ME effect ($\partial E/\partial H$ =0.13 V/ cm Oe at room temperature) in BTO$-CoFe_2O_4$ composites [126, 127]. They prepared this composite by unidirectional solidification of eutectic compositions in the quinary Fe-Co-Ti-Ba-O system. The ME effect obtained in this way can reach about hundred times larger than that in single-phase multiferroic one. But unidirectional solidification is complex and requires critical control over composition and processing. Research went inactive for almost 20 years across the world. Then in the early 1990s, Newnham's group [128] and Russia scientists [129, 130] prepared particulate ceramic composites of ferrites and BTO or $Pb(ZrTi)O_3$ (PZT)which were much more easier and cost effective to fabricate in comparison to eutectic composites. Various interesting ME composites investigated in recent years, can be divided in four groups.

1.4.2.1 Bulk Ceramic Composites

In the past decades, various ceramic composites consisting of piezoelectric and magnetic oxide ceramics are investigated. Two-phase composite is noted as 0-3, 2-2, 1-3 etc. which can be understood using the concept of phase connectivity introduced by Newnham et al. [131], for example, a 0-3 type particulate composite means one-phase particles (denoted by 0) embedded in the matrix of another phase (denoted by 3). Connectivity schemes used commonly are (a) 0-3 type particulate composites of piezoelectric and magnetic oxide grains, (b) 2-2 type laminate composites of BTO based FE ceramics and ferrites (or doped ferrites), PZT and ferrites (or doped ferrites), $(SrBa)Nb_2O_5$ and ferrites, and

so on [129, 130, 132] and (c) 1-3 type fibre composites with fibre/rod of one phase embedded in the matrix of another phase, as shown in Fig 1.6.

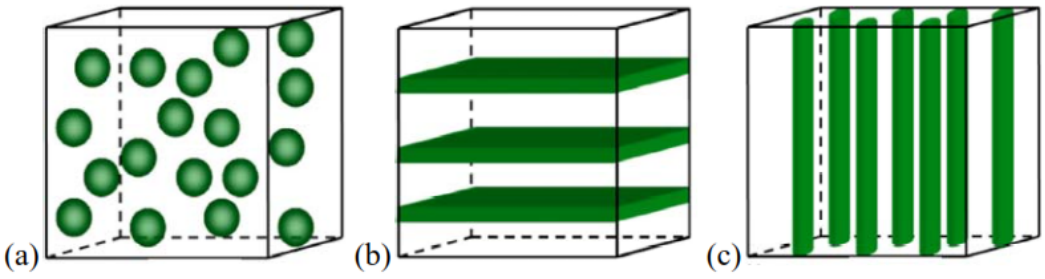

Figure 1.6: Schematic illustration of three bulk composites with the three common connectivity schemes: (a) 0−3 particulate composite, (b) 2−2 laminate composite and (c) 1−3 fibre/rod composite.

1.4.2.2 Two phase ME Composites of Magnetic Alloys and Piezoelectric Materials

Rare-earth-iron alloys such as $SmFe_2$, $TbFe_2$ or $Tb_{1-x}Dy_xFe_2$ (Terfenol-D) are very well known for exhibiting much higher magnetostriction compared to the magnetic oxide (such as ferrite) ceramics. Thus the composites of these alloys and piezoelectric materials should have much large ME response. Nan *et al.* first calculated the ME response of such composites by generalizing Green's function technique [133]. Experimentally, this giant ME effect was reported first by Ryu *et al.* [134] in the Terfenol-D/PZT laminate and in the Terfenol-D/polyvinylidene fluoride (PVDF) laminate by Mori and Wuttig [135]. Since then, Dong et al. [136, 137] have reported the ME effect in a number of laminate composites of Terfenol-D and various piezoelectric materials including PZT ceramics, $Pb(Mg_{1/3}Nb_{2/3}O_3)$-$PbTiO_3$ (PMN-PTO) or $Pb(Zn_{1/3}Nb_{2/3}O_3)$-$PbTiO_3$ (PZN-PTO) single crystal, or electroactive PVDF copolymers [138].

1.4.2.3 Three phase ME composites

In the two-phase Terfenol-D based laminates, the eddy current loss in bulk Terfenol-D is quite large at high frequency and Terfenol-D thin layers are very brittle which limits the applications of this laminate structure [139] as a ME composites. In order to overcome these difficulties a three-phase composite of Terfenol-D, PZT, and a polymer is developed. The simplest three-phase ME composite is quasi-0-3 type particulate composites where Terfenol-D grains are randomly oriented in the mixture matrix of PZT and polymer [140]. Other composites are 2-2 type laminate composites containing Terfenol-D/polymer and PZT/polymer [141], 1-3 composite (a fibre/rod reinforced composite) [142]. According to the design of a 1-3 three phase composite, a PZT bulk is diced to get a PZT rod array, and then the gap of the PZT rod array is filled with the mixture of Terfenol-D particles and epoxy. When the epoxy hardens, the pseudo 1-3 type multiferroic composite is obtained.

1.4.2.4 Nanostructured Composite Thinfilms

Recently, motivated by a pioneer work of Zheng *et al.* [143], multiferroic nanocomposite thin films of FE (such as BTO, PTO, PZT, and $BiFeO_3$) and magnetic oxides (such as CFO, NFO, and LCMO) prepared via thin film deposition techniques (such as pulsed laser deposition and sol-gel spin-coating method) have become new routes to multiferroic composites [144]. In comparison to bulk multiferroic ME composites, the nanostructured thin films provide more degrees of freedom, such as lattice strain or interlayer interaction, to modify the ME behavior. It also offers a way to investigate the physical mechanism of ME effect in nanoscale. However, the mechanical constraint arising from the thin film grown on substrate and the good bonding between the two phases in the nanostructurd composite films significantly affect the ME coupling interactions.

Similarly to the bulk composites nanostructured composite films can also be divided into three groups, (a) 0-3 type structures with magnetic spinel nanoparticles (such as Co-ferrite and Ni-ferrite) embedded in the FE films (such as PZT) [145], (b) 1-3 type heterostructures (vertical heterostructures) consisting of magnetic spinel pillars (such as Co-ferrite) vertically embedded into a FE films (such as BTO, PTO, or $BiFeO_3$) [143] and (c) 2-2 type heterostructures (horizontal nanostructures) consisting of alternating layers of a FE perovskite and magnetic oxide [146].

1.5 Motivation of the Thesis

The effort to use magnetoelectrics in technology, is become very difficult as more highly insulating single-phase magnetoelectrics, with operating temperatures above ambient and with larger magnetization is needed. For a magnetoelectric RAM, one would like to combine the ultrafast (250 ps) electrical WRITE operation with the non-destructive (no reset) magnetic READ operation, thus combining the best qualities of FRAM and MRAM. But thus far, the magnetization of multiferroics is too small for effective READ.

Among all the natural single phase multiferroics, only $BiFeO_3$ shows ME coupling at RT, but the coupling is too weak to use for a practical purpose. Motivation of our work is to enhance the multiferroic properties of $BiFeO_3$. Magnetic moments in $BiFeO_3$ have a complex spin cycloid structure of wavelength ~ 62 nm. Because of this structure the macroscopic magnetization is cancelled. In addition Bi is stereochemically active because of the lone pair of electrons. Hence, $BiFeO_3$ has very low resistance and high leakage characteristics. It is therefore of interest to modify the space-modulated spin cycloid structure and stabilize Bismuth. Doping of various elements like rare earth, transition, alkaline-earth in the A and B site can overcome this problem since due to doping some distortion might take place which will break the spin cycloid. Doping of

rare earth elements in the Bi site can improve the stoichiometry of the structure and reduce the leakage current since rare earth elements are extremely stable elements. This motivated us to dope Ba in the Bi site and Gd in the Fe site of the $BiFeO_3$ ceramics separately and study their properties in details. Synthesis of nanostructures can be a solution to this problem since thinfilms or nanowires will not have the problem of spin cycloid. So we have prepared $BiFeO_3$ nanostructure (thinfilm and nanowires) and studied the multiferroic properties.

1.6 Thesis Organization

The thesis begins with a brief introduction (**present chapter**) describing the significance of the present work, introduction to the multiferroic materials, origin of multiferroic (magnetic, FE and ME) properties in the material, type of multiferroics, necessary literatures on earlier work done. In my PhD, we have worked on $BiFeO_3$ (BFO) so a detailed literature study on $BiFeO_3$ is also added in this chapter.

Chapter 2 is focused on the various techniques we have used for sample preparation, characterization and measurements.

Chapter 3 presents the study on single doped (Ba on A-site) and co-doped (Ba on A site and Gd on B site) $BiFeO_3$ ceramics. It discusses the detailed description of magnetic, ferroelectic, conductivity and ME behaviour of the bulk $BiFeO_3$ samples.

Chapter 4 presents the multiferroic properties of $BiFeO_3$ thin films deposited on Si substrate by pulse laser deposition technique. Thickness of the film is also varied to observe the thickness dependent magnetic and FE properties.

Chapter 5 presents the detail study on undoped and doped (Pr on A site and Cr on B site) $BiFeO_3$ nanowires(NWs)/nanotubes(NTs) fabricated within the nanopores

of AAO template by wet-chemical route. The effects of diameter on FM and dielectric behaviour are also presented. In addition, photovoltaic properties of the $BiFeO_3$ NWs are also discussed.

Chapter 6 describes the conclusions and the scope for future works.

References

[1] M. Dawber, K. M. Rabe, and J. F. Scott, Rev. Mod. Phys. 77, 1083 (2005).

[2] S. H. Wemple, Phys. Rev. B 2,2679 (1970).

[3] G. Gerra, A. K. Tagantsev, N, Setter, and K. parlinski, Phys. Rev. lett. 96,107603 (2006).

[4] P. G. Radaelli, G. Iannone, M. Marezio, H. Y. Hwang, S-W. Cheong , J. D. Jorgensen and D. N. Argyriou, Phys. Rev. B 56, 82658276 (1997).

[5] Y. Tomioka, A. Asamitsu, Y. Moritomo, H. Kuwahara and Y. Tokura, Phys. Rev. Lett. 74, 5108 (1995).

[6] B. Keimer, N. Belk, R. J. Birgeneau, A. Cassanho, C. Y. Chen, M. Greven, M. A. Kastner, A. Aharony, Y. Endoh, R. W. Erwin and G. Shirane, Phys. Rev. B 46, 1403414053 (1992).

[7] B. Dieny, V. S. Speriosu, S. S. P. Parkin, B. A. Gurney, D. R. Wilhoit, and D. Mauri, Phys. Rev. B 43, 12971300 (1991).

[8] R. E. Camley and J. Barnas, Phys. Rev. Lett. 63, 664 (1989).

[9] F.C. Zhang and T. M. Rice, Phys. Rev. B 37, 3759 (1988).

[10] Y. Tokura, H. Takagi and S. Uchida, Nature 337, 345 (1989).

[11] P. Filippov, P. Yu, G. G. Ihas and V. V. Vainberg, Rev. Sci. Instrum. 80, 094902 (2009).

[12] M. Vazquez and A. Hernando, J. Phys. D 29, 939 (1996).

[13] X. Li, K. terabe, H. Hatano, H. Zeng and K. Kitamura, J. Appl. Phys. 100, 106103 (2006).

[14] Y. H. Xie, Y.Y. Lin and T. A. Tang, Integrated Ferroelectrics, 67, 255 (2004).

[15] G. Reiss and A. Hutten, Nat. Mater. 4, 725 (2005).

[16] J. P. Wang, Nat. Mater. 4, 191 (2005).

[17] L. D. Landau and E. M. Lifshitz, Electrodynamics of continuous media (Fizmatgiz, Moscow, 1959).

[18] I. E. Dzyaloshinskii, Sov. Phys. JETP 10, 628 (1959).

[19] D. N. Astrov, Sov. Phys. JETP 11, 708 (1609).

[20] G.A. Smolenskii, et al., Segnetoelectrics and Antisegnetoelectrics, Nauka Publishers, Leningrad, 1971 (in Russian).

[21] G.A. Smolenskii, I.E. Chupis, Sov. Phys. Uspekhi 25, 475 (1982).

[22] Y.N. Venevtsev, V.V. Gagulin, Ferroelectrics 162, 23 (1994).

[23] H. Schmid, Ferroelectrics 162, 317 (1994).

[24] J.P. Rivera, Ferroelectrics 161, 165 (1994).

[25] B.I. AlShin and D.N. Astrov, So. Phys. JETP 17, 809 (1963).

[26] G.T. Rado, Phys. Rev. Lett. 13, 335 (1964).

[27] T. Watanabe and K. Kohn, Phase Trans. 15, 57 (1989)

[28] G. A. Smolenskii and I. E. Chupis, Usp. Fiz. Nauk 137, 415 (1982)

[29] G. Lui, C. Naan, N. Cai and Y. Lin, J. Appl. Phys. 95, 2660 (2004).

[30] C. R. Serrao, A. Sundaresan and C. N. R. Rao, J. Phys. Cond. Mat. 19, 496217 (2007).

[31] A. B. Harris, M. Kenzelmann, Amnon Aharony and O. Entin-Wohlman, Phys. Rev. B 78, 014407 (2008)

[32] D. Talbayev, A. D. LaForge, S. A. Trugman1, N. Hur, A. J. Taylor, R. D. Averitt and D. N. Basov, Phys. Rev. Lett. 101, 247601 (2008).

[33] Z. X. Cheng, X. L. Wang, S. X. Dou, H. Kimura, and K. Ozawa, J. Appl. Phys. 107, 09D905 (2010).

[34] R. D. Johnson, S. R. Bland, C. Mazzoli, T. A. W. Beale, C-H. Du, C. Detlefs, S. B. Wilkins, and P. D. Hatton, Phys. Rev. B 78, 104407 (2008).

[35] T. Kimura, S. Kawamoto, I. Yamada, M. Azuma, M. Takano and Y. Tokura, Phys. Rev. B 67, 180401(R) (2003)

[36] J. B. Neaton1, C. Ederer, U. V. Waghmare, N. A. Spaldin, and K. M. Rabe, Phys. Rev. B 71, 014113 (2005).

[37] N. A. Hill, J. Phys. Chem. B 104, 66946709 (2000).

[38] W. J. Merz, Phys. Rev. 95, 690 (1954).

[39] R. D. King-Smith and D. Vanderbilt, Phys. Rev. B 49, 5828 (1994).

[40] G. Burns and B. A. Scoot, Phys. Rev. B 7,3088 (1973).

[41] T. Kimura et al., Nature 426, 55 (2003).

[42] N. Hur et al., Nature 429, 392 (2004).

[43] Axel Lubk, S. Gemming, and N. A. Spaldin, Phys. Rev. B Vol. 80, 104110 (2009).

[44] I. Sosnowska et al., J. Phys. C. 15, 4835 (1982).

[45] J. M. Moreau, C. Michel, R. Gerson, W. J. James, J. Phys. Chem. Solids, 32, 1315 (1971).

[46] V.S Filip'ev, I.P Smol'yaninov, E.G Fesenko, I.I Belyaev, Crystallogr. 5, 913 (1960).

[47] F. Kubel, H. Schmid, Acta Cryst. B 46, 698 (1990).

[48] J. D. Bucci, B. K. Robertson, W. J. James, J. Appl. Cryst. 5, 187 (1972).

[49] A. Palewicz, R. Przenioslo, I. Sosnowska, A. W. Hewat, Acta Cryst. B 63, 537 (2007).

[50] V. M. Goldschmidt, Naturwissenschaften 14, 477 (1926).

[51] R. D. Shannon, Acta Cryst. A 32, 751 (1976).

[52] D. Khomskii, Physics 2, 20 (2009).

[53] D. Lebeugle D. Colson, A. Forget, M. Viret, P. Bonville, J. F. Marucco, S. Fusil, Appl. Phys. Lett. 91, 022907 (2007).

[54] Teague, Gerson and James, Solid State Commun. 8, 1073 (1963).

[55] J. Wang, J. B. Neaton, H. Zheng, V. Nagarajan, S. B. Ogale, B. Liu, D. Viehland, V. Vaithyanathan, D. G. Schlom, U. V. Waghmare, N. A. Spaldin, K. M. Rabe, M. Wuttig, R. Ramesh, Science, 299, 1719 (2003).

[56] V. V. Shvartsman, W. Kleemann, R. Haumont, J. Kreisel, Appl. Phys. Lett. 90, 172115 (2007).

[57] R. P. S. M. Lobo, R. L. Moreira, D. Lebeugle, D. Colson, Phys. Rev. B, 76, 172105 (2007).

[58] M. Cazayous, D. Malka, D. Lebeugle, D. Colson, Appl. Phys. Lett. 91, 071910 (2007).

[59] C. Ederer, N. A. Spaldin, Phys. Rev. Lett. 95, 257601 (2005).

[60] X. Qi, J. Dho, R. Tomov, M. G. Blamire, and J. L. MacManus-Driscoll, Appl. Phys. Lett. 86, 062903 (2005).

[61] S. K. Singh, H. Ishiwara and K. Maruyama, J. Appl. Phys. 100, 064102 (2006).

[62] Y. P. Wang, L. Zhou, M. F. Zhang, X. Y. Chen, J.-M. Liu, and Z. G. Liu, Appl. Phys. Lett. 84, 1731 (2004)

[63] S.R. Das, R.N.P. Choudhary, P. Bhattacharya, R.S. Katiyar, J. Appl. Phys. 101, 034104 (2007).

[64] V. R. Singh, A. Garg1, and D. C. Agrawal, Appl. Phys. Lett. 92, 152905 (2008).

[65] V. Raghavendra Reddy, Deepti Kothari, Ajay Gupta, and S. M. Gupta, Appl. Phys. Lett. 94, 082505 (2009).

[66] J. W. Lin, Y. H. Tang, C. S. Lue, and J. G. Lin App Phys. Lett. 96, 232507 (2010).

[67] D. Lebeugle, D. Colson, A. Forget, M. Viret, A. M. Bataille, A. Gukasov, Phys. Rev. Lett. 100, 227602 (2008).

[68] J. F. Scott, M. K. Singh, R. S. Katiyar, J. Phys.: Condens. Matter 20, 322203 (2008).

[69] A. Palewicz, T. Szumiata, R. Przenioslo, I. Sosnowska, I. Margiolaki, Solid State Commun. 140, 359 (2006).

[70] R. Przenioslo, A. Palewicz, M. Regulski, I. Sosnowska, R. M. Ibberson, K. S. Knight, J. Phys.: Condens. Matter 18, 2069 (2006).

[71] A. V. Zalesskii, A. K. Zvezdin, A. A. Frolov, A. A. Bush, JETP Lett. 71, 465 (2000).

[72] A. A. Bush, A. A. Gippius, A. V. Zalesskii, E. N. Morozova, JETP Lett. 78, 389 (2003).

[73] M. Cazayous, Y. Gallais, A. Sacuto, R. de Sousa, D. Lebeugle, D. Colson, Phys. Rev. Lett. 101, 037601 (2008).

[74] M. K. Singh, W. Prelier, M. P. Singh, R. S. Katiyar, J. F. Scott, Phys. Rev. B 77, 144403 (2008).

[75] A. M. Kadomtseva et al., Phase Transitions 79, 1019-1042 (2006).

[76] A.K. Zvezdina, A.M. Kadomtsevab, S.S. Krotovb, A.P. Pyatakovb, Yu.F. Popovb, G.P. Vorob'evb, J. Magn. Magn. Mater. 300, 224 (2006).

[77] T. Moriya, Phys. Rev. 120, 91 (1960).

[78] Kouhei Takahashi, Noriaki Kida and Masayoshi Tonouchi, Phys. Rev. Lett. 96, 117402 (2006).

[79] G. H. Jonker and J. H. Van Santen, Physica 16, 337 (1950).

[80] G. H. Jonker and J. H. Van Santen, Physica 19, 120 (1953).

[81] E. O. Wollan and W. C. Koehler, Phys. Rev. 100, 545 (1955).

[82] R. Pauthenet and C. Veyret, J. Physique 31, 65 (1970).

[83] V. E. Wood, A. E. Austin, E. W. Collings and K.C. Brog, J. Phys. Chem. Solids 34, 859 (1973).

[84] J. A. Alonso, M. J. Martinez-Lope, M. T. Casais and M. T. Fernandez-Diaz, Inorg. Chem. 39, 917 (2000).

[85] S. Quezel-Ambrunaz, Bull. Soc. Fr. Miner. Cristallogr. 91, 339 (1968).

[86] Y. Troyanchuk, N. V. Kasper, H. Szymczak and A. Nabialek, Low Temp. Phys. 23, 300 (1997).

[87] W. C. Koehler and E. Wollan, J. Phys. Chem. Solids 2, 100 (1957).

[88] F. Moussa, M. Hennion, R. Rodriguez-Carvajal, H. Moudden, L. Pinsard and A. Revcolevschi, Phys. Rev. B 54, 149 (1966).

[89] A. Munoz, J. A. Alonso, M. J. Martinez-Lope, J. L. Garcia-Munoz and M. T. Fernandez-Diaz, J. Phys.: Condens. Matter 12, 1361 (2000).

[90] S. Quezel, F. Tcheou, J. Rossat-Mignod, G. Quezel and E. Roudaut, Physica B 86, 916 (1977).

[91] N. A. Hill and A. Filippetti, J. Magn. Magn. Mater. 242, 976 (1998)

[92] O. Carp, L. Patron, A. Ianculescu, J. Pasuk, R. Olar, J. Alloys and Compounds, 351, 314 (2000).

[93] M. Fiebig, T. Lottermoser, D. Frohlich, A. V. Goltsev and R.V. Pisarev, Nature 419, 818 (2002).

[94] T. Lottermoser and M. Fiebig, Phys. Rev. B 70, 220407(R)(2004).

[95] A. B. Harries, Phys. Rev. B 76, 054447 (2007).

[96] G. A. Smolenskii and I. Chupis, Sov. Phys. Usp. 25, 475 (1982).

[97] N. A. Spaldin and M. Fiebig, Science 309, 391 (2005)

[98] R. I. Dass and J. B. Goodenough, Phys. Rev. B 67, 014401 (2003).

[99] Lei Bi, Alexander R. Taussig, Hyun-Suk Kim, Lei Wang, Gerald F. Dionne, D. Bono, K. Persson, Gerbrand Ceder, and C. A. Ross, Phys. Rev. B 78, 104106 (2008).

[100] S. Kamba1, D. Nuzhnyy, R. Nechache, K. Zaveta, D. Niznansky, E. antava, C. Harnagea, and A. Pignolet, Phys. Rev. B 77, 104111 (2008).

[101] M. N. Iliev, P. Padhan, and A. Gupta, Phys. Rev. B 77, 172303 (2008).

[102] M. P. Singh, K. D. Truong, and P. Fournier, Appl. Phys. Lett. 91, 042504 (2007).

[103] M. P. Singh, K. D. Truong, P. Fournier, P. Rauwel, E. Rauwel, L. P. Carignan, and D. Mnard, Appl. Phys. Lett. 92, 112505 (2008).

[104] Y. Du, Z. X. Cheng, S. X. Dou, X. L. Wang, H. Y. Zhao, and H. Kimura, Appl. Phys. Lett. 97, 122502 (2010)

[105] Hongyang Zhao, Hideo Kimura, Zhenxiang Cheng, Xiaolin Wang, and Takashi Nishida, Appl. Phys. Lett. 95, 232904 (2009).

[106] A. Inomata and K. Kohn, J. Phys.: Condens. Matter 8, 2673 (1996).

[107] Y. F. Popov, A. M. Kadomtseva, S. S. Krotov, G. P. Vorobev, and M. M. Lukina, Ferroelectrics 279, 147 (2002).

[108] G. Buisson, Phys. Status Solidi A 16, 533 (1973).

[109] G. Buisson, Phys. Status Solidi A 17, 191 (1973).

[110] P. P. Gardner, C. Wilkinson, J. B. Forsyth, and B. M. Wanklyn, J. Phys. C 21, 5653 (1988).

[111] C. Wilkinson, F. Sinclair, P. P. Gardner, J. B. Forsyth, and B. M. Wanklyn, J. Phys. C 14, 1671 (1981).

[112] V. Polyakov, V. Plakhty, M. Bonnet, P. Burlet, L. Regnault, S. Gavrilov, I. Zobkalo, and O. Smirnov, Physica B 297, 208 (2001).

[113] E. F. Bertaut, G. Buisson, S. Quezel-Ambrunaz, and G. Quezel, Solid State Commun. 5, 25 (1967).

[114] A. Muoz, J. A. Alonso, M. T. Casais, M. J. Martnez-Lope, J. L. Martnez, and M. T. Fernndez-Daz, Eur. J. Inorg. Chem. 20, 685 (2005).

[115] D. Higashiyama, S. Miyasaka, N. Kida, T. Arima and Y. Tokura, Phys. Rev. B 70, 174405 (2004).

[116] B. Mihailova, M. M. Gospodinov, B. Guttler, F. Yen, A. P. Litvinchuk, and M. N. Iliev, Phys. Rev. B 71, 172301 (2005).

[117] T. A. Tyson, M. Deleon, S. Yoong, and S.-W. Cheong, Phys. Rev. B 75, 174413 (2007).

[118] H. Tsujini and K. Kohn, Solid State Comm. 83, 639 (1992).

[119] A. K. Zvezdin and A. P. Pyatakov, Low Temp. Phys. 36, 532 (2010).

[120] J. Ravez, S. C. Abrahams, and R. de Pape, J. Appl. Phys. 65, 3987 (1989).

[121] Robert Blinc, Gaper Tavcar, Boris emva, Darko Hanel, Pavle Cevc, Cene Filipic, Adrijan Levstik, Zvonko Jaglicic, Zvonko Trontelj, Naresh Dalal, Vasanth Ramachandran, Saritha Nellutla, and James F. Scott, J. Appl. Phys. 103, 074114 (2008).

[122] E. Kroumova, M. I. Aroyo, J. M. Prez-Mato and R. Hundt, Acta Cryst. B. 57, 599-601 (2001).

[123] V. Andriamampianina, P. Gravereau, J. Ravez and S. C. Abrahams, Acta Cryst. B. 50, 135-141 (1994).

[124] S. Morup and N. Thrane, Solid State Comm. 11, 1319 (1972).

[125] J. van Suchtelen, Philips Res. Rep. 27, 28 (1972).

[126] J. Boomgard, D. R. Terrell, R. A. J. Born, and H. F. J. I. Giller, J. Mater. Sci. 9, 1705 (1974).

[127] J. Boomgard, A. M. J. G. Run, and J. Suchtelen, Ferroelectrics 10,295 (1976).

[128] G. Harshe, J. P. Dougherty, and R. E. Newnham, Int. J. Appl. Electromagn. Mater. 4, 145 (1993).

[129] S. Lopatin, I. Lopatin, and I. Lisnevskaya, Ferroelectrics 162, 63 (1994).

[130] M. I. Bichurin, I. A. Kornev, V. M. Petrov, and I. Lisnevskaya, Ferroelectrics 204, 289 (1997).

[131] R. E. Newnham, D. P. Skinner, and L. E. Cross, Mater. Res. Bull. 13, 525 (1978).

[132] X. M. Chen, Y. H. Tang, and I. W. Chen, J. Appl. Phys. 96, 6520 (2004).

[133] C. W. Nan, M. Li, and J. H. Huang, Phys. Rev. B 63, 144415 (2001).

[134] J. Ryu, S. Priya, A. V. Carazo, K. Uchino, and H. E. Kim, J. Am. Chem. Soc. 84, 2905 (2001).

[135] K. Mori and M. Wuttig, Appl. Phys. Lett. 81, 100 (2002).

[136] S. X. Dong, J. F. Li, and D. Viehland, J. Appl. Phys. 95, 2625 (2004).

[137] S. X. Dong, J. F. Li, and D. Viehland, Appl. Phys. Lett. 85, 2307 (2004).

[138] S. X. Dong, J. F. Li, and D. Viehland, J. Mater. Sci. 41, 97 (2006).

[139] C. W. Nan, G. Liu, and Y. H. Lin, Appl. Phys. Lett. 83, 4366 (2003).

[140] C. W. Nan, N. Cai, L. Liu, J. Zhai, Y. Ye, and Y. H. Lin, J. Appl. Phys. 94, 5930 (2003).

[141] N. Cai, J. Zhai, C. W. Nan, Y. H. Lin, and Z. Shi, Phys. Rev. B 68, 224103 (2003).

[142] Z. Shi, C. W. Nan, J. Zhang, N. Cai, and J. F. Li, Appl. Phys. Lett. 87, 012503 (2005).

[143] H. Zheng, J. Wang, S. E. Lo?and, Z. Ma, L. Mohaddes-Ardabili, T. Zhao, L. Salamanca-Riba, S. R. Shinde, S. B. Ogale, F. Bai, D. Viehland, Y. Jia, D. G. Schlom, M. Wuttig, A. Roytburd, and R. Ramesh, Science 303, 661 (2004).

[144] R. Ramesh and N. A. Spaldin, Nat. Mater. 6, 21 (2007).

[145] J. G. Wan, X. W. Wang, Y. J. Wu, M. Zeng, Y. Wang, H. Jiang, W. Q. Zhou, G. H. Wang, and J. M. Liu, Appl. Phys. Lett. 86, 122501 (2005).

[146] M. P. Singh, W. Prellier, L. Mechin, C. Simon, and B. Raveau, J. Appl. Phys. 99, 024105 (2006).

f

2 Experimental Techniques

The current chapter briefly describes different techniques to synthesize bulk and nanostructures (such as thin films, nanowires and nanotubes) of $BiFeO_3$ (BFO). Also we will discuss different characterization techniques we have used to investigate the properties of $BiFeO_3$.

2.1 Materials Fabrications

2.1.1 Chemical Synthesis Route: Bulk Material

Chemical synthesis is a very simple and straight forward method for synthesizing complex oxide materials. Higher compositional homogeneity and better stoichiometry can be achieved by this technique by controlling the sintering temperature.

To prepare the Ba doped samples with composition $Bi_{1-x}Ba_xFeO_3$ (x = 0.0, 0.10, 0.15, 0.20 and 0.25), starting chemicals $Ba(N0_3)_2$, $Bi(N0_3)_3$ and $Fe(N0_3)_3$ were weighed according to the stoichiometric compositions. These Ba doped samples are denoted as Ba_xBFO in the thesis. Gd and Ba co-doped samples with composition $Bi_{1-x}Ba_xFe_{1-y}Gd_yO_3$ ($0 \leq$ x,y ≤ 0.1 i.e. $Gd_{0.05}$BFO, $Ba_{0.05}Gd_{0.05}$BFO, $Ba_{0.05}Gd_{0.1}$BFO and $Ba_{0.1}Gd_{0.05}$BFO) were also prepared by chemical synthesis route in ambient atmosphere. Here $Ba(N0_3)_2$

, $Gd(N0_3)_3$, $Bi(N0_3)_3$ and $Fe(N0_3)_3$ were weighed according to the stoichiometric compositions to prepare the samples. All nitrates with high purity ($> 99.99\%$) were first dissolved in aqueous medium individually than the clear solution of these chemicals were mixed and dried up at 80 °C. The dried mixture was pressed in to pallets at high pressure and sintered in the furnace (at 500 °C for Ba doped samples and at 750 °C for Ba and Gd co-doped samples) for 4 hrs. After that the products were crushed, ground, mixed well, again pressed into pallets and sintered at higher temperatures (between 865 °C to 885 °C for 2 to 3 hrs) for several times to get the phase pure samples.

2.1.2 Pulsed Laser Deposition (PLD) Technique: Thin Films

There are many thin-film growth techniques (such as pulsed laser deposition (PLD), RF magnetron sputtering, chemical vapor deposition (CVD), metal-organic CVD (MOCVD), chemical solution deposition (sol-gel), molecular beam epitaxy (MBE) etc.) to synthesis high-quality thin-film samples with the designs required for the application purposes. We have used PLD technique to deposit undoped and Ba doped $BiFeO_3$ thin films on Si(100) substrates.

PLD is a very old technique to deposit high quality films [1]. High power laser pulse is used to melt, evaporate and ionize material from the surface of a target. This "ablation" event produces a transient, highly luminous plasma plume that expands rapidly away from the target surface. The ablated material is collected on an appropriately placed substrate upon which it condenses and the thin film grows. The target material which is evaporated by the laser is normally found as a rotating disc attached to a support. This process can occur in ultra high vacuum or in the presence of a background gas, such as oxygen which is commonly used for oxide materials.

Thin film growth kinematics by PLD depends on several growth parameters such as:

- **Laser parameters:** several factors such as laser energy, laser fluence (Joule/cm^2) and ionization degree of the ablated material affect the film quality and the stoichiometry.

- **Substrate temperature:** The surface temperature of the substrate has an influence on the nucleation density. Generally, the nucleation density decreases as the temperature is increased. Post annealing of the film is also has an effect on the film stoichiometry.

- **Substrate surface:** lattice mismatch between the target and substrate and also the roughness of the substrate effects the nucleation and growth of the film.

- **Background pressure:** In case of oxide deposition, proper oxygen pressure in the deposition chamber is needed to ensure stoichiometric transfer from the target to the film.

- Distance between the target and substrate and repetition rate also have to optimize to get a high-quality thin-film.

The deposition of the undoped and Ba doped $BiFeO_3$ films was carried out in a pulsed laser deposition chamber, using a KrF excimer laser with a wavelength of 248 nm on silicon (100) substrate. High purity powder samples of $BiFeO_3$ and $Bi_{1-x}Ba_xFeO_3$ were prepared from the nitrate salts ($>99.9\%$, Sigma-Aldrich) of Bi, Fe and Ba using previously mentioned chemical synthesis route. Pellet of these powders, with diameter 2.54 cm and thickness 1 cm was used as the targets for the thin films. An oxygen pressure of 3×10^{-1} mbar, a repetition rate of 3 Hz and a laser fluency of 4J/cm^2 was maintained during film deposition. To get phase pure film, temperature of the substrate was maintained at 650 °C during film deposition. After deposition, the film was cooled down to 300 °C and annealed at that temperature for 1 hr in oxygen atmosphere.

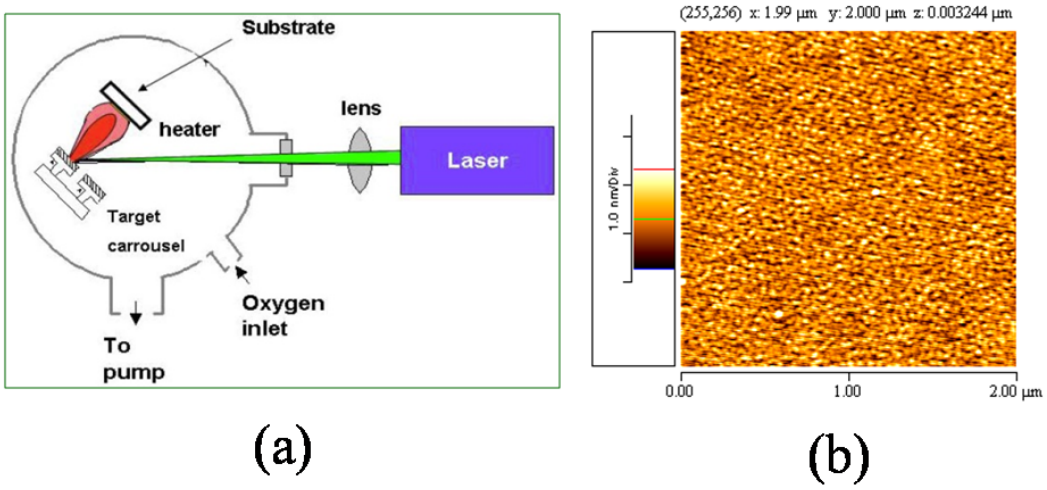

Figure 2.1: (a) Schematic diagram of PLD set up and (b) Topography of Ba doped $BiFeO_3$ thin film fabricated by PLD technique.

Keeping all the above parameter fixed, deposition time was varied to synthesize films with different thickness. Fig 2.1(a) shows the schematic diagram of PLD set up and Fig 2.1(b) shows the topography of Ba doped $BiFeO_3$ thin film fabricated by PLD technique.

The background magnetic contribution of the Si substrate is subtracted from all of the magnetization data of the film. Au layer of ~ 0.5 mm diameter is deposited through a shadow mask at room temperature (RT) on both side of the film to perform the electrical measurements.

2.1.3 Template Assisted Wet Chemical Liquid Phase Deposition Technique: Nanowires/Nanotubes

In this process nanowires (NWs) and nanotubes (NTs) were prepared in the nanoporous aluminium oxide (AAO) template (Fig 2.2). Self-ordered AAO template was fabricated by two-stage electrochemical anodization of high purity ($> 99.99\%$) aluminium foil by

critically controlling the anodization parameters, as reported elsewhere [2, 3]. In brief, after the electropolishing of aluminium foil required for its surface smoothing, anodization was carried out in 3wt% phosphoric acid solution at 10 °C maintaining a current density of 300 Am^{-2} by varying the dc anodization voltage between 65-70 V for 3 hr in order to fabricate the AAO template of large pore diameter. The oxide layer grown on the aluminium surface after the first stage of anodization for 20 min was removed through chemical etching [3]. After anodization was over the remaining aluminium part attached with the AAO was dissolved in $HgCl_2$ solution. AAO was dipped inside the 10% H_3PO_4 solution for 40 min for pore opening and rounding and then it was cleaned several times in double-distilled water to prepare the template ready for the growth of $BiFeO_3$ NTs/NWs.

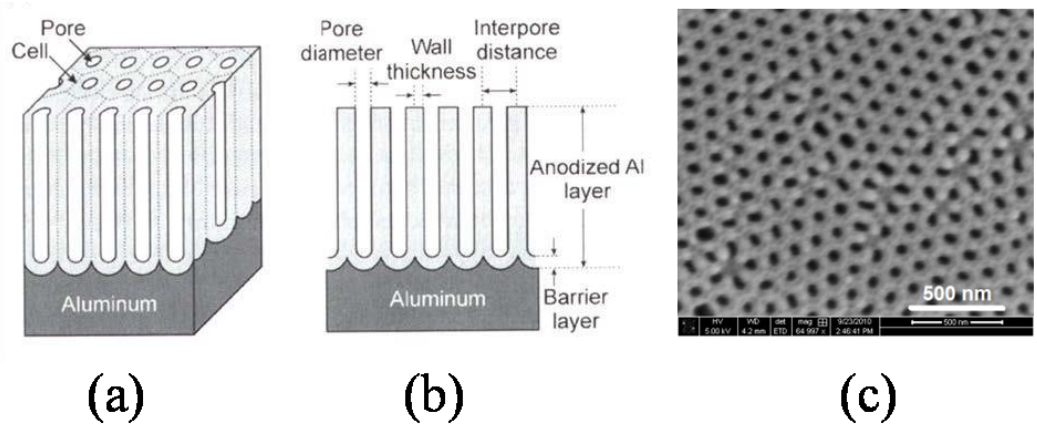

Figure 2.2: (a) Schematic diagram of idealized structure of porous alumina template obtained from anodization of thin aluminum sheet, (b) a cross sectional view of the anodized layer (The figure is taken from Ref. [4]) and (c) FESEM image of porous AAO template (top view).

To prepare the arrays of $BiFeO_3$ NWs/NTs within the nanopores AAO, firstly solution of $BiFeO_3$ was prepared by dissolving equimolar high purity bismuth nitrate [$Bi(NO_3)_3.\ 5H_2O$] and ferric nitrate [$Fe(NO_3)_3.\ 9H_2O$] in 2-methoxyethanol ($C_3H_8O_2$)

followed by constant stirring of the mixture for about 30 min at RT. The concentration of the final solution was adjusted to 0.3 M and the pH of the solution to 1-2. Afterwards the AAO template was immersed inside the solution of the compound for long time to help the sol to reach inside the pores of the template. Concentration and pH of the solution had to control to get a phase pure sample. Afterwards, the template was removed from the solution and its surface was washed carefully to remove the sol from the template surface and it was dried under IR lamp. Finally the sol filled AAO template was annealed to crystalline the NWs/NTs. Finally, the $BiFeO_3$ NWs/NTs were fabricated through annealing of the sol filled AAO template at 500 °C for 2 hr in air. For synthesizing the doped $BiFeO_3$ NWs/NTs, the method was similar to that reported for undoped $BiFeO_3$ but here an appropriate stoichiometric amount of chromium nitrate [$Cr(NO_3)_3$. $9H_2O$], praseodymium nitrate [$Pr(NO_3)_3$. $6H_2O$] and their mixture was added to the solution of $Bi(NO_3)_3$ and $Fe(NO_3)_3$ to fabricate the Cr-doped $BiFeO_3$ NTs ($BiFe_{0.9}Cr_{0.1}O_3$ ($Cr_{0.1}$BFO)), Pr-doped $BiFeO_3$ NWs/NTs ($Bi_{0.9}Pr_{0.1}FeO_3$ ($Pr_{0.1}$BFO)) and the Cr-Pr co-doped $BiFeO_3$ NWs/NTs ($Bi_{0.9}Pr_{0.1}Fe_{0.9}Cr_{0.1}O_3$ ($Pr_{0.1}Cr_{0.1}$BFO)), respectively.

For the SEM and TEM measurements, the NWs/NTs were released from the pores of AAO by dissolving the template in 2 M NaOH solution. In case of M-H measurements, magnetic contribution of the AAO template was subtracted from the contribution of the template embedded pure and doped $BiFeO_3$ NWs/NTs to get the actual magnetization value of the NWs/NTs.

2.2 Sample Characterization

2.2.1 Structural and Surface Morphology Characterization Techniques

The crystal structure and the surface morphology of the synthesized samples were characterized using powder X-Ray Diffraction (XRD), X-ray photoelectron spectroscopy (XPS), imaging techniques like Scanning Electron Microscopy (SEM), Transmission Electron Microscopy (TEM), Atomic force microscopy (AFM) and the stoichiometry was checked using Energy Dispersive X-ray analysis (EDAX).

2.2.1.1 X-Ray diffraction (XRD)

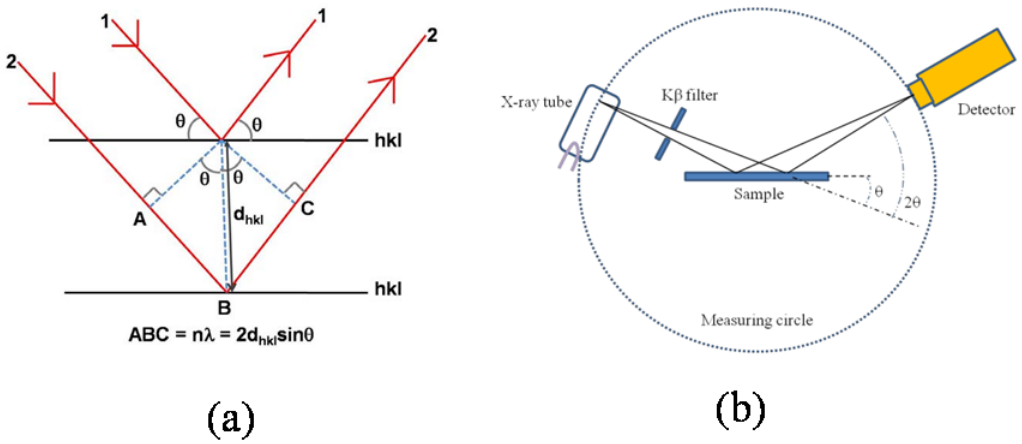

Figure 2.3: (a) Bragg's law and (b) Schematic diagram of X-ray diffraction optics used in $\theta - 2\theta$ mode.

X-ray diffraction (XRD) is one of the most well known analytical techniques to study crystallographic structure, chemical composition and physical properties of the materials. X-rays are generated by a cathode ray tube, filtered to produce monochromatic radiation,

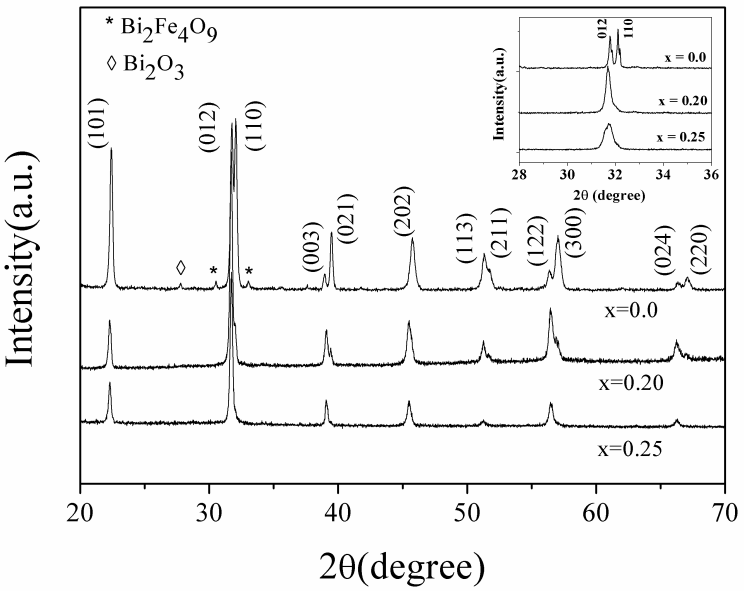

Figure 2.4: XRD pattern obtained from Ba doped $Bi_{1-x}Ba_xFeO_3$ samples

collimated to concentrate, and directed toward the sample [5]. The atomic planes of a crystal cause an incident beam of X-rays to interact with one another as they leave the crystal. The interaction produces constructive interference (and a diffracted ray) when it satisfy Bragg's Law,

$$2dsin\theta = n\lambda \tag{2.1}$$

English physicists Sir W.H. Bragg and his son Sir W.L. Bragg developed this relationship in 1913 to explain why the cleavage faces of crystals appear to reflect X-ray beams at certain angles of incidence (θ, q). The variable d is the distance between atomic layers in a crystal, and the variable λ is the wavelength of the incident X-ray beam, n is an integer. Bragg's law is illustrated in Fig 2.3(a). The condition, $2dsin\theta = n\lambda$ is derived from simple geometry (as can be seen from the figure 2.3(a)).

In order to determine the phase and the orientation of the prepared samples (ceramics, thin films and nanowires), experimental diffraction patterns can be compared with the JCPDS (Joint Committee on Powder Diffraction Standard) database or with some

other standard data base. Each crystallographic plane has three indices h, k, l. Hence with the help of the data base each plane can be indexed with different hkl.

We have used Panalytical (X'Pert Pro) system with a CuKα radiation ($\lambda = 1.54$ Å) for characterising all the samples. This is a $\theta - 2\theta$ system in which the X-ray tube is fixed, and the specimen moves at half the rate of the detector to maintain the $\theta - 2\theta$ geometry as shown in the diagram in Fig 2.3(b). Fig 2.4 shows a XRD pattern obtained from Ba doped $Bi_{1-x}Ba_xFeO_3$ samples.

2.2.1.2 X-ray photoelectron spectroscopy (XPS)

X-ray photoelectron spectroscopy (XPS) is a quantitative spectroscopic technique that works by irradiating the surface of a sample material with monoenergetic soft x-rays causing the core electrons to be ejected [6, 7]. XPS is truly based on Einsteins idea about the photoelectric effect, developed around 1905. The technique was developed in the mid 1960s by Kai Siegbahn and his research group at the University of Uppsala, Sweden. One can obtained the composition, chemical state empirical formula and electronic state of the components of a material using this technique.

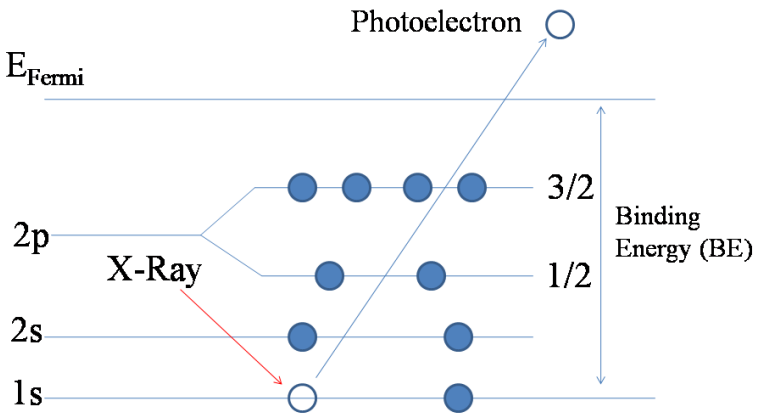

Figure 2.5: Schematic diagram of XPS mechanism [8]

The relationship governing the interaction of a photon of the X-ray with a core level electron is:

$$KE = h\nu - BE - e\Phi \tag{2.2}$$

where, KE is the kinetic energy of the ejected photoelectron (measure in the XPS spectrometer), $h\nu$ is the characteristic energy of X-ray photon, BE is the Binding Energy of the atomic orbital from which the electron originates and $e\Phi$ is the spectrometer work function. The kinetic energies of these ejected photoelectrons (Fig 2.5) give the information of the elements in the sample and the intensities of the photoelectron is proportional with the relative concentrations of elements in the sample. XPS data is helpful to obtain information on chemical states from the variations in binding energies or chemical shifts, of the photoelectron lines.

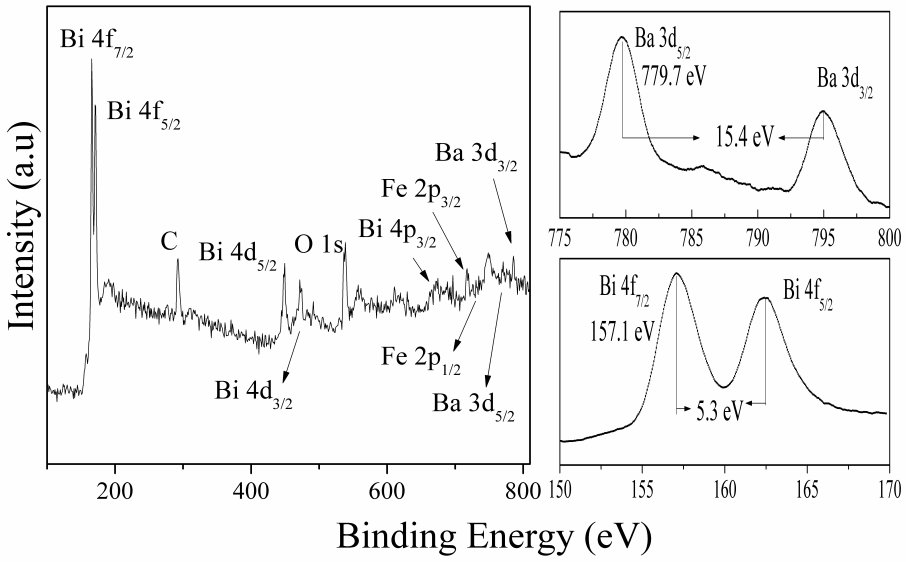

Figure 2.6: Experimentally measured XPS spectra of $Bi_{0.9}Ba_{0.1}FeO_3$ sample.

As for each and every element, there is a characteristic binding energy associated with each core atomic orbital i.e. each element gives rise to a characteristic set of peaks in the photoelectron spectrum at kinetic energies determined by the photon energy and the

respective binding energies [9]. We have performed XPS measurements of the valance state of the ions in our samples using XPS VG Microtech ESCA-2000 Multilab apparatus with a non-monochromatic Mg Kα (1253.6 eV) excitation source at Indian Institute of Physics (IOP), Bhubaneswar, with the help of Prof. Shikha Verma. Initially, the sample is scanned by the incident x-ray photon energy which falls gradually from 1253.6 eV to 0 eV and it gives the information about the presence of various constituent elements within the sample. After that the individual elemental high resolution spectrum is collected one by one. Fig 2.6 shows survey scan of $Bi_{0.9}Ba_{0.1}FeO_3$ sample in the energy range between 0 to 800 eV and high resolution XPS spectra of Ba 3d and Bi 4f core level. The spectra explores that Ba and Bi are in +2 and +3 valence state in the sample respectively.

2.2.1.3 Scanning Electron Microscopy (SEM)

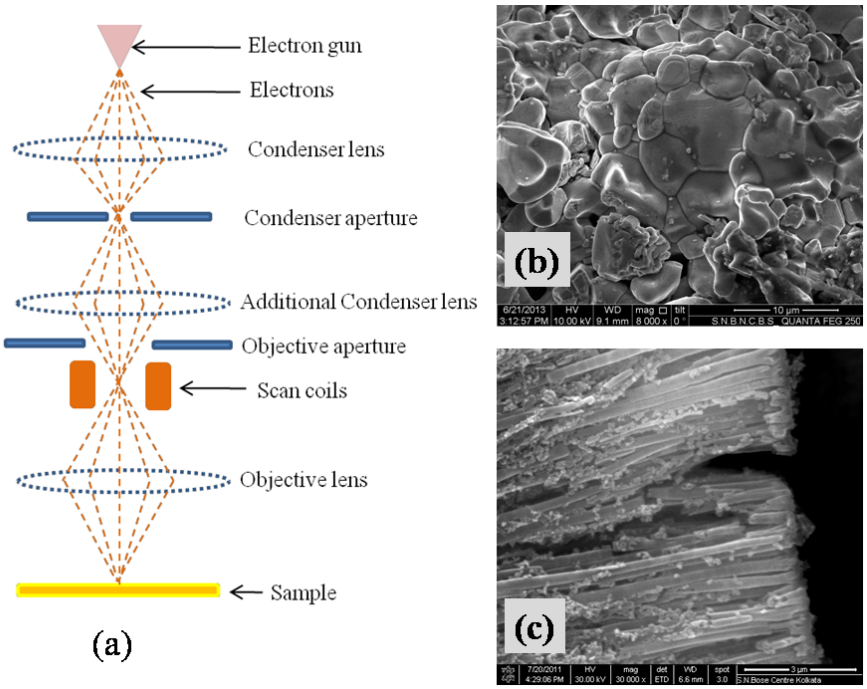

Figure 2.7: (a) Schematic diagram of a SEM unit, (b) SEM image of $BiFeO_3$ ceramics and (c) SEM image of $BiFeO_3$ nanowires.

SEM is the most widely used instrument for obtaining the topographical features (such as grain size, distribution of the particles etc.) of the sample surface. A beam of highly energetic electrons are used to examine objects at sub-micrometer length scale [10].

The basic steps involved here are the following: a stream of electrons is formed in high vacuum (by electron guns). The stream is accelerated towards the specimen (with a positive electrical potential) and is confined, focused and directed in a particular direction using metallic charged plates and magnetic lenses resulting in a monochromatic beam. In SEM (schematically shown in Fig 2.7(a)), the electron beam is either thermoionically or field emitted from an electron gun [11] and focused in vacuum into a fine probe that is rastered over the surface of the specimen. As it incidents on the sample, it interacts with the atoms of the sample and affecting the electron beam. These interactions and effects are detected and transformed into an image. SEM works on a voltage between 2 to 50 kV and its beam diameter that scans the specimen is 5 nm-2 μm. A field-emission cathode in the electron gun of a SEM (FESEM) provides narrower probing beams at low as well as high electron energy. When, the electron beam interacts with the sample, the energy exchange between the electron beam and the sample results deceleration of incident electrons through the energy dissipation and produces a variety of signals which include secondary electrons (SE), back-scattered electrons (BSE), characteristic X-rays, visible light (cathod-luminescence) (CL), specimen current and transmitted electrons. Secondary and backscattered electrons are conventionally separated according to their energies [12]. The electrons are detected by suitable detectors placed in the microscope in proper positions. The sample (such as ceramics and nanowires) preparation include a thin gold coating on the sample (mainly for electrically non conducting samples, e.g., $BiFeO_3$) to avoid static charge accumulation during SEM imaging. Characteristic X-rays are used for elemental analysis. The process is known as energy dispersive analysis of

X-ray (EDAX). Due to high energetic and narrower beam, field emission SEM (FESEM) results in both improved spatial resolution and minimized sample charging and damage. A JEOL scanning electron microscope system (JSM 6700 F)is used for the present study. Fig 2.7(b) and (c) show the SEM micrographs of $BiFeO_3$ ceramics and $BiFeO_3$ nanowires, respectively.

2.2.1.4 Transmission Electron Microscopy (TEM)

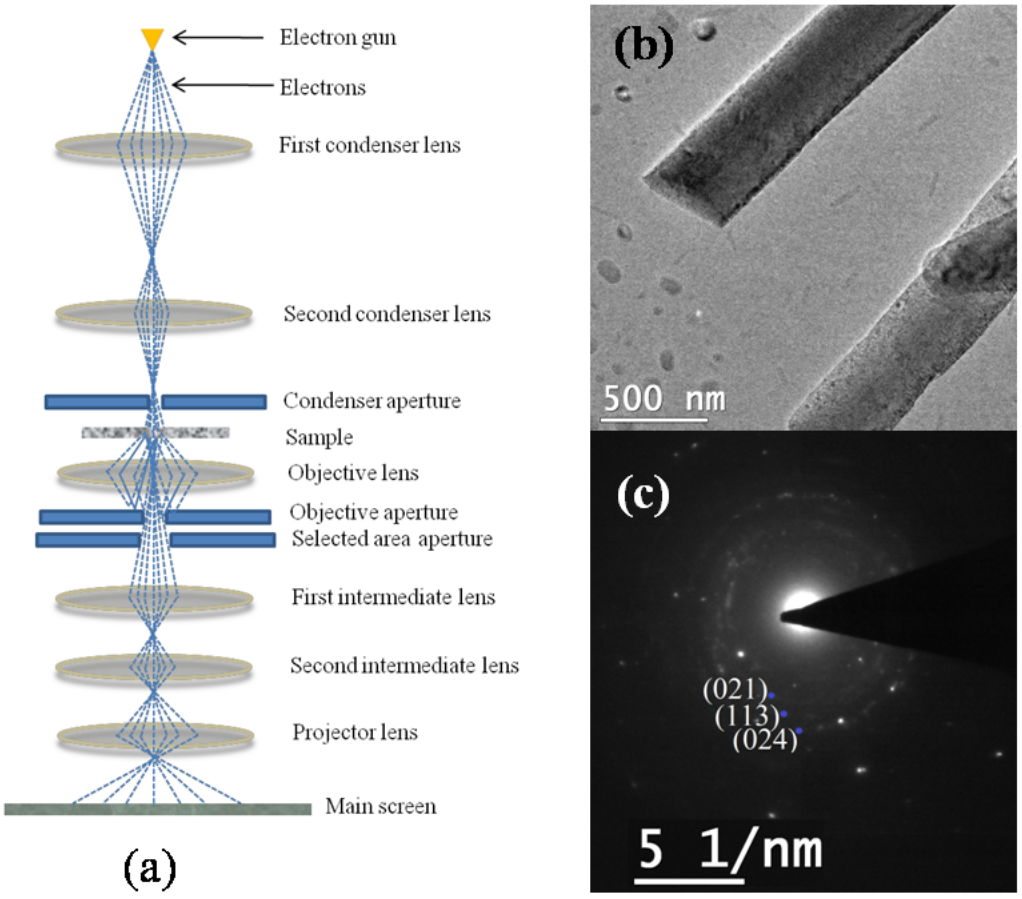

Figure 2.8: (a) Schematic diagram of a TEM unit, (b) TEM micrograph of $BiFeO_3$ nanowires and (c) SAED patterns of same $BiFeO_3$ nanowires.

The Transmission Electron Microscope (TEM) is the first type of EM developed in

1931 which is a versatile instrument, capable of characterizing the internal structure of materials with a wide range of imaging and analytical methods. It uses diffraction of electrons to image materials. Schematic diagram of a TEM is shown in Fig 2.8(a).

In TEM, a beam of electrons (with a typical wavelength of less than 1 Å) is sent through a thin specimen without any interaction occurring inside the specimen. A fraction of the electrons in the beam get either elastically or inelastically scattered. One is the scattered (diffracted beam) electrons by atoms in the specimen in an elastic fashion (no loss of energy). Thus, while passing through the specimen, in case of crystalline samples the electron beam undergoes diffraction according to Bragg's law. Here, the incident electrons have the same energy (thus wavelength) and enter the sample normal to its surface. All electrons that are scattered by the same atomic spacing will have same scattering angle. These scattered electrons can be collated using magnetic lenses to form a pattern of spots, each spot corresponding to a specific atomic spacing (or crystalline plane). This pattern can then yield information about the orientation, atomic arrangements and phases present in the area of the sample being examined.

Another is unscattered electrons (transmitted beam) which produce a two dimensional image of the sample. The transmission of this unscattered electrons is inversely proportional to the specimen thickness. Areas of the specimen that are thicker will have fewer transmitted unscattered electrons and so will appear darker, conversely the thinner areas will have more transmitted and thus will appear lighter. This mode of operation to create contrast in image is known as bright field imaging mode. In order to take microscopic images of ferromagnetic nanowires (NWs), we place them on carbon grids (fine two dimensional mess of copper covered with carbon) that are specially made for TEM imaging purpose [13]. Standard TEM grid has typical diameter of $\sim$3.05 mm with a thickness of few micrometer and mesh size ranging from a few to 100 μm. Pretreatments of the NWs are done before placing them on carbon grid. In case of

NWs, alumina template that is used to prepare the NWs is dissolved chemically using 2M NaOH. Released NWs are then washed carefully using distilled water and then the residual is ultra sonicated in ethyl alcohol for few minutes to detach the magnetic NWs from each other partially. Fig 2.8(b) shows the TEM micrograph of $BiFeO_3$ NWs using a high resolution TEM or HRTEM (JEOL-2010) system.

Bragg's law is used to indexing the diffraction patterns. The radius of circular rings (Fig 2.8(c)) in the diffraction patterns are measured using the microscopic length scale. For spot patterns, the distances of the diffracted spots from the central spot is measured. These distances correspond to the interplanar spacing of the diffracting planes. Thus, by measuring R and calculating the corresponding plane spacing (d_{hkl}), the diffraction pattern can be indexed with the standard diffraction data of the corresponding elements or compounds provided by ICSD (Inorganic Crystal Structure Database) [14].

2.2.1.5 Scanning Probe Microscopy (SPM)

Scanning probe microscopy (SPM) produces images of sample surfaces using a physical probe that scans the specimen on scales ranging from 100 μm to 10 pm [15]. SPM was founded with the introduction of the scanning tunneling microscope (STM) in 1986 [16]. SPM is a very essential instrument to observe the morphology of the sample surface, distribution of point defects and structural defects with the atomic resolution. So it became a necessary tool in the field of nanoscience and nanotechnology. In this thesis, several SPM techniques such as AFM, PFM and MFM have been used for the characterization of the thin film and nanowires using a Vecco-3100 scanning probe microscope set up.

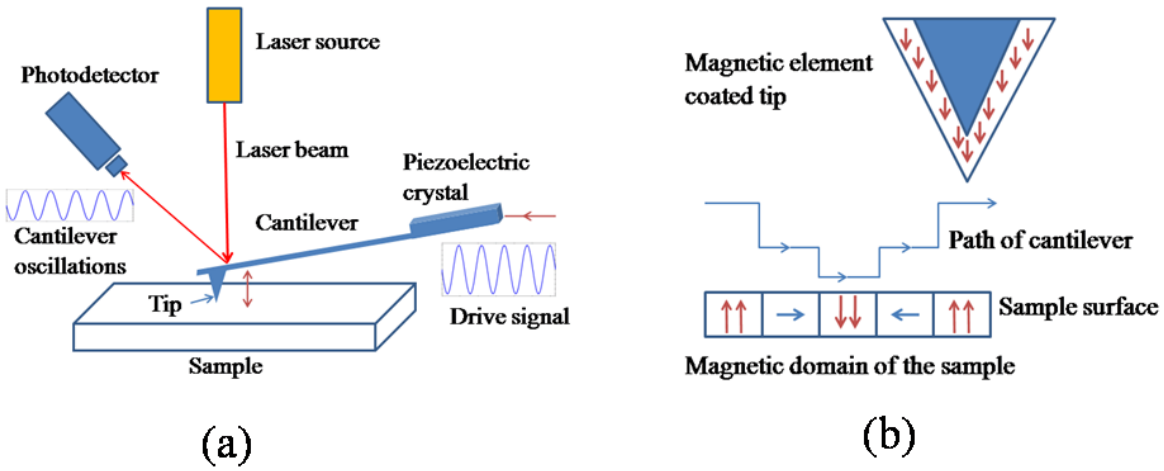

Figure 2.9: Schematic diagram of (a) Atomic force microscopy (AFM) and (b) Magnetic force microscopy (MFM) system.

Atomic force microscopy (AFM)

AFM is a very high resolution (of the order of Å) type scanning probe microscope which helps to measure and observe the topography of the sample on the nanoscale range. In AFM the information about the sample topography is collected through the interaction between the sample surface and the mechanical probe during the measurement.

Here the probe is a very tiny sharp tip at the end of a cantilever. Cantilever can be made of single-crystalline silicon, silicon dioxide (SiO_2), or silicon nitride (Si_3N_4). The force between the surface and the probe can be measured in two different modes. One, contact mode in which the tip is directly in contact with the sample surface and the interaction force is dominated by Van der Waal's interaction. The other mode is the tapping mode which is a non contact mode. A drive signal is applied by a piezoelectric crystal with typical frequencies ranging from 10 kHz to 1 MHz [17] to the "Tapping Piezo", mechanically oscillates the probe at or near its resonance frequency. The interaction between the tip and the surface changes the cantilever oscillation amplitude or

the phase relative to the Drive Signal (see schematic in Fig 2.9(a)).

Magnetic force microscopy (MFM)

In case of MFM, the AFM tip is coated with a thin (<50 nm) magnetic film (such as Ni or Co), which have negligible coercivity, so that the tip's magnetic state (or magnetization, M) does not change during the imaging. The magnetic tip is sensitive to the out-of-plane component of the stray field originating from a magnetic sample (e.g. from a domain wall) and each scan line is recorded twice. First, the topographic information of the line is recorded using the AFM Tapping Mode. This information is used during the second scan in order to keep the cantilever always at a certain probe sample distance, called Lift Height. During this scan the magnetic tip is only sensitive to the magnetic stray field from the sample. Therefore the combination of these two modes enables an accurate localization of the magnetic stray fields coming from the magnetic structure. The stray magnetic field from the sample can affect the magnetic state of the tip, and vice versa. Typical resolution of 30 nm can be achieved [18], although resolutions as low as 10 to 20 nm are attainable [19]. Thus, interpretation of the MFM measurement is not straightforward. Fig 2.9(b) shows schematic diagram of the magnetic tip movement over a magnetic sample. In MFM micrographs, the bright and dark spots correspond to the local magnetic stray field of the sample either in the upward or in the downward direction with respect to sample's horizontal surface.

Piezoresponse force microscopy (PFM)

In case of PFM, the AFM tip is coated with a thin conducting material for the imaging of the ferroelectric domains in the sample. The working principle in PFM is when the sharp conductive probe comes into contact with a ferroelectric surface (or piezoelectric

material) and an alternating current (AC) is applied to the probe, excite deformation of the sample occur through the converse piezoelectric effect (CPE). This deflection of the probe cantilever is detected through standard split photodiode detector. Here also topography and ferroelectric domains can be imaged simultaneously with high resolution.

2.2.2 Optical Properties Measurement Techniques

2.2.2.1 Photoluminescence (PL) Spectroscopy

Photoluminescence (PL) spectroscopy is a very commonly used tool to identify various energy levels within the energy gap of semiconducting materials. A monochromatic light from Xe lamp is used to excite the electrons in valence band. If the incident photon energy ($E = hc/\lambda$) is greater than the band gap energy, then it can be absorbed by the valence band electrons which goes up to the conduction band crossing the forbidden energy gap. During the photoexcitation, the electrons generally have excess energy which loses during coming to rest at the lowest energy in the conduction band. At this point the electron eventually falls back down to the valence band or nearby acceptor states arises due to different defect levels. Similarly, electrons can also fall from the various donor impurity states near to the conduction band. As they (electrons) fall down, the energy associated is emitted as luminescent photons which are emitted from the material. The process of photon excitation followed by photon emission is called photoluminescence.

In the doped samples various dopant substitutional defects can grow within the lattice and their (defects) respective energy level lies within the energy band gap of the host materials. Acceptor impurity or defect states lie near to valence band maxima while the donor defects reside below the conduction band minima. Thereby these defect (acceptor or donor or both) levels also get involved and the associated electronic

transitions can generate the characteristic luminescence in the visible region of the electromagnetic radiation energy spectrum. Therefore by investigating such characteristic luminescence, it is possible to identify the presence of various defects within the materials. We have conducted PL measurement for all the undoped and doped NWs samples using a spectrofluorometer (Horiba Jobin Yvon, Fluorolog-3) having Xe lamp source.

2.2.2.2 Raman Spectroscopy

Raman spectroscopy is a very effective and sensitive tool for characterization of molecular structure, identifying phase purity, chemical bonding and stress on the samples. In Raman scattering technique a photon of light interacts with the lattice or molecules and produces scattered waves of different wavelengths. When a monochromatic light is incident on the sample, it interacts with the lattice phonons in the following ways: the light may be reflected, absorbed or scattered. Raman measurement is based on the analysis of the scattered radiation. This scattered radiation can be divided into elastic and inelastic components. Rayleigh scattering is an elastic process i.e scattering without a change in frequency of the light. Whereas, a change in the frequency of light is Raman scattering. Depending on the vibrational state of the molecules, the frequency of this scattered light can be higher or lower.

When an incident photon with wave vector k_i and frequency ω_i interacts with the lattice it creates a electron-hole pair via electron radiation interaction. These electrons recombines with the hole by creating a phonon (wave vector k and frequency ω) via electron-lattice interaction. Following the conservation rule, the scattered photon frequency and wave vector can be written as,

$$\begin{aligned} \omega_s &= \omega_i \pm \omega \\ k_s &= k_i \pm k \end{aligned} \tag{2.3}$$

If $\omega_s < \omega_i$, it is called stokes scattering and if $\omega_s > \omega_i$, it is anti-stokes scattering. This change in frequency is called Raman shift which provides the chemical and structural information such as on bond vibration of the material. This bond vibrational energy is useful for the analysis of the magnetoelectric coupling in the multiferroic material induced by the structural distortion.

Raman spectroscopy measurements were carried out in the range 50-1000 cm^{-1} using the micro-Raman spectrometer (LABRAM HR from Horiba Jobin Yvon) at IISER, Kolkata with the help of Prof. Goutam Dev Mukherjee.

2.2.3 Magnetic Properties Measurement Techniques

All of the magnetic properties measurements were carried out using a commercial vibrating sample magnetometer (VSM) [20, 21] and a Quantum Design superconducting quantum interference device (SQUID) magnetometer [22].

2.2.3.1 Vibrating Sample Magnetometer (VSM)

Vibrating sample magnetometer (VSM) is a very sensitive and versatile instrument which can measure a very low magnetic moment upto a order of 10^{-5} emu. Vibrating sample magnetometer (VSM) is based on the flux change in a coil due to the vibration of a magnetized sample near it. Faraday's law of induction states that an electromotive force (*EMF*), 'V' will be generated in a coil if there is a change in flux, B linking the coil. For a tightly wound coil of wire, composed of N identical loops and a cross-sectional area of A, the induced *EMF* in the coil can be written as,

$$V = -nA(dB/dt) \tag{2.4}$$

The direction of the *EMF* is given by Lenz's law. If the coil is positioned in a constant magnetic field H, the flux around it is given by,

$$B = \mu_0 H \tag{2.5}$$

where, μ_0 is permeability of vacuum. Now if we place a magnetic sample having magnetization M near the coil, then the flux will be,

$$B = \mu_0 (H + M) \tag{2.6}$$

Thus the corresponding flux change is given by,

$$\Delta B = \mu_0 M \tag{2.7}$$

The induced *EMF* in pick-up coils expressed at the beginning thus can be rewritten as

$$V dt = -NA\mu_0 M \tag{2.8}$$

The above equation implies that the output signal of the coil is proportional to the magnetization M of the sample and independent of the magnetic field in which the magnitude of M is to be determined. Schematic diagram of a VSM is shown in Fig 2.10(a) (reproduced from [16]). In a VSM, the sample to be measured is centered in the region between the poles of an electromagnet which can generate a uniform magnetic field H_0. A thin vertical nonmagnetic sample rod (made of plastic/quartz) connects the sample holder with a transducer assembly located above the magnet. The transducer converts a sinusoidal signal as drive signal (generated by an oscillator/amplifier circuit) into a sinusoidal vertical vibration (of frequency ν) of the sample rod. The sample is thus subjected

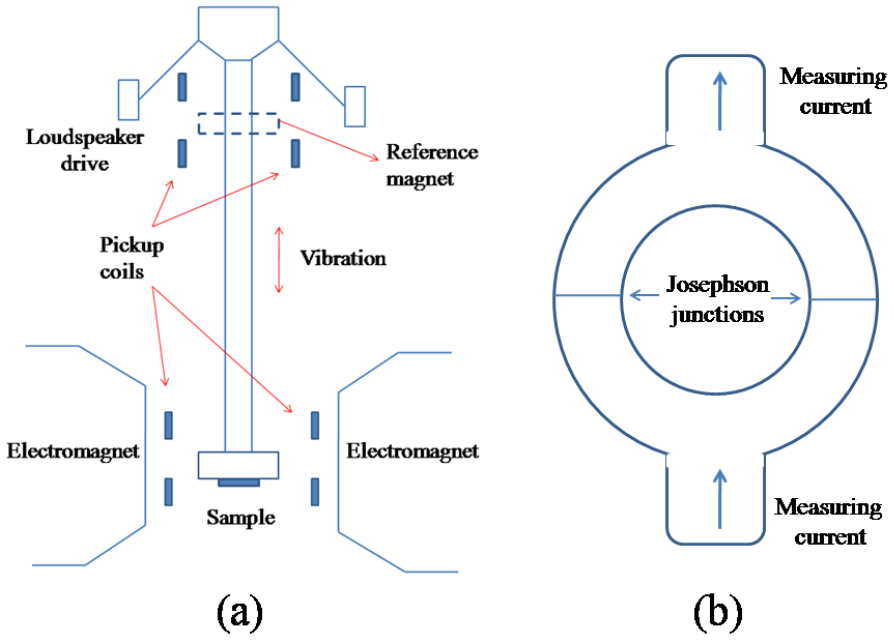

Figure 2.10: Schematic diagram of (a) Vibrating sample magnetometer (VSM) and (b) Superconducting quantum interference device (SQUID) flux sensor.

to a sinusoidal motion in the magnetic field H_0. The oscillating magnetic field of the vibrating sample induces an alternative *EMF* in the detection coils or pick up coil (made of copper and mounted on the poles of the magnet) whose magnitude is proportional to the magnetization of the sample. This alternative *EMF* is amplified using a lock-in amplifier. However, though the *EMF* signal in the pick-up coil at a vibration frequency ν is proportional to the magnitude of the moment of the sample, it is also proportional to the vibration amplitude and frequency. Thus the moment readings taken simply by measuring the amplitude of the signal are subject to errors due to variation in amplitude and frequency of vibration. In order to avoid this difficulty, a nulling technique is introduced employing a vibrating capacitor for generating a reference signal that varies with moment, vibration amplitude and frequency in the same manner as the signal from the pickup coils. When these two signals are processed in an appropriate manner, it is possible to eliminate the effects of vibration amplitude and frequency shifts. In that

case, one obtains readings that vary only with the moment of the sample.

For the measurement of the magnetic properties of all our samples a Lakeshore make VSM (Lake Shore Cryotronics) is used which has maximum magnetic field generating capability of 2.1 T without cryogenic system and 1.76 T can be achieved with LN_2/LHe dewar between the coils. The moment versus temperature and isothermal hysteresis loops at various temperatures (80 to 400 K for low temperature measurements using a cryogenic system (Liquid N_2) and RT to 1273 K for high temperature measurements) can be measured with temperature stability of ± 0.2 K and temperature resolution of 0.001 K. Noise level of 1.25 μemu (RMS value) in moment measurement can be achieved using the system [23].

2.2.3.2 Superconducting Quantum Interference Device (SQUID) Magnetometer

SQUID magnetometers have a higher sensitivity than VSMs. Here the resolution obtained in a SQUID magnetometer is of the order of 10^{-8} emu. As such, we use SQUID magnetometer for measuring those samples which have a lower magnetic moment (specially nanowires (NWs) due to the diamagnetic AAO template). The working principle of this device is mainly based on the tunneling of superconducting electrons (the Cooper pairs) across a very narrow insulating gap, called as Josephson junction, between two superconductors [24]. A sketch of the device in its usual form is shown in the Fig 2.10(b) (reproduced from Ref. [16])

The components of a SQUID magnetometer typically consist of the following: A superconducting measuring current flows through the ring, so that total supercurrent is divided into two part and pass through the two identical Josephson junctions (A and B). When a magnetic field is applied a magnetic flux Φ goes through the superconducting loop and induces a persistent current J, according to Faraday's Law. The induced

current adds to the measuring current in one junction (I_A), and subtracts in the other (I_B). When the current waves flow through the junctions their phases shift by δ_A and δ_B respectively.

$$\begin{aligned} I_A &= I_0 sin\delta_A \\ I_B &= I_0 sin\delta_B \end{aligned} \tag{2.9}$$

Where I_0 is the maximum allowable current flowing through the junction. Magnetic flux going through a superconducting loop is quantized. Hence there is interference between I after passing the junctions. When a material with magnetic moment is kept in the loop containing a Josephson junction, an *EMF* is induced in the loop, which induces a current with a frequency decided by the Josephson equations. The SQUID detects the change in currents or frequency to deduce the magnetic moment of the sample.

S-VSM (Quantum Design, MPMS) system is used to investigate the magnetic hysteresis loops of NWs at UGC-DAE Consortium for Scientific Research, Kolkata with the help of Dr. D. Das.

2.2.4 Electrical Properties Measurement Techniques

For the measurement of electrical properties of the bulk samples, pellet with diameter of 5 mm and thickness of 1 mm was prepared and sintered at $\sim$ 850°C for 8-10 hr to minimize the oxygen losses and increase grain size. Both sides of the pellet were pasted with silver paste to connect electric wires for the measurements of dielectric and magnetoelectric properties. The sintered density was measured following the Archimedes method and theoretical density was calculated from the lattice parameters values (XRD

refined values) and molecular weight (M) using the formula,

$$\rho = \frac{nM}{NV} \tag{2.10}$$

Where n is the number of molecules per unit cell, N is the Avagadro Number and V is the cell volume. The sintered density of the pure and doped samples was found to be within the range of 92-95 % of the theoretical density. This proves that the pellets used for the measurements were extremely dense with much less air cavities (pores). For the thinfilm samples 100 nm gold layer was sputtered using a shadow mask on both side of the film and for the NWs and NTs samples silver paste was used as top and bottom electrode.

2.2.4.1 Dielectric Properties Measurement Setup

Impedance analyzer or an LCR meter (Inductance (L), Capacitance (C), and Resistance (R)) provides very accurate and thorough component and material evaluation with various test fixtures. It measures impedance (inductance, capacitance, and resistance) at spot frequencies or across a range of frequencies. Advanced model of Impedance analyzer measures the true inductance or capacitance, and also the equivalent series resistance of capacitors and the Q factor of inductive components. The Impedance Analyzer, is interfaced with the computer and the data (capacitance, dissipation factor, inductance and AC conductance) is collected as a function of frequencies. Usually the sample is subjected to an AC voltage source [25, 26]. The analyzer measures the voltage across and the current through the sample. From the ratio of these the analyzer determines the magnitude of the impedance. The phase angle between the voltage and current in combination with the impedance, equivalent capacitance or inductance and resistance of the sample can be calculated and displayed. The analyzer assumes a parallel model for

the CR measurements (as would be encountered in measuring a capacitor with a leaky dielectric) and a series model for a LR measurement (as would be encountered in an inductor coil). So the electrical equivalent of a composite ceramic can be represented by a parallel combination of capacitance (C_p), and a frequency dependent resistance due to short range polarization $R_{ac}(\omega)$ and a dc resistance R_{dc} due to a long range transport of charge carriers. C_p and R_p (the parallel combination of R_{ac} and R_{dc}) are the equivalent capacitance and resistance measured in the experiment for evaluating the dielectric constant and the dielectric loss tangent (tanδ). It may be noted that the resistance R_p in parallel arises due to a combination of both ac and dc conductivity $[\sigma_{ac} + \sigma_{dc}]$ in the sample. tanδ or dissipation factor (D) of a dielectric material at a given frequency ω, is given by,

$$tan\delta = \frac{1}{\omega C_p R_p} \tag{2.11}$$

and the dielectric constant (ε) value can be calculated form the capacitance value using the equation,

$$\varepsilon = \frac{Cd}{A\varepsilon_0} \tag{2.12}$$

where C is the capacitance of the sample in Farad (F), d is the distance between the two electrodes in meters (m), A is the area of the pellet in square meters (m^2) and ε_0 is the free space permittivity (8.85×10^{-12}F/m).

Agilent 4294A Impedance Analyzer was used to measure dielectric constant, AC conductivity, real and imaginary part of impedance (Z' and Z'', respectively) of all the samples. To do the temperature dependent study the samples were placed in an oven in which temperature upto 550°C can be achieved. To observe the magnetoelectric coupling between magnetic and electric ordering parameters in the samples, dielectric properties were measured in the presence of the magnetic field. Here the sample was placed in between the pole pieces of an electromagnet with its surface perpendicular to the field

Figure 2.11: Dielectric properties measurement setup.

direction. The amplitude of the magnetic field was measured by the Hall Probe. In the home-made set-up, maximum 6 kOe magnetic field was achievable. Fig 2.11 shows the home-made set-up for the measurement of the magnetic field and temperature dependent electrical properties of the samples.

2.2.4.2 Ferroelectric Hysteresis Loop or PE Loop Tracer

To establish a material as a multiferroic, it is very important to characterise the ferroelectric properties of that material. A P-E loop of a material is a plot of the charge or polarisation (P) developed in the material on application of an external electric field (E) at a given frequency. In case of an ideal capacitor current leads the voltage by 90 degrees i.e. current and voltage are always out of phase so the P vs E plot will be a straight line (Fig 2.12(a)). But the current and voltage are in phase in case of an ideal resistor so the P-E loop is a circle with the centre at the origin (Fig 2.12(b)). Therefore for a parallel set up with ideal capacitor and resistor the P-E loop shows a leakage nature (Fig 2.12(c)) where the slope of the curve is proportional with the capacitance and the

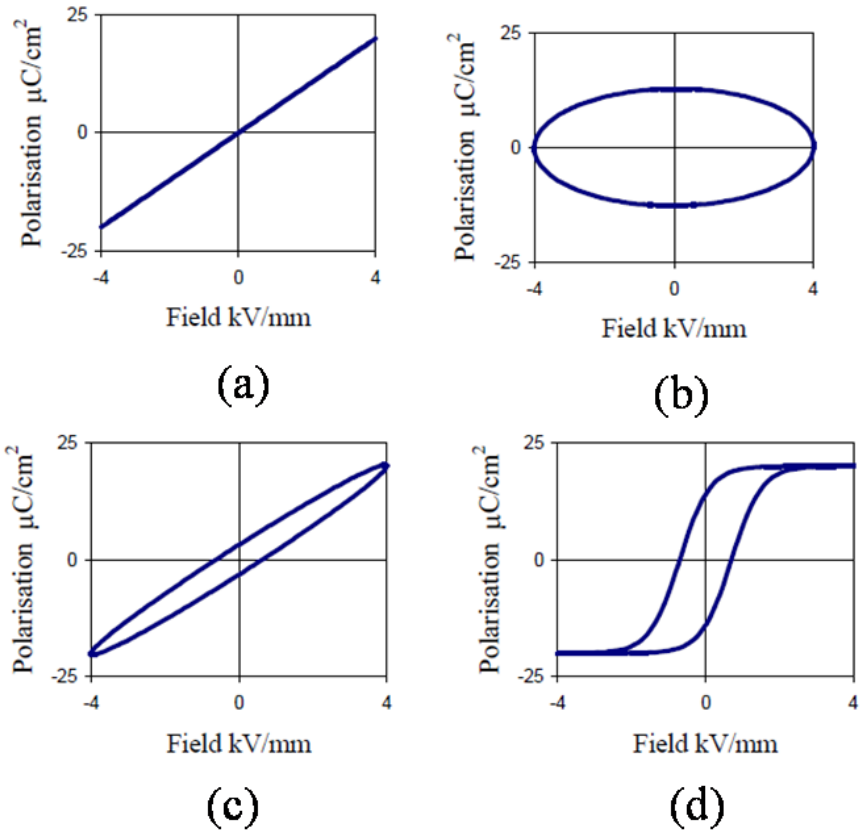

Figure 2.12: (a)Ideal linear capacitor response, (b) Ideal resistor response, (c) Lossy capacitor response and (d) Non-linear ferroelectric response [27].

area is proportional with the loss tangent of the device. Thus if the set up contain a ferroelectric material, we get a PE hysteresis loop (Fig 2.12(d)).

The PE loop measurement method is developed over the years with advances in electronics hardware and software which is based on Sawer-Tower circuit. In 1930, Sawyer and Tower [28] mentioned this technique in their paper which included some seminal measurements on Rochelle salt. Fig 2.13(a) shows the schematic diagram of the circuit. It consist of two capacitor, C_s (s stands for the ferroelectric sample) and C_i in series (i for internal reference) and load resistance, R (series combination of R_1 and R_2). We can select an appropriate value for C_i and R. As the capacitors are connected in

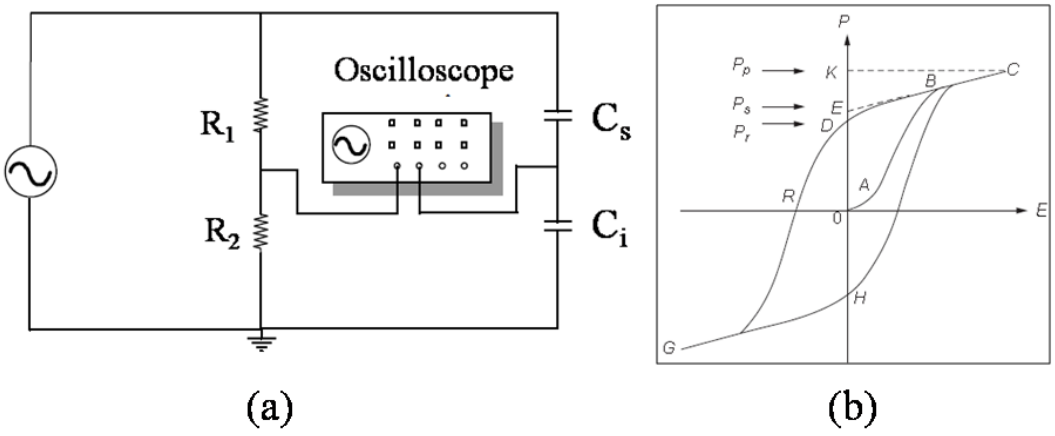

Figure 2.13: (a) Schematic diagram of the Sawer-Tower circuit and (b) Schematic figure of a typical P-E hysteresis loop [27].

series, the charge (Q = CV) on the known (C_i) and unknown capacitors (C_s) will be same. So solving the equations,

$$\begin{aligned} C_i \times C_s &= V_i \times V_s \\ V_T &= V_i + V_s \end{aligned} \tag{2.13}$$

where V_T is the total applied voltage and V_i is measured manually, C_s can be calculated. Finally multiplying C_s with V_s will give the Q_s value. Now Q_s divided by the sample area gives the polarization (P) value of the sample [29].

Fig 2.13(b) shows a typical hysteresis plot. In portion OA of the graph, field induced polarization occurs on the application of a low field. On increasing the field strength, polarization increases non-linearly with the field as the domains start to align in the direction of applied field (portion AB). On further increase in the field strength, the polarization attains a saturation value (portion BC), where maximum domains are aligned in the field direction. On gradually decreasing the field strength, the polarization decreases following the path CBD. The extrapolation of the CB region to zero-field axis at E, gives the region OE, i.e, spontaneous polarization P_s and the region OD represents

the remnant polarization P_r. P_r is always less than P_s, as some of the domains return to their original positions on reducing the field to zero. The electric field required to bring the polarization to zero is called the coercive field (E_c) shown in region OR. E_c depends on frequency, temperature and waveform applied. Ferroelectric hysteresis loops of all the samples are studied by a PE loop tracer (Radiant Technologies, Model no 609B).

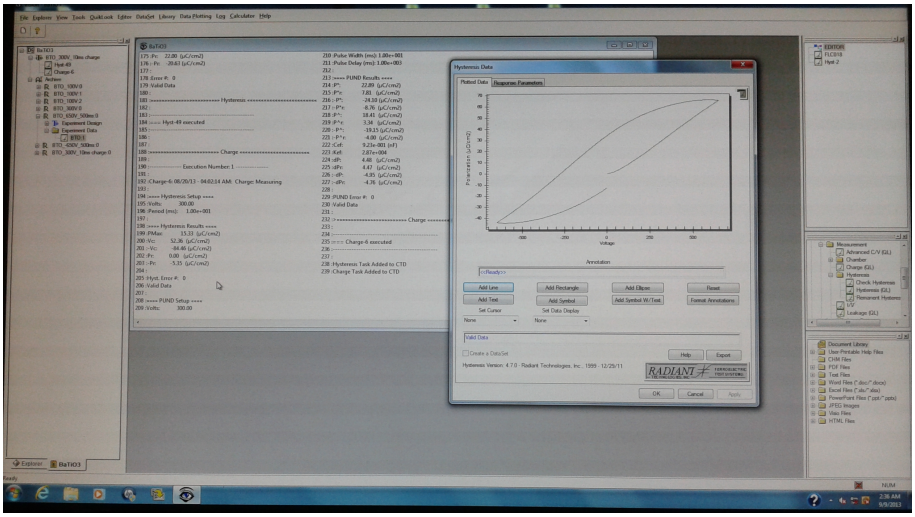

Figure 2.14: PE hysteresis loop of $BaTiO_3$ sample measured at RT.

References

[1] Pulsed Laser Deposition of Thin Films, edited by Douglas B. Chrisey and Graham K. Hubler, John Wiley & Sons, 1994.

[2] H. Masuda and K. Fukuda, Science 268, 1466 (1995).

[3] J. Sarkar, G. G. Khan, and A. Basumallick, Bull. Mater. Sci. 30, 271 (2007).

[4] A. Eftekhari, Nanostructured materials in electrochemistry, Wiley-VCH publishers (2007).

[5] Cullity, B. D., Stock, S. R., Elements of X-ray Diffraction, 3rd Edition, Prentice Hall (2001).

[6] Surface Analysis by Auger and X-ray Photoelectron Spectroscopy, edited by D. Briggs and J.T. Grant. IM Publications and Surface Spectra Limited (2003).

[7] Practical Surface Analysis (second edition) V1, edited by D. Briggs and M. P. Seah. John Wiley and Sons Ltd.(1990).

[8] PNNL EMSL: www.emsl.gov

[9] J.F. Moulder, W.F. Stickle, P.E. Sobol and K.D.Bomben, Handbook of X-ray Photoelectron Spectroscopy. Physical Electronics Inc., Eden Prairie (1995).

[10] Erni, R., Rossell, M. D., Kisielowski, C., Dahmen, U., "Atomic-Resolution Imaging with a Sub-50-pm Electron Probe". Phys. Rev. Lett., 102 (9), 096101(2009).

[11] Groves, T.R., Pfeiffer, H.C., Newman, T.H. and Hohn, F.J., J. Vac. Sci. Technol. B, 6(6), 2028 (1988).

[12] Brundle, C. R., Evans, C. A. Jr., Wilson, S., Encyclopedia of materials characterization, Butterworth-Heinemann publications, 1992.

[13] ProSciTech, Australia.

[14] Fachin formations zentrum (FIZ) Karlsruhe (2007).

[15] D. A. Bonnell, Scanning Probe Microscopy and Spectroscopy, 2nd edition, Wiley-VCH (2000).

[16] Introduction to Magnetic materials, Second Edition edited by B. D. Cullity and C. D. Graham, Wiley (2009)

[17] H. Hopster and H. P. Oepen, Magnetic Microscopy of Nanostructures, Springer (2005).

[18] L. Abelmann, S. Porthun, et al. J. Magn. Magn. Mater., 190, 135147(1998).

[19] Nanoscan AG, Quantum Leap in Hard Disk Technology.

[20] Daniel J. Amit and G. Parisi, J. Phys. C: Solid State Phys., 16, 1385 (1983).

[21] Marcia C. Barbosa, Phys. Rev. B, 46, 3672 (1992).

[22] Michael Aizenman and Jan Wehr, Phys. Rev. Lett., 62, 2503 (1989).

[23] Lake Shore Cryotronics, Inc., USA.

[24] B. D. Josephson, Rev. Mod. Phys. 46 (2) 251254 (1974).

[25] Agilent 4294A Precision Impedance Analyzer, Operation Manual, Accessed in 2012.

[26] J. Wu and J. Wang J. of App. Phys. 105, 124107 (2009).

[27] Y. Xu, Ferroelectric Materials and Their Applications, North-Holland Elsevier Sci. Publ., Amsterdam 1991.

[28] C. B. Sawyer and C. H. Tower, Phys Rev. 35, 269 (1930).

[29] M. Stewart, M. G. Cain and D. A. Hall, Ferroelectric Hysteresis Measurement and Analysis, NPL Report CMMT(A) 152 (1999).

3 Magnetoelectric coupling in undoped and doped $BiFeO_3$ ceramics

3.1 Multiferroic properties of Ba^{2+} doped $BiFeO_3$ ceramics

3.1.1 Background

Multiferroics which possess two ferroic (ferroelectric and magnetic) orderings in single phase are very rare in nature due to its requirement of coexistence of transition metal ions with odd number of d electrons for magnetism with d^0 electronic configuration for ferroelectric property in the same compound. $BiFeO_3$ (BFO) is one of the most interesting members [1] of multiferroic family (such as $BiMnO_3$ and $DyFeO_3$) which shows large magnetoelectric coupling in single phase at room temperature (RT). It has been studied by many groups worldwide due to its importance in fundamental research as well as in commercial applications. Unfortunately, BFO has serious drawbacks, i.e.

low value of magnetoelectric coupling and electric leakage, due to oxygen vacancies or impurities, which restrict the usage of the material for potential application purposes. It has been observed that doping [2, 3, 4, 5] with lone-pair active ions at A-sites and magnetic transition metals at B-sites reduces the leakage current in BFO and enhances the multiferroic properties. Doping changes cycloidal spin structure of BFO to a canted spin structure [6] which can be the reason behind the enhancement in magnetic properties in doped samples. Though Ba-doped BFO shows promising results, few reports are available on this composition [7, 8, 9, 10]. In previous work, RT magnetic, ferroelectric and magnetodielectric properties for $Bi_{1-x}Ba_xFeO_3$ (x=0.15, 0.25, 0.3, 0.35) ceramics [7, 9] and $Bi_{0.75}Ba_{0.25}FeO_3$ thin film [8] were observed. Khomchenko *et. al.* [10] had studied the mechanism of defects formation due to Ba substitution and their influence on the crystal structure and magnetic properties of Ba doped $Bi_{1-x}Ba_xFeO_3$ (x= 0.2, 0.3). In this section, the effect of Ba concentration on the high temperature magnetic and magnetoelectric properties of BFO are investigated in detail.

3.1.2 Results and Discussion

3.1.2.1 Crystal structure of $Bi_{1-x}Ba_xFeO_3$ ceramics

Figure 3.1 shows the XRD pattern of $Bi_{1-x}Ba_xFeO_3$ or Ba_xBFO (x=0.0, 0.1, 0.15, 0.2, 0.25) ceramics. Except the first one, all other samples show single phase perovskite structure which implies that the doping does not lower the stabilization of BFO. Only BFO shows additional low intensity peaks of Bi_2O_3 and $Bi_2Fe_4O_9$ at $2\theta = 27.6°, 33.2°$ and $30.52°$. Inset of Fig 3.1 shows the magnified patterns within $2\theta = 28°$ to $36°$ which reveals a shift in the peak positions towards left with the increase of doping concentration, indicating increment in the lattice parameter. Thus Ba substitution leads to an increase in the unit cell volume since the ionic radius of Ba^{+2} (1.49 Å) is larger

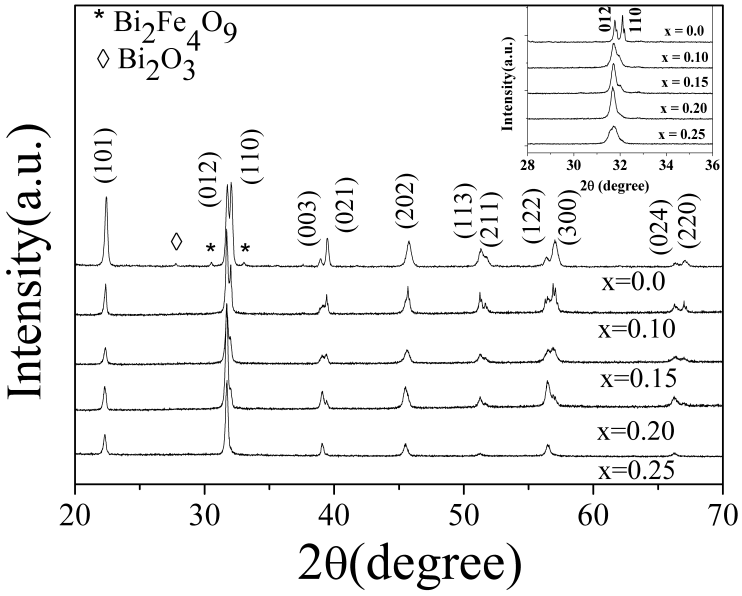

Figure 3.1: XRD patterns for $Bi_{1-x}Ba_xFeO_3$ ($0 \leq x \leq 0.25$) samples.

than that of Bi^{+3} (1.17 Å). Separation between (012) and (110) diffraction peaks (Inset of Fig 3.1) is reduced with Ba substitution which implies that the rhombohedral structure may be distorted to a monoclinic or a tetragonal structure. This change might be important for the ferroelectric properties of the compounds.

3.1.2.2 Thermal properties of $Bi_{1-x}Ba_xFeO_3$ ceramics

Thermal analysis of the samples has been carried out with DTA (200°C to 900°C) and DSC (30°C to 500°C) to study the ferroelectric and magnetic transition temperatures respectively. DTA results are shown in Fig 3.2. For the parent compound, a peak obtained at 831°C is attributed to the ferroelectric transition (T_C) in this compound. The peak is shifted towards higher temperature in the Ba-substituted compounds and reaches 868°C for $Ba_{0.25}$BFO sample exhibiting ferroelectric characteristics over a wide temperature range. This increase in T_C can be due to decrease of pressure with increase in cell volume. In $BaTiO_3$ various transition temperatures shift down on compression

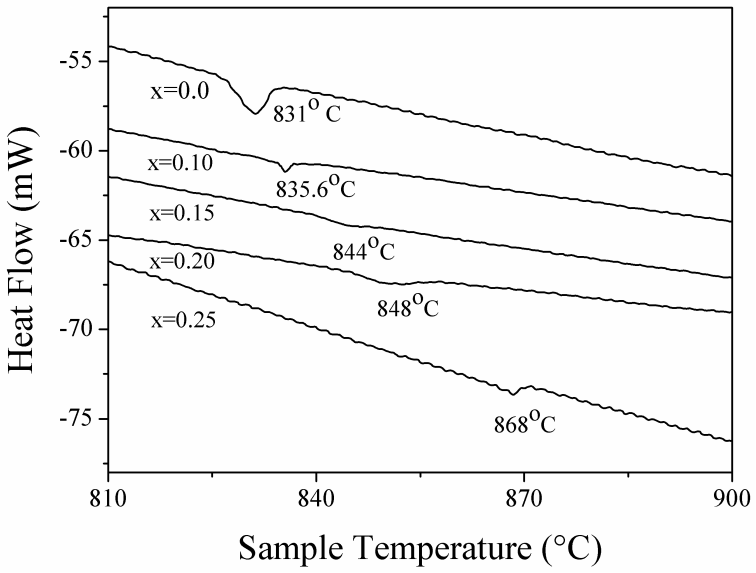

Figure 3.2: DTA patterns for $Bi_{1-x}Ba_xFeO_3(0 \leq x \leq 0.25)$ samples.

[11]. Similarly, lowering of ferroelectric transition temperature is observed when doped with smaller atoms [12]. DSC results for $Bi_{1-x}Ba_xFeO_3$ are shown in Fig 3.3. As can be seen in the figure, the heat flow data shows a kink like anomaly at 369.2°C for undoped BFO (heating curve) and the kink position is almost the same for both heating and cooling curve indicating a second order magnetic phase transition for the compound. Similar to the ferroelectric transition, magnetic transition also shifts towards higher temperature on Ba-doping which is 386.2°C for $Ba_{0.25}$BFO ceramics.

3.1.2.3 Magnetic properties of $Bi_{1-x}Ba_xFeO_3$ ceramics

The magnetic hysteresis loops, as shown in Fig 3.4, illustrate the linear field dependence of magnetization for pure BFO indicating its antiferromagnetic nature. However when Ba is doped replacing Bi, ferromagnetic behavior is observed at RT and the characteristics of the loop depends on doping concentrations. As shown in the inset of Fig 3.4, remanent magnetization and coercivity are maximum in case of x = 0.15 sample. Al-

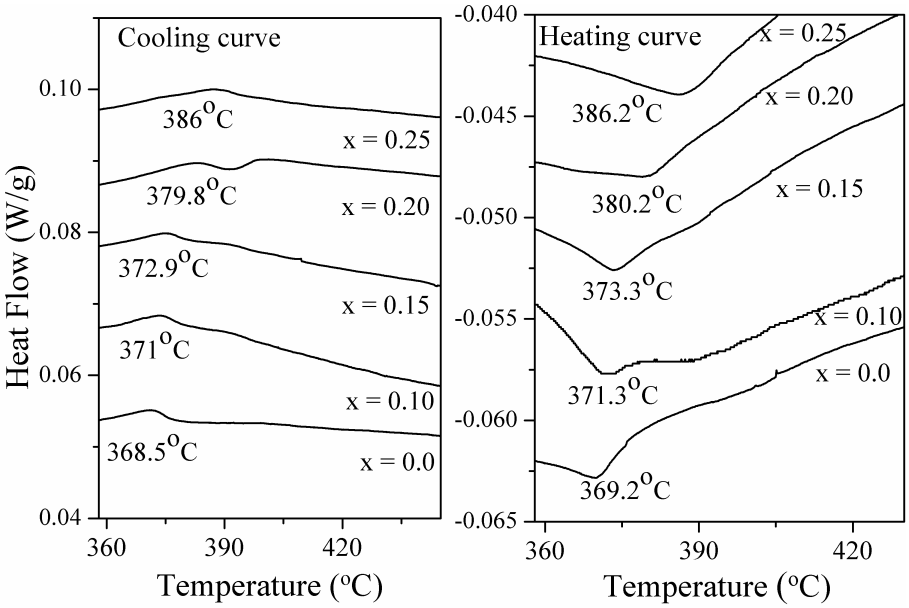

Figure 3.3: DSC patterns for $Bi_{1-x}Ba_xFeO_3(0 \leq x \leq 0.25)$ samples.

though the reason behind the occurrence of ferromagnetism in Ba doped BFO samples is not clearly understood, this can be attributed to the change in interaction between Fe^{+2} and Fe^{+3}, breaking down the balance between the antiparallel sublattice magnetization [13, 14]. Change in canting angle [15] or spiral spin modulation [16] may also be responsible for this phenomenon.

Figure 3.5(a) shows the temperature dependence (30°C to 750°C) of magnetization,

Table 3.1: Comparison of magnetic transition temperature observed in DSC and VSM measurement of $Bi_{1-x}Ba_xFeO_3$ $(0 \leq x \leq 0.25)$ ceramics.

Measurement (°C)	x = 0.0	x = 0.10	x = 0.15	x = 0.20	x = 0.25
DSC data (heating)	369.2	371.3	373.3	380.2	386.2
VSM data (T_{M1})	372	398	400	407	409

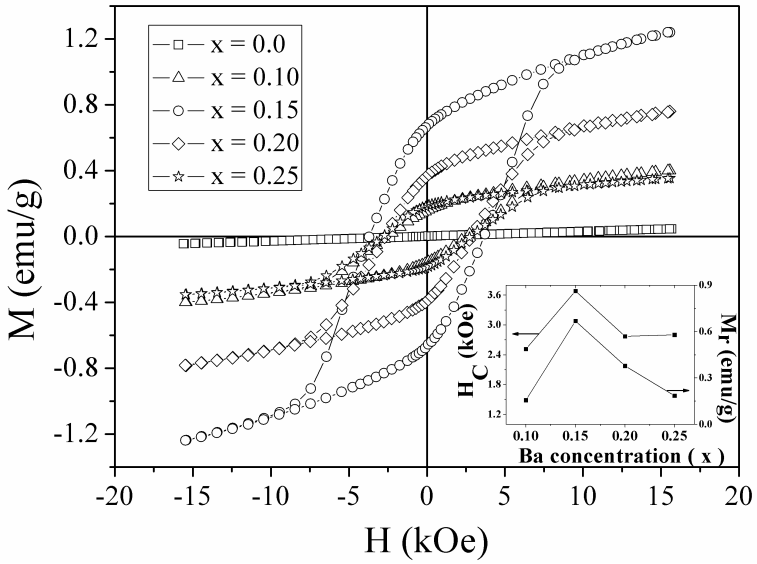

Figure 3.4: Magnetic hysteresis loops of $Bi_{1-x}Ba_xFeO_3(0 \leq x \leq 0.25)$ at room temperature.

M of $Bi_{1-x}Ba_xFeO_3$ in presence of a magnetic field, H=600 Oe. For all Ba doped and undoped BFO sample an antiferromagnetic transition is observed, with a ferromagnetic or ferrimagnetic nature above $\sim$ 373°C (T_{M1}). Another magnetic transition is also observed above $\sim$ 600°C (T_{M2}). The slight increase in transition temperatures with Ba-concentration is shown in the inset of Fig 3.5(a). This is in good agreement with our DSC data (Table 3.1). M increases with Ba concentration till x=0.15 beyond which it decreases. To understand the magnetic behavior, hysteresis loops are measured at temperatures, below T_{M1}, above T_{M2} and within them and they are shown in Fig 3.5(b) and Fig 3.6(a) for pure BFO and $Ba_{0.15}$BFO sample. In between T_{M1} and T_{M2}, pure BFO shows hysteresis loop with very small coercivity, $H_C \sim$ 50 Oe. This magnetic behavior above the Néel temperature can be due to the existence of impurity phase of $Bi_2Fe_4O_9$ as it is paramagnetic at RT [17]. Linear field dependence of M is observed at temperatures higher than T_{M2}. Ba-doped samples show ferromagnetic hysteresis loops at RT and up to T_{M2}, above which they exhibit linear M vs. H behavior resembling

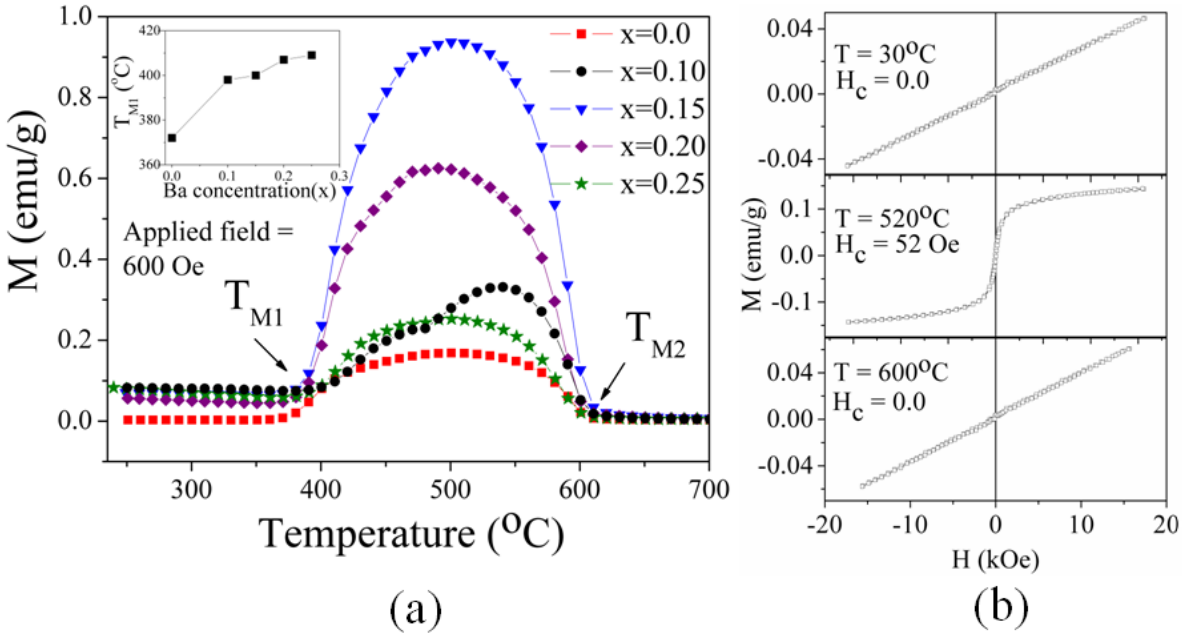

Figure 3.5: (a) Magnetization vs temperature plot of $Bi_{1-x}Ba_xFeO_3 (0 \leq x \leq 0.25)$ at room temperature; (b) Magnetic hysteresis loops of pure $BiFeO_3$ at different temperatures.

paramagnetism as shown in Fig 3.6(a) for x=0.15. A sharp decrease in the coercivity from 3.66 kOe to 14.3 Oe is observed with the increase of temperature from 30°C to 520°C in case $Ba_{0.15}$BFO sample.

To confirm the magnetic state of the samples at different temperature, Arrott's plots (M^3 vs H) are plotted (Fig 3.6(b)) for the samples with x=0 and 0.15. Parent compound shows positive intercept (Fig 3.6(b)) on the y-axis indicating spontaneous magnetization in between T_{M1} and T_{M2} only. On the other hand, $Ba_{0.15}$BFO shows spontaneous magnetization up to T_{M2} (Fig 3.6(b)).

3.1.2.4 Ferroelectric properties of $Bi_{1-x}Ba_xFeO_3$ ceramics

It is very difficult to get good ferroelectric properties in BFO ceramics due to the presence of oxygen vacancies. However, Ba substitution makes BFO more insulating and

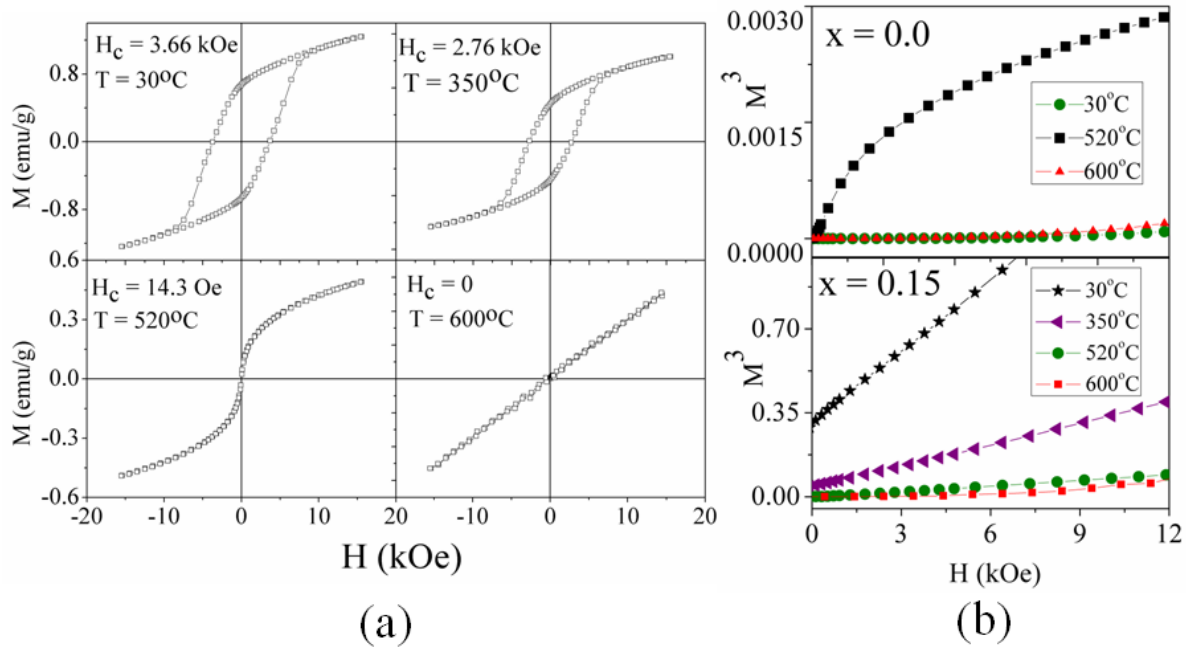

Figure 3.6: (a) Magnetic hysteresis loops of $Bi_{0.85}Ba_{0.15}FeO_3$ at different temperatures; (b) M^3 vs H plots of $BiFeO_3$ (top) and $Bi_{0.85}Ba_{0.15}FeO_3$ (below) at different temperatures.

better ferroelectric properties are observed. This can occur if the samples have a stoichiometry of $Bi_{1-x}Ba_xFeO_{3-\delta}$ instead of having mix valence of Fe ions to maintain the charge neutrality. This can also be explained by the distortion of oxygen octahedral by relative displacement of the equatorial and apical oxygens in Ba doped samples as observed in A site ion-substituted $Bi_4Ti_3FeO_{12}$ [18]. Enhanced ferroelectricity observed in $Bi_{4-x}La_xTi_3O_{12}$ is due to rotation of TiO_6 octahedra in the a-b plane accompanied with a shift of the octahedron along the c axis. Room temperature, polarization (P) vs electric field (E) loops of $Bi_{1-x}Ba_xFeO_3$ ($0.1 \leq x \leq 0.25$) samples are shown in Fig 3.7 at the frequency of 50 Hz. $Ba_{0.1}$BFO and $Ba_{0.15}$BFO exhibits an unsaturated hysteresis loop while $Ba_{0.2}$BFO shows saturated P-E loop. Though $Ba_{0.25}$BFO is showing higher polarization compared to others, the observed roundish hysteresis loop is due to a large leakage current which can overshadow the real contribution from reorientation of electri-

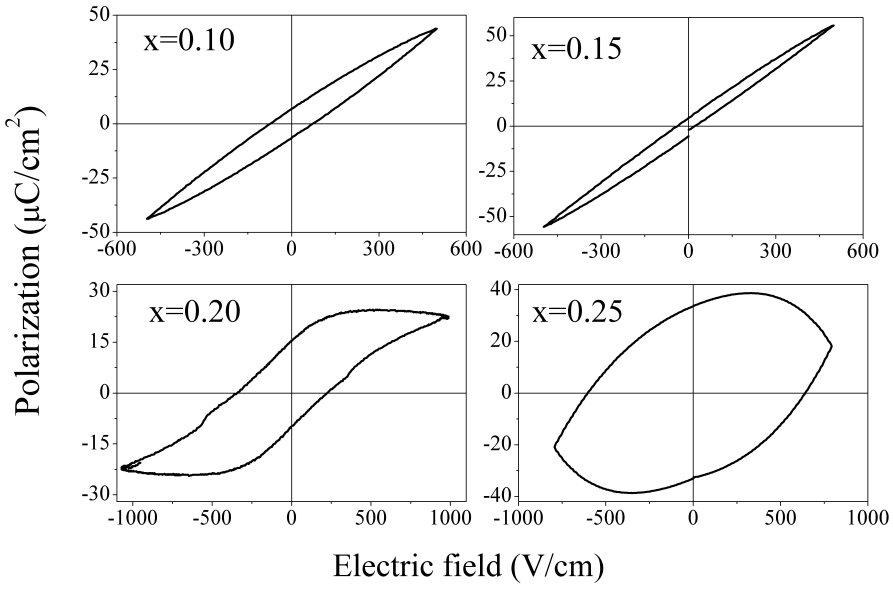

Figure 3.7: Ferroelectric hysteresis loop of $Bi_{1-x}Ba_xFeO_3(0.1 \leq x \leq 0.25)$ ceramics at f = 50 Hz.

cal dipoles [19]. From Fig 3.7 it can be predicted that dielectric loss or leakage current is negligible in Ba = 0.1, 0.15 and 0.2 doped samples.

Electrical switching causes the trapping of electronic charge at the domain wall. Fatigue endurance of the samples is also an important factor for practical applications. Fatigue occurs in BFO mainly because of the change in the positions of oxygen vacancies. Doping of higher radius Ba^{+2} reduces movable charge density due to which fatigue resistance changes with appropriate doping concentration. Fatigue characteristics of all the samples are carried out at an applied field ± 6 kV cm^{-1} and frequency 50 Hz. Fig 3.8 shows that remanent polarization P_r value remains almost the same up to 2×10^5 read and/or write switching cycles for samples x=0.1 to 0.2. P-E loop shows the same nature before and after the fatigue measurement. Though $Ba_{0.25}$BFO shows higher P_r value initially than the other Ba doped samples, fatigue resistance of $Ba_{0.25}$BFO is very much less than the rest of Ba doped samples. P_r value of $Ba_{0.25}$BFO decreases continuously from $\sim 24.3\,\mu C/cm^2$ to a lower value with the switching cycles. Compared

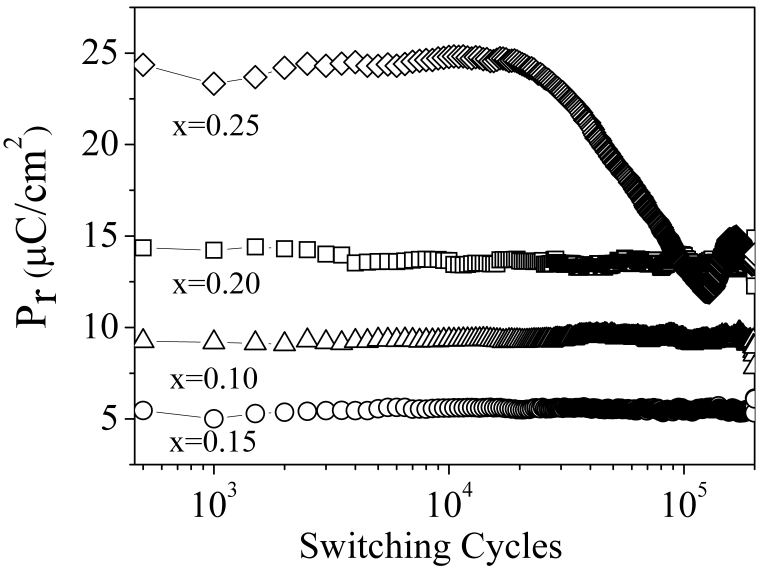

Figure 3.8: Fatigue traits of $Bi_{1-x}Ba_xFeO_3(0.1 \leq x \leq 0.25)$ ceramics at $E = \pm 6$ kV cm^{-1} and $f = 50$ Hz.

to others, $Ba_{0.2}$BFO sample shows maximum fatigue resistance with P_r value about $\sim 14.35\,\mu C/cm^2$ throughout the measurement cycles.

3.1.2.5 Dielectric and Magnetodielectric effect

Fig 3.9 shows the variation of dielectric constant (ε) of the samples measured from 50 to 1000 Hz at RT. ε changes noticeably with doping concentration. $Ba_{0.2}$BFO shows maximum value of ε at RT. The trend observed here is closely similar to that of ferroelectric measurements. Inset of Fig 3.9 shows the variation of ε with Ba doping concentration. Magnetoelectric coupling of $Ba_{0.2}$BFO sample (which shows maximum fatigue resistance) is clearly shown in Fig 3.10. ε of the sample increases with the applied magnetic field. Inset (a) of Fig 3.10 shows a field dependence of the magnetodielectric (MD) effect [8, 20], expressed by $[\varepsilon_r(H)\text{-}\varepsilon_r(0)]/\varepsilon_r(0)$ at frequency (f) 500 Hz. The value of positive MD effect in case of $Ba_{0.2}$BFO sample is higher than the MD effect reported in Nd doped

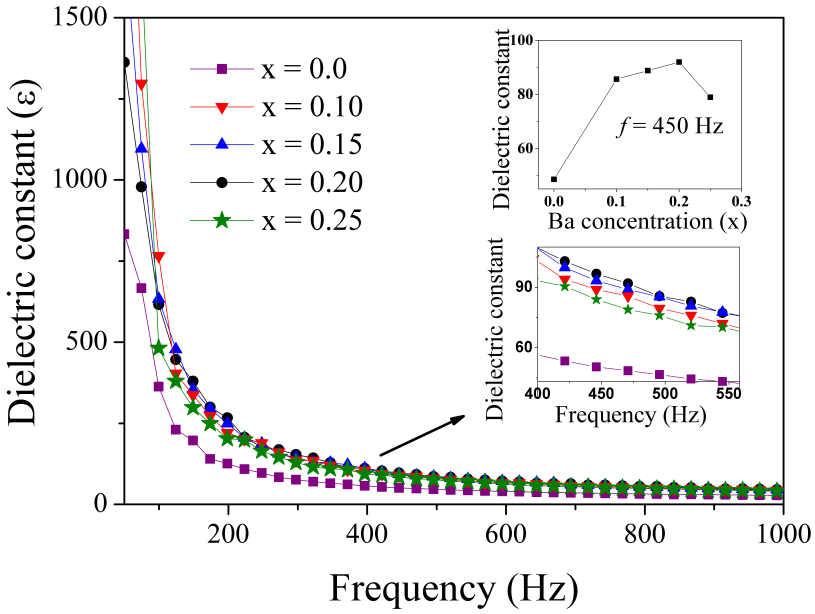

Figure 3.9: Dielectric constant vs frequency (50 Hz-1 kHz) of $Bi_{1-x}Ba_xFeO_3(0 \leq x \leq 0.25)$ ceramics at room temperature.

BFO ceramics [21]. On the other hand, at higher magnetic field some multiferroics, such as $BiMnO_3$, show negative MD effect i.e decrease in ε value with the increase in applied field [22]. This increase in ε with field might be due to magnetoelectric effect or leakage current or magnetostriction. But the resistivity of the material increases on Ba doping. Therefore, we can eliminate the leakage current effect. To the best of our knowledge, effect of magnetostriction on ε value of BFO is not checked yet. The percentage change of ε in $BiMnO_3$ due to magnetostriction was reported to be less than 1% [22]. Therefore, magnetoelectric effect is dominant factor for the change in ε with magnetic field. In multiferroics, electric and magnetic domains coexist. The application of magnetic field gives rise to strain and hence develops stress. Strain induced stress on the ferroelectric generates the electric field [23]. This field could orient the ferroelectric domains, leading to an increase in ferroelectric properties. So ε value of the material increases when magnetic field is applied. Temperature dependence of ε of the sample $Ba_{0.2}$BFO from RT

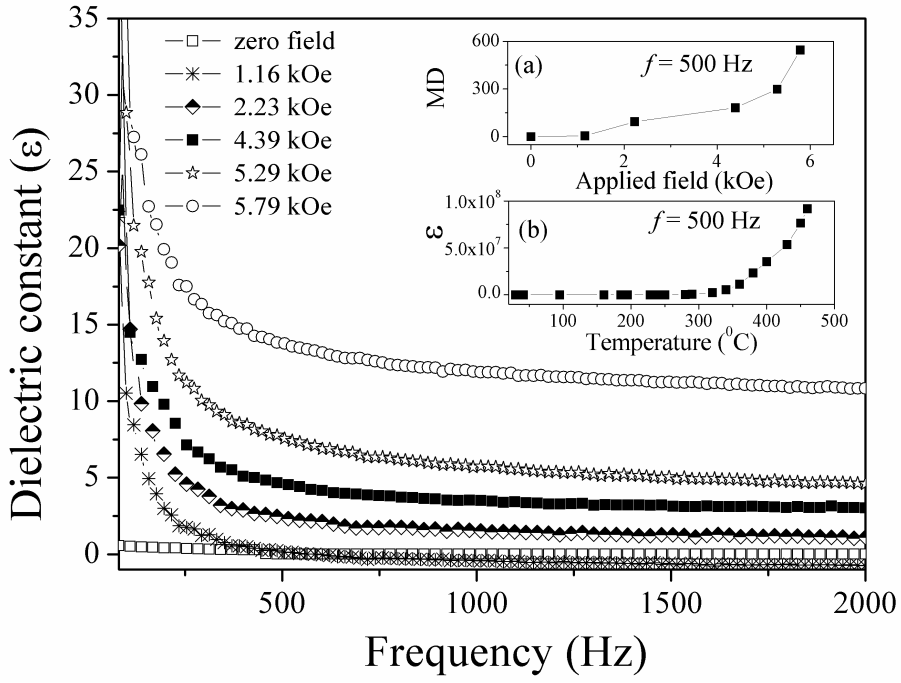

Figure 3.10: Dielectric constant (ε) vs frequency (100 Hz-2 kHz) of $Bi_{0.8}Ba_{0.2}FeO_3$ sample at different fields. Inset (a): MD vs applied field and Inset (b) ε vs temperature.

to 460°C is shown in the inset (b) of Fig 3.10. Further increase of temperature was not possible due to the limitation of sample holder. It is observed that at zero field ε of the sample increases sharply above 360°C. This sharp increase can be considered due to the magnetic phase transition around this temperature or it can be said that the magnetic ordering suppresses the dielectric constant.

3.2 Multiferroic properties of Ba^{+2} and Gd^{+3} co-doped $BiFeO_3$ ceramics

3.2.1 Background

Co-substitution of multi-elements in the A and B sites also enhances multiferroic properties of $BiFeO_3$ (BFO). It is reported that co-doping reduces the leakage current problem due to reduction in oxygen vacancy and better charge compensation in the samples [5, 24, 25].

A large electric remanent polarization ($P_r > 70\,\mu C/cm^2$) is reported in $Bi_{1-x}Gd_xFeO_3$ films deposited on $Pt/Ti/SiO_2/Si$ substrates [26]. But $Bi_{1-x}R_xFeO_3$(R = $GdMnO_3$, Gd) sample shows very weak ferromagnetic (FM) order at room temperature (RT) [27, 28]. Previous reports show that Ba doping in Bi site enhances magnetoelectric properties and shows ferromagnetism at RT [7, 8, 9, 10, 29]. But, according to the best of our knowledge, characteristics of Ba and Gd co-doped BFO are not known yet. In this present work, we have doped Ba replacing Bi and Gd in place of Fe. Gd^{+3} (0.93 Å) is used to substitute Fe^{+3} (0.63 Å) because of its higher magnetic moment compared to Fe and higher radius which will create more distortion which results in an enhancement in the electrical polarization. So it is expected that Ba and Gd co-doped samples will provide both enhanced properties as well as good ME coupling.

3.2.2 Results and Discussion

3.2.2.1 XRD and XPS studies of $Bi_{1-x}Ba_xFe_{1-y}Gd_yO_3$ compounds

Figure 3.11 shows the XRD pattern of undoped, single ion doped and co-doped BFO samples ($Bi_{1-x}Ba_xFe_{1-y}Gd_yO_3$ compounds henceforth written as Ba_xGd_yBFO where x

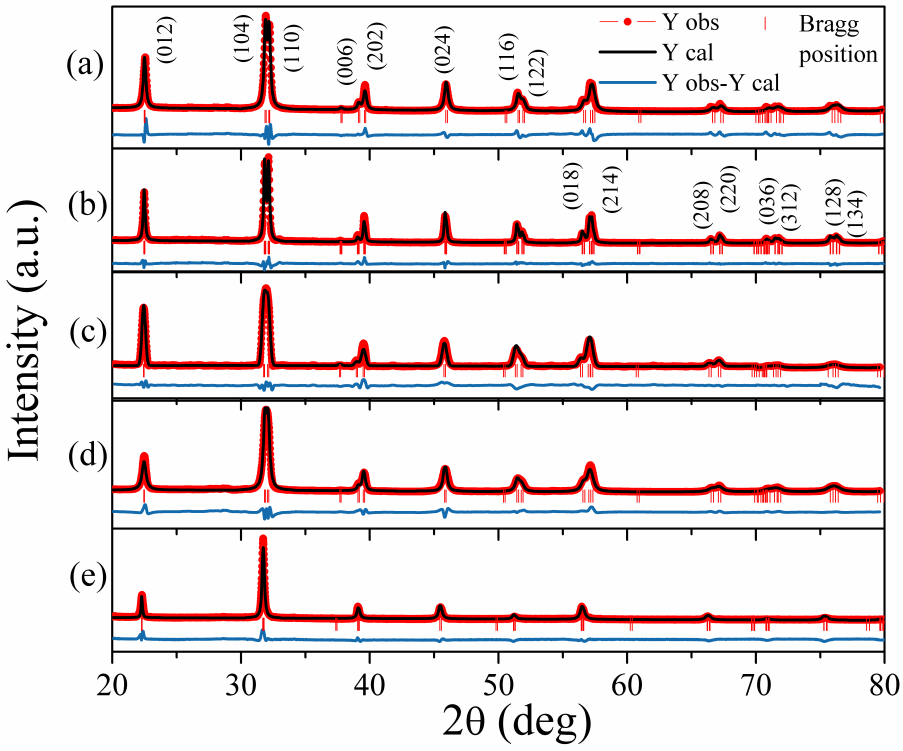

Figure 3.11: XRD patterns for $Bi_{1-x}Ba_xFe_{1-y}Gd_yO_3(0 \leq x, y \leq 0.1)$samples.

and y are Ba and Gd concentration, respectively). $Gd_{0.05}$BFO and $Ba_{0.05}Gd_{0.05}$BFO possess similar structure with BFO. While with the increase in doping concentration XRD pattern shows that the doubly split peaks of BFO at $2\theta \sim 32°$, $39°$, $51°$ and $56°$ merge into a single broadened peak. This behavior indicates the possibility of higher structural distortion due to doping. Merging of peaks upon ion doping was reported earlier as an indication of rhombohedral to orthorhombic phase transition [30, 31, 32]. The Rietveld refinement was carried out for rhombohedral, triclinic, monoclinic and orthorhombic structures. From the refined parameters, the value of χ^2 in rhombohedral (=1.96) and orthorhombic (=2.11) structures was found to be lesser than that in monoclinic and triclinic structures. But we have not observed any (111) peak near $2\theta = 27°$ which has been assigned as the evidence of the rhombohedral to orthorhombic structure change [33]. Hence all the samples crystallize into the rhombohedrally distorted per-

Table 3.2: Refined structural parameters for $Bi_{1-x}Ba_xFe_{1-y}Gd_yO_3(0 \leq x, y \leq 0.1)$ ceramics. (Error in 10^{-4} order in refined parameters)

Sample	lattice parameters	atoms		Positions x	y	z	Bond	Len -gth Å	Fe-O(1) / Fe-O(2)	angle Fe-O -Fe
BFO	$a =$	Bi/Ba	6a	0	0	0	Bi-O	2.38	1.12	152.44
	5.5617 ± 2	Fe/Gd	6a	0	0	0.2525 ± 2	Fe-O(1)	2.15		
	$c =$	O	18b	0.4194 ± 2	0.0008 ± 1	0.9571 ± 2	Fe-O(2)	1.91		
	13.8009 ± 1									
$Gd_{0.05}$	$a =$	Bi/Ba	6a	0	0	0	Bi-O	2.11	1.19	142.41
BFO	5.5756 ± 2	Fe/Gd	6a	0	0	0.2194 ± 2	Fe-O(1)	2.27		
	$c =$	O	18b	0.4239 ± 1	0.0226 ± 2	0.9345 ± 3	Fe-O(2)	1.90		
	13.8585 ± 1									
$Ba_{0.05}$	$a =$	Bi/Ba	6a	0	0	0	Bi-O	2.21	1.21	154.82
$Gd_{0.05}$	5.5679 ± 5	Fe/Gd	6a	0	0	0.2247 ± 4	Fe-O(1)	2.27		
BFO	$c =$	O	18b	0.4611 ± 2	0.0082 ± 1	0.9442 ± 5	Fe-O(2)	1.81		
	13.8273 ± 1									
$Ba_{0.05}$	$a =$	Bi/Ba	6a	0	0	0	Bi-O	2.66	1.39	166.20
$Gd_{0.1}$	5.6377 ± 4	Fe/Gd	6a	0	0	0.2551 ± 2	Fe-O(1)	2.34		
BFO	$c =$	O	18b	0.4733 ± 3	-0.0294 ± 5	0.9777 ± 4	Fe-O(2)	1.67		
	13.8225 ± 1									
$Ba_{0.1}$	$a =$	Bi/Ba	6a	0	0	0	Bi-O	2.29	1.22	163.10
$Gd_{0.05}$	5.5753 ± 2	Fe/Gd	6a	0	0	0.2277 ± 1	Fe-O(1)	2.34		
BFO	$c =$	O	18b	0.4935 ± 2	0.0003 ± 2	0.9521 ± 1	Fe-O(2)	1.79		
	13.8126 ± 3									

ovskite structure with the space group R3c at RT accompanied by significant structural distortion. Table 3.2 shows the refined parameters.

To further measure the oxidation states of the elements and change in the oxygen vacancy concentration with doping in the doped samples, XPS measurements were performed of undoped BFO, $Ba_{0.1}Gd_{0.05}$BFO and $Ba_{0.05}Gd_{0.1}$BFO ceramics. Fig 3.12(a) displays a doublet located at 157.9 eV and 163.2 eV, corresponding to the core lines of Bi $4f_{7/2}$ and $4f_{5/2}$ of Bi^{+3}, respectively, remain unchanged with doping in all the samples. The Fe valence states of the samples are shown in Fig 3.12(b). There is no difference in the peak positions for all the samples. The peaks at binding energy 710.3 eV and 723.9 eV represents Fe $2p_{3/2}$ and $2p_{1/2}$ peaks, respectively of Fe^{+3} which arises from spin orbit interaction. No distinct peak of Fe^{+2} is observed at 709.5 eV. The satellite peak for Fe $2p_{3/2}$ at a difference of 8 eV furthermore confirms that only Fe^{+3} is present

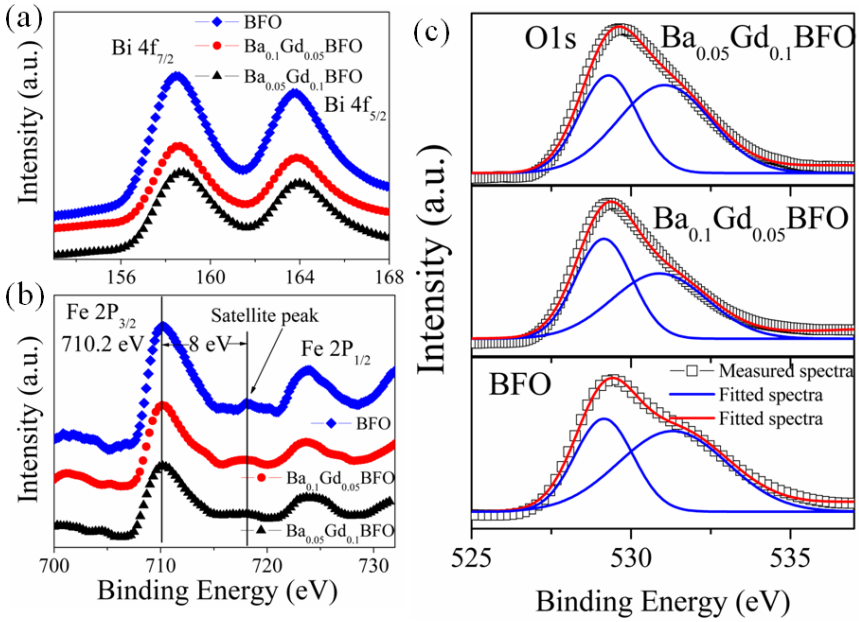

Figure 3.12: XPS spectra of the (a) Bi, (b) Fe and (c) O element of BFO, $Ba_{0.1}Gd_{0.05}BFO$ and $Ba_{0.05}Gd_{0.1}BFO$ samples.

in the samples. Fig 3.12(c) shows O 1s spectra of the samples which can be fitted by symmetric Gaussian curve with peak positions 529.2 eV and 531.4 eV. The lower binding energy peak corresponds to the O 1s core spectrum of BFO phase [34] while higher binding energy peak attributes to the oxygen vacancy [35] in the samples. Comparing the area ratio of the two peaks (lower binding energy/ higher binding energy) in samples, it is observed that the area ratio is higher in co-doped sample as compared with BFO, indicating the decrease of oxygen vacancy concentration in the co-doped samples [36]. Oxygen vacancy is minimum in $Ba_{0.1}Gd_{0.05}BFO$.

3.2.2.2 Magnetic properties of $Bi_{1-x}Ba_xFe_{1-y}Gd_yO_3$ compounds

The magnetization hysteresis (M-H) loops of all samples are shown in Fig 3.13(a) and (b), which clearly indicates the enhancement in magnetization with doping at 80 K and

300 K. Though $Gd_{0.05}$BFO and $Ba_{0.05}Gd_{0.05}$BFO show weak ferromagnetic behaviour, magnetization value at maximum applied field is more in the first one with the same concentration of Gd. Interestingly, ferromagnetic response is enhanced with further increase in Ba or Gd doping concentration (i.e. in $Ba_{0.05}Gd_{0.1}$BFO and in $Ba_{0.1}Gd_{0.05}$BFO). Gd rich, $Ba_{0.05}Gd_{0.1}$BFO shows enhanced magnetic property among all the doped samples with remanent magnetization $\sim$ 0.07 emu/gm at 300 K and maximum magnetization value $\sim$ 0.82 eum/gm at 80 K at an applied field 16 kOe. As reported previously, Eu and Gd doped BFO show lesser magnetization value [16, 33, 37]. Pradhan *et al.* anticipated that the ferromagnetism in Bi rich Fe deficient Gd doped BFO ceramics [16] might be induced from the defects created by excess Bi in the interstitial region of BFO lattice. But defect driven ferromagnetism is ruled out in our case as Bi concentration is reduced due to Ba substitution. Origin of ferromagnetic states in nanostructured BFO is the breakdown of the cycloid spin structure in the samples [15, 28, 34]. But this size effect does not play any role in our case as our samples are bulk in size.

Now the possible reason behind the enhancement in magnetization in our case might be the followings: (a) Although, valance state of Fe in BFO should be Fe^{+3} but charge compensation required due to Ba^{+2} doping in the position of Bi^{+3} might give rise to formation of Fe^{+4} or oxygen vacancies. Incorporation of Fe^{+4} in the compound changes the magnetic spin structure from antiferromagnetic to ferrimagnetic due to difference in magnetic moment between Fe^{+3} and Fe^{+4}. But magnetization value here in co-doped sample is less compared to only Ba doped BFO ceramics [7, 29]. This observation indicates that mixed valance state of Fe is reduced due to co-doping in our sample. But further experimental evidence is needed to prove this fact. (b) Khomchenko *et al.* reported [27] that in $Bi_{1-x}Gd_xFeO_3$ enhanced magnetism does not occur from magnetically active Gd^{+3} as the contributions of Fe and Gd averaged over the cycloid period of the spatially modulated structure in $Bi_{1-x}Gd_xFeO_3$ would be zero. This argument could be

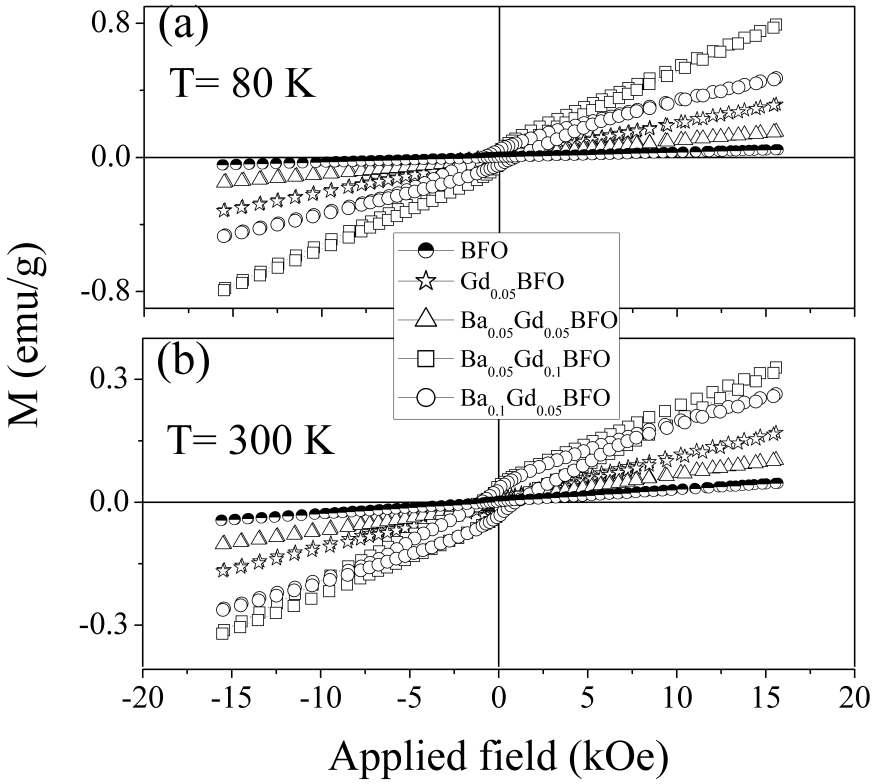

Figure 3.13: Magnetic hysteresis loops of $Bi_{1-x}Ba_xFe_{1-y}Gd_yO_3(0 \leq x, y \leq 0.1)$ at (a) 80 K and (b) 300 K.

true in our case also. (c) Dzyaloshinksii-Moriya (DM) interaction induces weak ferromagnetism and magnetoelectric effects in incommensurate (IC) multiferroic perovskites, such as $RMnO_3$ (R= Gd,Tb,Dy) [38]. In case of cuprates, DM interaction depends linearly on the tilt of the oxygen octahedra and on the spin orbit of the Cu^{+2} ions [39]. So it might happen that as distortion occurs in the lattice structure of the samples due to doping, DM interaction is one of the reasons of weak ferromagnetism in the materials. Weak ferromagnetism may also arise because of the magnetoelectric interactions due to internal effective electric field as suggested by Kadomtseva *et al.* [40]. (d) In the FeO_6 octahedra the iron atom is displaced with respect to the centre of the octahedron. So in case of undoped BFO, it has three oxygen atoms located at a long distance of 2.15 Å

(Fe-O(1)) and other three oxygen atoms located at a short distance of 1.91 Å (Fe-O(2)) from Fe. Substitution of higher radius atoms, Ba^{+2} (1.49 Å) and Gd^{+3} (0.93 Å) replacing Bi^{+3} (1.17 Å) and Fe^{+3} (0.63 Å) respectively, distort the lattice structure which changes the ratio between Fe-O(1) and Fe-O(2) bond, which results in a change in the Fe-O-Fe bond angle. (Fe-O(1)) / (Fe-O(2)) ratio is maximum in case of $Ba_{0.05}Gd_{0.1}BFO$. Hence, the major reason of ferromagnetic ordering in Ba and Gd co-doped samples is the release of potential magnetization locked in cycloidal spin structure.

3.2.2.3 Electrical properties of $Bi_{1-x}Ba_xFe_{1-y}Gd_yO_3$ compounds

P vs E loop of all four samples are shown in Fig 3.14 at a frequency of 50 Hz and a maximum field ±50 kV cm^{-1}. Doped samples show well saturated P-E loop while BFO does not show any ferroelectric switching. Roundish P-E loop of $Gd_{0.05}BFO$ sample occurs due to the high leakage current in a high electric field region. As co-doped samples are more insulating compared to others (Inset of Fig 3.14), charge defect concentration is noticeably less in them. $Ba_{0.1}Gd_{0.05}BFO$ shows a higher resistivity ($\sim 1.5 \times 10^7 \Omega$-cm at f=1 kHz) at an applied field of 5.5 kOe and maximum remanent polarization ($P_r \sim 8.82\,\mu C/cm^2$) compared to that of the other doped samples. But $Ba_{0.05}Gd_{0.1}BFO$ shows more leakage free nature with $P_r \sim 7.08\,\mu C/cm^2$. Table 3.2 shows that Gd and Ba co-doping distorted the Fe-O octahedra which might leads to an enhancement in polarization value. It is reported that straightening of Fe-O-Fe angle increases orbital overlap between O 2p and the Fe 3d levels [41]. Though Fe-O-Fe angle is minimum in $Gd_{0.05}BFO$ sample, it shows leakage behaviour. Therefore better ferroelectric property in the co-doped samples occurs due to the reduction in oxygen vacancy.

Frequency dependence of the dielectric constant (ε) of the samples is measured at RT (Fig 3.15). The ε value is $\sim$ 196, 48, 530, 459 and 1536 at 1 kHz for the samples with

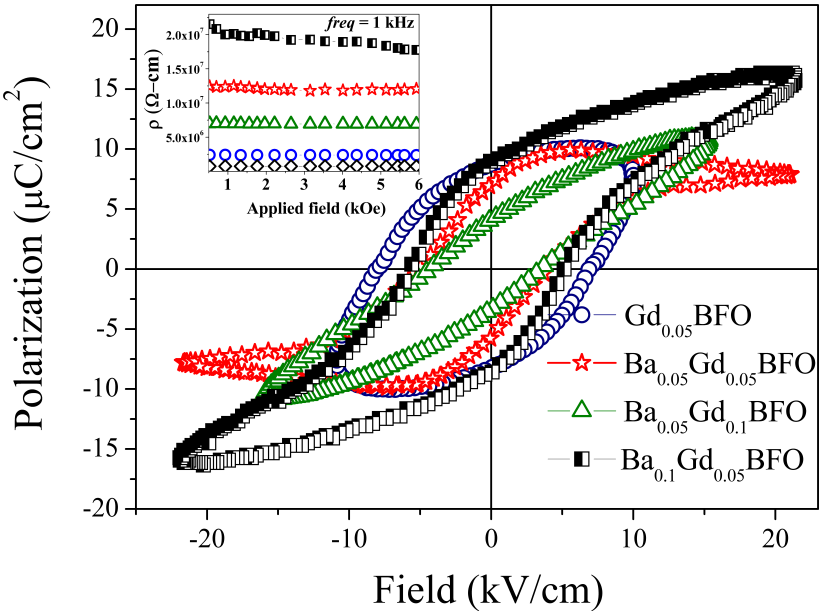

Figure 3.14: Ferroelectric hysteresis loop of $Bi_{1-x}Ba_xFe_{1-y}Gd_yO_3(0 \leq x, y \leq 0.1)$ ceramics at f = 50 Hz. Inset shows resistivity (ρ) vs applied magnetic field plot at frequency 1 kHz.

compositions BFO, $Gd_{0.05}$BFO, $Ba_{0.05}Gd_{0.05}$BFO, $Ba_{0.05}Gd_{0.1}$BFO and $Ba_{0.1}Gd_{0.05}$BFO respectively. High ε value in the co-doped samples indicates a lower charge defect in the samples. Though, BFO and $Gd_{0.05}$BFO shows only slight dispersion with frequency, co-doped samples show significant frequency dispersion behaviour similar to the earlier reports on BFO samples [2, 42]. Low frequency dispersion of BFO is reported due to finite conductivity which arises from oxygen vacancies in BFO ceramics [43, 44]. Four types of polarization, (a) Electronic, (b) Atomic and Ionic, (c) Dipolar and (d) Interfacial polarization, contribute to the total polarization. Dipolar polarization contributes in the subinfrared frequency range ($10^3 - 10^6$ Hz) [33]. It is impossible for dipolar polarization to follow the electric field in the microwave region. Whereas interfacial polarization contributes only in the lower frequency range ($\sim 10^3$ Hz). Therefore, at higher frequency ε is smaller as all polarizations do not contribute at high frequencies.

Obstruction of charge carriers at the grain boundaries or at defect sites develops the

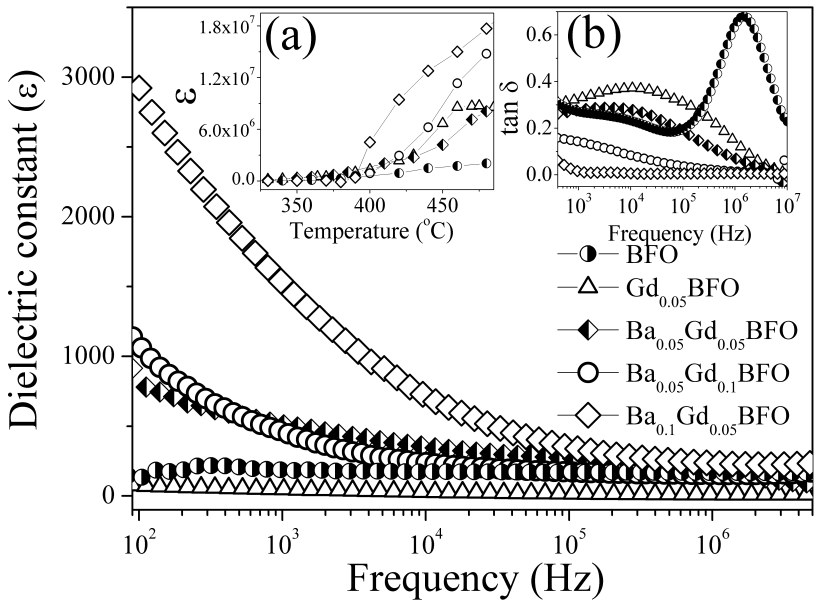

Figure 3.15: Dielectric constant (ε) vs frequency of $Bi_{1-x}Ba_xFe_{1-y}Gd_yO_3(0 \leq x, y \leq 0.1)$ ceramics at room temperature. Inset (a) shows the ε vs temperature plot at frequency 1 kHz and (b) shows RT Dielectric loss (tan δ) vs frequency plot.

localized polarization in polycrystalline samples [45]. RT variation of ε with frequency is well fitted with the Cole-Cole equation given by,

$$\varepsilon(\omega) = \varepsilon_\infty + \frac{\varepsilon_s - \varepsilon_\infty}{(1 + i\omega t)^{1-\alpha}} \tag{3.1}$$

where, ε_∞ is the permittivity at the high frequency limit, ε_s is the static, low frequency permittivity, τ is the characteristic dielectric relaxation time and ω is the angular frequency. The exponent parameter α can take a value between 0 and 1. τ and (1-α) values of all the samples obtained from the best fitted experimental and theoretical results (Table 3.3) indicate that the dielectric relaxation time increases with doping.

Table 3.3: Dielectric relaxation time (τ) and $(1-\alpha)$ values for $Bi_{1-x}Ba_xFe_{1-y}Gd_yO_3$ $(0 \leq x, y \leq 0.1)$

Sample	ε_∞	ε_s	$\tau(s)$	$1-\alpha$
BFO	1.65	2	$(3.7 \pm 0.2) \times 10^{-4}$	(0.4 ± 0.008)
$Gd_{0.05}$BFO	1	0.08	$(0.9 \pm 0.01) \times 10^{-2}$	(0.27 ± 0.001)
$Ba_{0.05}Gd_{0.05}$BFO	2.5	10.5	$(1.5 \pm 0.2) \times 10^{-2}$	(0.31 ± 0.005)
$Ba_{0.05}Gd_{0.1}$BFO	1.55	24.5	$(4.4 \pm 0.8) \times 10^{-2}$	(0.44 ± 0.003)
$Ba_{0.1}Gd_{0.05}$BFO	2.1	42	$(1.2 \pm 0.2) \times 10^{-2}$	(0.37 ± 0.005)

3.2.2.4 Magnetoelectric coupling of $Bi_{1-x}Ba_xFe_{1-y}Gd_yO_3$ compounds

Establishing a material as a good multiferroic requires the presence of magnetoelectric (ME) coupling between magnetic and electric dipoles in the material. ME coupling of the material can be measured by observing the change in polarization or magnetization value by the application of external magnetic or electric field respectively. Inset (a) of Fig 3.15 shows the ε vs temperature plots of all the samples at a frequency 1 kHz. It can be seen clearly that at low temperature ($< 350°C$), ε value of all the samples is invariant with temperature. But around 385°C, which is very close to the magnetic transition temperature (370°C) of BFO, ε of all the samples increases sharply. Since magnetic and electric orderings are coupled in these materials, change in magnetic ordering clearly affects the ε value. $Ba_{0.1}Gd_{0.05}$BFO shows maximum increment of ε than the other doped samples. Inset (b) of Fig 3.15 shows the dielectric loss ($\tan\delta$) vs frequency plots of all the samples. Dielectric loss behaviour of undoped BFO at higher frequency ($\sim 10^6$ Hz) range indicates the Maxwell-Wagner space charge effect [46, 47]. This dielectric

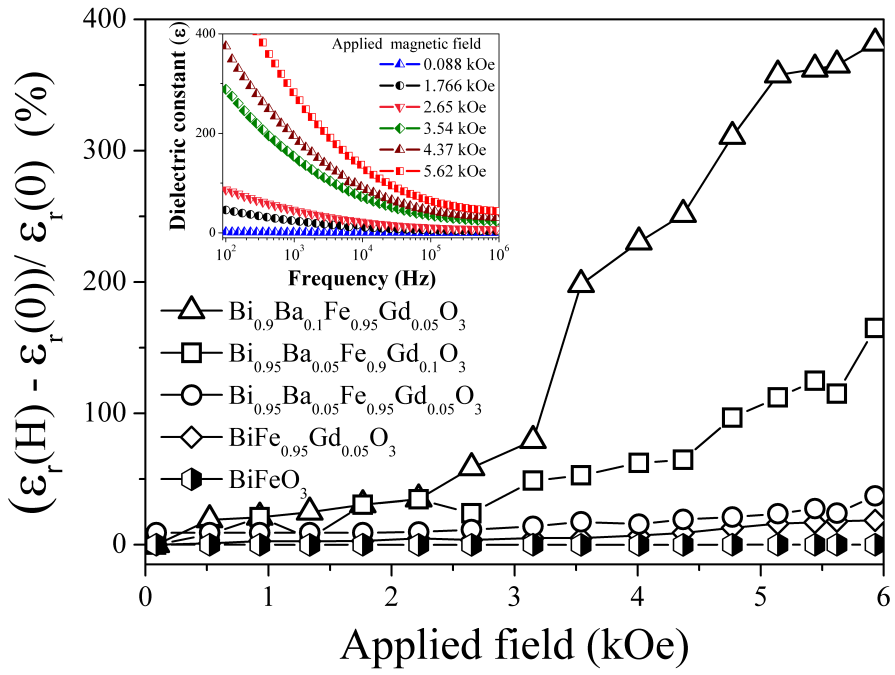

Figure 3.16: MD vs applied field plot of $Bi_{1-x}Ba_xFe_{1-y}Gd_yO_3$ $(0 \leq x, y \leq 0.1)$ ceramics at a frequency 1 kHz. Inset shows RT Dielectric constant vs frequency plot of $Ba_{0.1}Gd_{0.05}$BFO sample at different applied magnetic field.

relaxation might be coming from parallel combination of capacitance and resistance of grain and grain boundary. This peak shifts towards lower frequency with doping, with a decrease in the peak intensity. However, $Ba_{0.1}Gd_{0.05}$BFO and $Ba_{0.05}Gd_{0.1}$BFO samples show no signature of dielectric loss peak which indicates that space charge effect is reduced in these samples. As all the samples were prepared in a similar way we can ignore the possibility of space charge effect coming from the interface of electrode and ceramics.

Magnetic field dependence of ε, which is called magnetodielectric (MD) effect, is also measured to study ME coupling in doped samples. Figure 3.16 shows the field dependence of the MD effect, expressed by $[\varepsilon_r(\mathrm{H})\text{-}\varepsilon_r(0)]/\varepsilon_r(0)$, at a frequency 1 kHz, of all the samples. Though parent BFO shows very weak MD effect, it increases with doping. Above 2.5 kOe applied field MD increases dramatically in $Ba_{0.1}Gd_{0.05}$BFO and

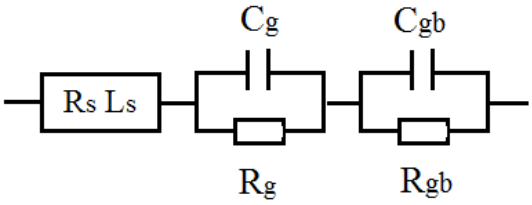

Figure 3.17: Equivalent circuit that represents the electrical properties of grain and grain boundary.

$Ba_{0.05}Gd_{0.1}BFO$ samples. In case of $Ba_{0.1}Gd_{0.05}BFO$, MD is $\sim$ 360 at 5.5 kOe field. So from the above observed data it can be said that Ba and Gd co-doped, $Ba_{0.1}Gd_{0.05}BFO$ sample exhibits better magnetoelectric coupling [21].

3.2.2.5 Impedance spectroscopy of $Bi_{1-x}Ba_xFe_{1-y}Gd_yO_3$ compounds

Complex impedance spectroscopy [48] is a very well known technique to describe the electrical properties of polycrystalline electro-ceramics. Grain and grain boundary contribution to the electrical properties (conductivity, dielectric constant) of the dielectric materials are better analysed using the equivalent circuit (Fig 3.17) and brick layer model for electro-ceramics. The equivalent circuit model consist two parallel RC circuits (R_gC_g and $R_{gb}C_{gb}$), R_S and L_S connected in series. Here, the low frequency response corresponds to $R_{gb}C_{gb}$ which is the grain boundary response, high frequency response corresponds to R_gC_g which is the grain response and R_SL_S represent the contribution from measuring leads and electrodes. Each semicircles appear in the impedance plot corresponds to the parallel RC component of the equivalent circuit.

Nyquist plots of -imaginary vs. real impedance data at different temperatures are shown in Fig 3.18(a-e). All Z^* (-Z'' vs Z') plots at different temperature ($\sim$ 30°C to 250°C) consist of a single high frequency arc which is centered on the real axis. In

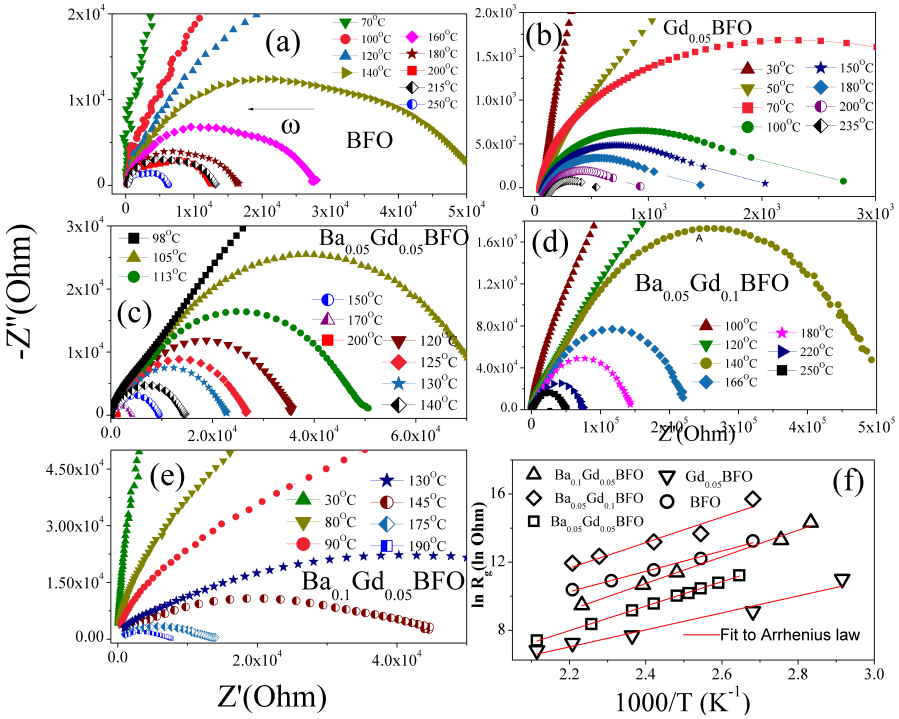

Figure 3.18: (a-e) Nyquist plot of impedance measured at different and (f) Arrhenius plot for the grain resistance temperatures of $Bi_{1-x}Ba_xFe_{1-y}Gd_yO_3$ ($0 \leq x, y \leq 0.1$) ceramics.

case of BFO, on increasing the temperature above 120°C a distorted arc (Fig 3.18(a)) is obtained which might be the indication of an additional component appearing at low frequencies. This high frequency semicircles can be identified as a bulk property from the fact that it passes through the origin and grain boundary effect is seemed to be eliminated [48, 49]. The resistance value for the grain (R_g) at a given temperature is equal to the intercept of the corresponding semicircle with x axis. Capacitance (C_g) related to grain can be calculated using R_g and frequency of maxima (f_{max}) of the semicircle from the equation,

$$\omega\tau = 2\pi f_{max} RC = 1 \tag{3.2}$$

Table 3.4: Various calculated parameters for $Bi_{1-x}Ba_xFe_{1-y}Gd_yO_3$ ($0 \leq x, y \leq 0.1$)

Sample	f_{max} (Hz)	R_g (kΩ cm)	C_g (pF cm^{-1})	E_r eV
BFO	6.9×10^4	282.8	8.16	0.48 ± 0.02
$Gd_{0.05}$BFO	3.4×10^6	2.49	18.80	0.41 ± 0.06
$Ba_{0.05}Gd_{0.05}$BFO	4.6×10^3	140	247.2	0.58 ± 0.005
$Ba_{0.05}Gd_{0.1}$BFO	6.2×10^3	670	38.45	0.61 ± 0.03
$Ba_{0.1}Gd_{0.05}$BFO	4.0×10^3	500.2	79.4	0.63 ± 0.03

Value of C_g obtained (Table 3.4) at 100°C for all the samples are of the order of pF. It is clear that R_g of all the samples decreases with increase in the temperature which might be due to the thermally activated change in conductivity of the samples. The resistance (R_g) obtained for the grain follows the Arrhenius law,

$$\tau = \tau_0 \, exp\left(\frac{E_r}{k_B T}\right) \tag{3.3}$$

where τ_0 is the prefactor, E_r is the activation energy for the dielectric relaxation, T is the absolute temperature and k_B is the Boltzman constant. Figure 3.18(f) shows the fitted curve for all the samples. Slope of the ln(R_g) vs 1000/T curve gives activation energy (E_r) which varies within 0.41-0.63 eV for all the samples (Table 3.4). This value is very close to the activation energy of La doped BFO sample for thermal motion of oxygen ion vacancies [44]. So here also the existence of a relaxation mechanism may be interpreted by the charge carriers created by oxygen vacancy hopping between neighbouring sites within the crystalline lattice. This E_r value decreases when only Gd is doped but

increases with co-doping. E_r for grain conduction is highest ($\sim 0.63 \pm 0.03$ eV) for $Ba_{0.1}Gd_{0.05}$BFO sample and is lowest ($\sim 0.41 \pm 0.06$ eV) for $Gd_{0.05}$BFO sample.

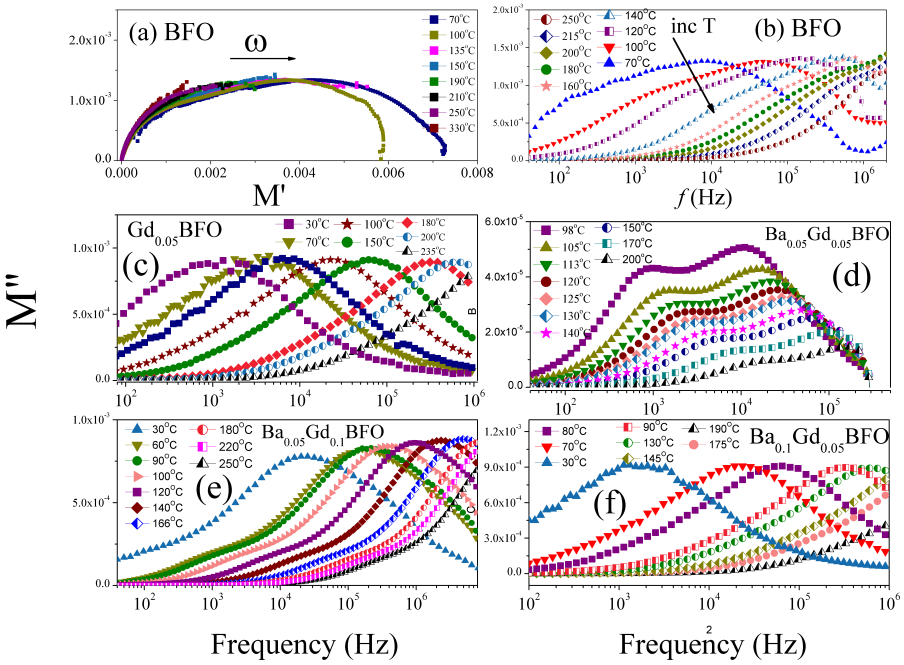

Figure 3.19: (a) Complex modulus plots of pure BFO and (b-f) M″ vs frequency plots of $Bi_{1-x}Ba_xFe_{1-y}Gd_yO_3$ ($0 \leq x, y \leq 0.1$) ceramics at different temperature.

Size of the semicircles appear in the impedance plot depends on the resistive responses of the components. If the difference in resistance between grain and grain boundary is large than it is very difficult to resolve the responses coming from grain and grain boundary. Whereas, electric modulus depends on capacitance value which could be helpful in understanding the different relaxations. Electric modulus (M″) is expressed as

$$M^* = M' + jM'' = j \times 2\pi f C_0 Z^* = j \times 2\pi f C_0 (Z' + jZ'') \tag{3.4}$$

where, $C_0 = \varepsilon_0 A/d$ is the geometrical capacitance. A is the electrode area and d is the distance between the electrodes [50]. Fig 3.19(a) shows the complex modulus

plot (M″ vs M′) of BFO at a temperature range from 70°C to 330°C. The depressed semicircle at temperature range (70°C to 100°C) indicates the possibility of having more than one relaxation in the sample [44]. But above 100°C only one arc is observed corresponding to the grain relaxation. M″ vs frequency plot for all samples at different temperatures is shown in Fig 3.19(b-f). All samples show a strong peak in the plot in between 1.5-10 kHz frequency range associated with the R_gC_g component of the circuit. Peak positions get shifted towards higher frequency with increasing temperature. In case of BFO, (Fig 3.19(b)) an inclination is observed (plot of 70°C) at higher frequency ($> 10^6$ Hz) side which might be coming from measuring leads and electrodes (L_sR_s). $Ba_{0.05}Gd_{0.05}$BFO sample shows two peaks, one at ∼1 kHz and another at ∼10 kHz (plot of 100°C). Whereas, $Ba_{0.05}Gd_{0.1}$BFO sample also shows a very weak peak at ∼1 kHz and a strong peak at frequency ∼10 kHz (plot of 100°C). But this peak at ∼1 kHz which might corresponds to the grain boundary response is absent in $Ba_{0.1}Gd_{0.05}$BFO sample. The abnormally small grain boundary response can be due to the presence of high ionic conductivity phase along the grain boundary which short circuit the grain boundary impedance. Otherwise, grain boundary peak in the other samples might occur at frequency below 40 Hz which is not possible to measure in our instrument.

3.2.2.6 AC conductivity measurements of $Bi_{1-x}Ba_xFe_{1-y}Gd_yO_3$

Figure 3.20 (a-e) shows the variation of ac conductivity (σ_{ac}) with frequency in the range 40-10^7 Hz and at different temperatures of the samples. All plots reflect a dispersion of σ_{ac} which shifts towards higher frequency with increasing temperature. In case of $Gd_{0.05}$BFO and $Ba_{0.05}Gd_{0.1}$BFO (Fig 3.20(b-d)), it is observed that σ_{ac} increases with frequency but at high frequency region ∼5-10 MHz, σ_{ac} starts decreasing again.

σ_{ac} increases with increase in frequency as the hopping of carriers increases. But at

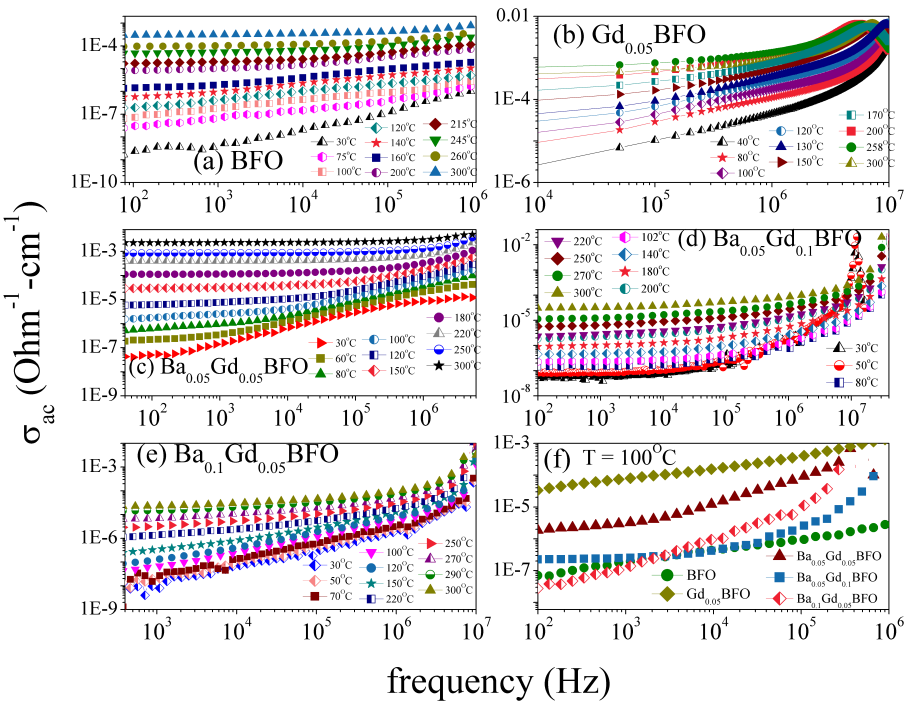

Figure 3.20: ac conductivity plots as a function of frequency (a-e) at different temperature and (f) at 100°C of $Bi_{1-x}Ba_xFe_{1-y}Gd_yO_3$ $(0 \leq x, y \leq 0.1)$ ceramics.

very high frequency it is difficult for the carriers to follow the applied field frequency so it lags behind the applied frequency, resulting in a drop in the σ_{ac} values. σ_{ac} consists of a flat and frequency independent region at low frequency region. With the increase in the temperature this flat region increases suggesting a dominant DC conduction behaviour in this region. At the same time, σ_{ac} also depends on the doping concentration. Fig 3.20(f) shows the change in σ_{ac} with doping variations at 100°C. σ_{ac} has increased after doping BFO with Gd but it start decreasing in the co-doped samples. $Ba_{0.1}Gd_{0.05}BFO$ has minimum σ_{ac} value among all the samples. σ_{ac} of a material can be written as [51],

$$\sigma_{ac}(T) = \sigma_1(T) + \sigma_1(T) \tag{3.5}$$

where, the first term is the frequency dependent component of ac conductivity, which is

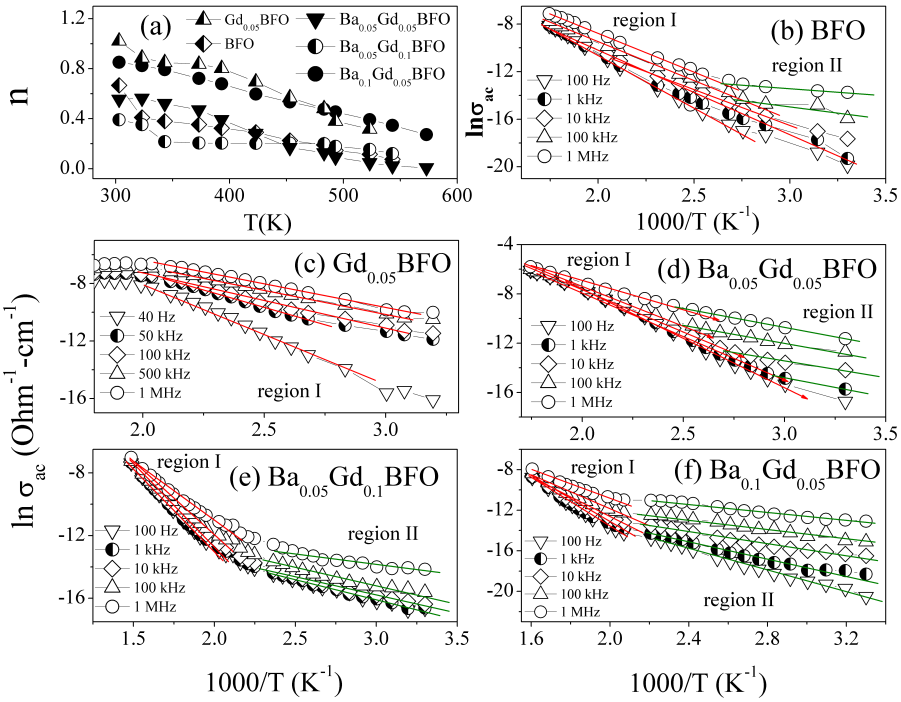

Figure 3.21: (a) Variation of η with temperature and (b-f) ac conductivity vs 1000/T (K^{-1}) plots of $Bi_{1-x}Ba_xFe_{1-y}Gd_yO_3$ ($0 \leq x, y \leq 0.1$) ceramics at different frequency.

related with the dielectric relaxation due to the localized electric charge carriers. $\sigma_1(T)$ is given by,

$$\sigma_1(\omega, T) = A(T)\omega^{\eta}(T) \tag{3.6}$$

where the parameter η is dimensionless and A has the unit of conductivity. Slope of $\ln(\sigma_{ac})$ vs $\ln(\omega)$ plot gives η value of the material at that temperature. Figure 3.21(a) shows the temperature dependence of η value of the samples. It is well known that the nature, how η varies with temperature, can suggest the conduction mechanism in the material depending on various model [44, 51, 52, 53, 54]. (i) If η is independent of temperature then the conduction can be explained by quantum mechanical tunnelling (QMT), (ii) correlated barrier hopping (CBH) is expected when η decreases with the temperature, (iii) increase of η with the temperature can be correlated with small po-

Table 3.5: Activation energy and η value for $Bi_{1-x}Ba_xFe_{1-y}Gd_yO_3(0 \leq x, y \leq 0.1)$ ceramics.

Sample	Region I E_a (eV)					Region II E_a (eV)					η at
	100 Hz	1 kHz	10 kHz	100 kHz	1 MHz	100 Hz	1 kHz	10 kHz	100 kHz	1 MHz	30°C 300°C
BFO	0.72	0.54	0.50	0.53	0.53	NA	NA	NA	0.18	0.11	0.66 – 0.07
$Gd_{0.05}$BFO	0.56	0.39	0.31	0.27	0.27	NA	NA	NA	NA	NA	1.0 – 0.31
$Ba_{0.05}Gd_{0.05}$BFO	0.65	0.61	0.57	0.53	0.40	NA	0.26	0.21	0.23	0.25	0.56 – 0.01
$Ba_{0.05}Gd_{0.1}$BFO	0.87	0.85	0.85	0.75	0.62	0.21	0.21	0.19	0.19	0.11	0.39 – 0.12
$Ba_{0.1}Gd_{0.05}$BFO	0.99	0.91	0.82	0.69	0.45	0.44	0.35	0.24	0.19	0.16	0.85 – 0.27

laron conduction while if η reaches a minima followed by an increase with further increase in temperature than an overlapping large polaron tunnelling (OLPT) is the dominant conduction mechanism. It is very clear from Fig 3.21(a) that for all samples η decreases slowly with increasing temperature (Table 3.5). Therefore, CBH is the expected conduction mechanism in the Ba doped and Ba-Gd co-doped samples.

The second term of Equ 3.5, $\sigma_2(T)$ is the DC conductivity which corresponds to the drift of charge carriers and follows Arrhenius relation,

$$\sigma_2(T) = \sigma_0 \, exp\left(-\frac{E_a}{K_B T}\right) \tag{3.7}$$

where, σ_0 is the pre-exponential factor and E_a is the activation energy for charge conduction. Fig 3.21(b-e) shows the variation of $\ln(\sigma_{ac})$ with the inverse of temperature (in K scale) at different frequencies for all the compositions. Conductivity behaviour shows two regions, region I where the conductivity is strongly temperature dependent but almost frequency independent and region II where the conductivity is strongly dependent on frequency but weakly temperature dependent. Temperature division for region I and II is different for all the samples. The activation energy of the samples for intrinsic

conduction at different frequencies can be found from the slope of the curves (Table 3.5). It is observed that activation energy decreases with increase in frequency. The value of activation energy of the samples in region I varies from 0.27 to 0.99 eV which indicates long range motion of oxygen vacancy contribution in the conduction mechanism [44]. Whereas in region II, value and variation of activation energy is very small with doping which indicates that short range hopping motion of oxygen vacancy and impurity conduction might prevailed in this temperature region. One of the possible explanation of anomaly in activation energy value is the substitution of Ba and Gd in place of Bi and Fe in the unit cell. AC conductivity in the samples is mainly due to the hopping of oxygen vacancy between the oxidation states of $Fe^{+3}-O-Fe^{+2}$ ion. Oxygen vacancy arises in BFO due to the volatile nature of Bi. So co-doping has an indirect but appreciable effect on hopping conduction in the samples.

3.3 Conclusion

This work verifies the effect of single site doping and co-doping on the multiferroic properties of BFO. Through tuning the sintering temperature of chemical synthesis procedure, we have successfully prepared Ba doped and Ba-Gd co-doped Bismuth ferrite samples.

Above the Néel temperature of pure BFO, a large enhancement in magnetization is observed in Ba doped samples. Transition temperatures (magnetic and ferroelectric) shift towards higher temperature with the increase in dopant concentration. Canting of spins and displacement of oxygen atoms from its original position could be the reasons for enhanced magnetic and ferroelectric properties respectively. The noticeable change in dielectric constant with doping and the observed change in lattice parameters indirectly confirm that Ba is not remaining isolated in the compound but enters the lattice. Mag-

netoelectric coupling also increases due to Ba substitution. Measurements of electric properties illustrate a remarkable difference in dielectric constant above the magnetic transition temperature of the parent compound.

Distortion in the lattice structure arises due to Ba and Gd co-doping which decisively influences the magnetic properties of BFO. Gd doping induces RT ferromagnetism in BFO ceramics which increases again with replacing Bi with Ba. Gd rich, $Ba_{0.05}Gd_{0.1}$BFO shows maximum magnetization both at 80 K and at 300 K. Change in Fe−O bond length due to the doping gives rise to the ferromagnetic behaviour in the ceramics. Due to high resistivity, well saturated *P-E* hysteresis loop is observed in $Ba_{0.1}Gd_{0.05}$BFO with a remanent polarization, $P_r \sim 8.82\,\mu C/cm^2$ at RT. The anomaly in ε value of all the ceramics at $\sim 385^{\circ}$C is thought to arise from magnetic ordering. Impedance spectroscopy and electrical modulus plots suggest only one relaxation in the frequency range $40 - 10^7$ Hz which is preferably due to the grain contribution. The grain resistance follows Arrhenius law associated with a highest activation energy ~ 0.63 eV in case of $Ba_{0.1}Gd_{0.05}$BFO sample which is almost same with the activation energy obtained from the frequency independent region of ac conductivity data. Decrease in the η value with temperature implies that the charge transport is assisted by correlated barrier hopping mechanism. Although, magnetization and remanent polarization value of Ba and Gd co-doped BFO is smaller than other rare earth doped BFO thin films or nanostructures, presence of enhance magnetoelectric behavior at RT makes this material a true multiferroic.

References

[1] S-W. Cheong and M. Mostovoy , Nat. Mater. 6, 13-20 (2007).

[2] Chin-Feng Chung, Jen-Po Lin and Jenn-Ming Wu, Appl. Phys. Lett. 88, 242909 (2006).

[3] Monoj Kumar, K. L. Yadav, Appl. Phys. Lett. 91, 242901 (2007).

[4] K. Jawahar and R.N.P.Choudhary, Indian Journal of Engineering and Material Sc. 15 (2008).

[5] Z. Cheng, X. Wang, S. Dou, Phys. Rev. B 77, 092101 (2008).

[6] J. W. Lin, Y.H. Tang, C. S. Lue, J. G. Lin, Appl. Phys. Lett. 96, 232507 (2010).

[7] D. H. Wang, W. C. Goh, M. Ning, and C. K. Ong, Appl. Phys. Lett. 88, 212907 (2006).

[8] Meiya Li, Min Ning, Yungui Ma, QibinWu and C K Ong, J. Phys. D: Appl. Phys. 40, 16031607 (2007).

[9] V. B. Naik and R. Mahendiran, Solid State Commun. 149, 754-758 (2009).

[10] V A Khomchenko, M Kopcewicz, A M L Lopes, Y G Pogorelov, J P Araujo, J M Vieira and A L Kholkin, J. Phys. D, 41, 102003 (2008).

[11] T. Ishidate, S. Abe, Phys. Rev. Lett. 78, 12 (1997).

[12] J.R. Sahu, C.N. Rao, Solid State Sci. 9, 952953 (2007).

[13] W. Eerenstein, F. D. Morrison, J. Dho, M. G. Blamire, J. F. Scott, and N. D. Mathur, Science 307, 1203a (2005).

[14] F. Huang, X. Lu, Weiwei Lin, X. Wu, Yi Kan, and J. Zhu, Appl. Phys. Lett. 89, 242914 (2006).

[15] J. Wang, A. Scholl, H. Zheng, S. B. Ogale, D. Viehland, D. G. Schlom, N. A. Spaldin, K. M. Rabe, M. Wuttig, L. Mohaddes, J. Neaton, U. Waghmare, T. Zhao, and R. Ramesh, Science 307, 1203b (2005).

[16] S.K. Pradhan, J. Das, P.P Rout, S.K. Das, J. Magn. Magn. Mater. 322, 3614-3622 (2010).

[17] Shamir N, Gurewitz E and Shaked H Acta Crystallogr. A 34, 662 (1978).

[18] T. Kojima, T. Sakai, T. Watanabe, H. Fanakubo, K. Saito, M.Osada, Appl. Phys. Lett. 80, 2746 (2002).

[19] J. F. Scott, J. Phys. Cond. matter, 20, 021001 (2008).

[20] C. H. Yang, T. Y. Kao and Y. H. Jeong, Solid State Commun. 134, 299 (2005).

[21] Youn-Ki Jun, Won-Taek Moon, Chae-Myung Chang, Hyun-Su Kim, Hyun Sam Ryu, Jae Wook Kim, Kee Hoon Kim and Seong-Hyeon Hong, Solid State Commun. 135, 133137 (2005).

[22] T. Kimura, S. Kawamoto, I. Yamada, M. Azuma, M. Takano and Y. Tokura, Phys. Rev. B 67, 180401(R) (2003).

[23] V. R. Palkar, Darshan C. Kundaliya, S. K. Malik and S. Bhattacharya, Phys. Rev. B 69, 212102 (2004).

[24] Z. X. Cheng, X. L. Wang, H. Kimura, K. Ozawa and S. X. Dou Appl. Phys. Lett. 92, 092902 (2008).

[25] Benfang Yu, Meiya Li, JingWang, Ling Pei, Dongyun Guo and Xingzhong Zhao J. Phys. D: Appl. Phys. 41, 185401 (2008).

[26] G. D. Hu, X. Cheng, W. B. Wu, and C. H. Yang, Appl. Phys. Letts., 91, 232909 (2007).

[27] V. A. Khomchenko, D. A. Kiselev, I. K. Bdikin, V. V. Shvartsman, P. Borisov, W. Kleemann, J. M. Vieira and A. L. Kholkin, Appl. Phys. Lett. 93, 262905 (2008).

[28] A. Lahmar, S. Habouti, M. Dietze, C.-H. Solterbeck, and M. Es-Souni, Appl. Phys. Letts., 94, 012903 (2009).

[29] R. Das and K. Mandal, J. Magn. Magn. Mater. 324, 1913 (2012).

[30] Z.X. Cheng, A.H. Li, X.L. Wang, S.X. Dou, K. Ozawa, H. Kimura, S.J. Zhang, T.R. Shrout, J. Appl. Phys. 103, 07E507 (2008).

[31] G. Le Bras, D. Colson, A. Forget, N. Genand-Riondet, R. Tourbot, P. Bonville, Phys. Rev. B 80, 134417 (2009).

[32] A. Ianculescu, F. Prihor, P. Postolache, L. Mitoseriu, N. Dragan and D. Crisan, Ferroelectrics, 391, 6775 (2009).

[33] S.K. Pradhan and B.K.Roul, J. Phys. and Chem. Solids 72, 11801187 (2011).

[34] Liang Fang, Jian Liu, Sheng Ju, Fengang Zheng, Wen Dong, and Mingrong Shenc, Appl. Phys. Lett. 97, 242501 (2010).

[35] C. Rath, P. Mohanty, A. C. Pandey and N. C. Mishra, J. Phys. D: Appl.Phys. 42, 205101 (2009).

[36] Y. B. Lin, Y. M. Yang, B. Zhuang, S. L. Huang, L. P. Wu, Z. G. Huang, F. M. Zhang and Y. W. Du, J. Phys. D: Appl. Phys. 41, 195007 (2008).

[37] P. Uniyal and K. L. Yadav, J. Appl. Phys. 105, 07D914 (2009).

[38] I A Sergienko and E. Dagotto, Phys. Rev. B 73, 094434 (2006).

[39] D. Coffey, T. M. Rice and F. C. Zhang, Phys. Rev. B 44, 10112 (1991).

[40] A. M. Kadomtseva, A. K. Zvezdin, F. Y. Popov, A. P. Pyatakov and G. P. Vorob'ev, JETP letters 79, 571 (2004).

[41] G. Catalan G and J. F. Scott, Adv. Mater. 21, 24632485 (2009).

[42] Radheshyam Rai, Sunil Kumar Mishra, N.K. Singh, Seema Sharma and Andrei L. Kholkin Current Applied Physics 11, 508-512 (2011).

[43] A. K. Jonscher, Nature 267, 673 (1977).

[44] P. Pandit, S. Satapathy and P. K. Gupta, Phy. B 406, 2669-2677 (2011).

[45] 37. Y. Chen, X. Yu Zhang, C. Vittoria, V. G. Harris, Appl. Phys. Lett. 94, 102906 (2009).

[46] J. X. Zhang, J. Y. Dai, W. Lu, H. L. W. Chan, B. Wu and D. X. Li, J. Phys. D: Appl. Phys. 41, 235405 (2008).

[47] J. X. Zhang, J. Y. Dai and H. L. W. Chan, J. Appl. Phys. 107, 104105 (2010).

[48] Macdonald J R, Johnson W B 2005 Impedance Spectroscopy Theory, Experiments and Applications, in: E. Barsoukov, J.R. Macdonald (Eds.), John Wiley & Sons Inc, Hoboken, NJ.

[49] K. Majhi, B. S. Prakash and K. B. R. Varma, J. Phys. D: Appl. Phys. 40, 7128 (2007).

[50] A. Srivastava, A. Garg and F. D. Morrison, J. Appl. Phys. 105, 054103 (2009).

[51] E. V. Gopalan, K. A. Malini, S. Saravanan, D. S. Kumar, Y. Yoshida, M. R. Anantharaman, J. Phys. D: Appl. Phys. 41, 185005 (2008).

[52] T. M. Meaz, S. M. Attia and A. M. Abo El Ata, J. Magn. Magn. Mater. 257, 296 (2003).

[53] A. Ghosh, Phys. Rev. B 42, 1388 (1990).

[54] M. K. Fayek, M. F. Mostafa, F. Sayedahmed, S. S. Ata-Allah and M. Kaiser, J. Magn. Magn. Mater 210, 189-195 (2000).

4 Study of undoped and doped $BiFeO_3$ thin films

Thin films with strong magnetic properties as well as excellent ferroelectric properties (large remanent polarization, small coercive field and fatigue-free properties) are required for practical applications which are very difficult to get in bulk $BiFeO_3$ due to (i) cancellation of microscopic magnetization in spiral spin structure and (ii) high leakage current. It is reported that different ion such as Ba, Mn, Sr, La, Pr etc. substitution enhances ferroelectric and magnetic properties of $BiFeO_3$ [1, 2, 3, 4]. It has also been demonstrated that suppression of the G-type spiral spin structure in $BiFeO_3$ thin films give rise to an enhanced magnetic property [5, 6]. Wang et al reported large polarization ($\sim$60 $\mu C/cm^2$) in $BiFeO_3$ thin film, for the first time [7]. Thinner $BiFeO_3$ film on $BaPbO_3$/Pt/Ti/SiO_x/Si shows smaller polarization value and higher retention properties compared to the thicker films [8]. In case of La doped $BiFeO_3$ film, thickness also has a strong influence on the piezoelectric properties of the film [9]. Epitaxial strain in $BiFeO_3$ thin films creates self-assembled ferroelectric domains [10, 11].

4.1 Influence of film thickness on ferroelectric and magnetic properties of $Bi_{1-x}Ba_xFeO_3$ thin films

4.1.1 Background

Though Ba doped $BiFeO_3$ (BFO) thin film [12] has been studied earlier, yet little attention is focused on the studies of the effect of thickness and surface morphology on their multiferroic properties. It is well known that the grain size and surface topography of thin films depends on the film thickness which influences the dielectric, ferroelectric and transport properties of the materials remarkably. Furthermore, the magnetic properties of the BFO, which has a long range (∼62 nm) spiral spin structure, can also be tailored by controling the film thickness.

In previous chapter we have observed that 15% Ba doped BFO sample shows maximum magnetic property and enhanced ME property at RT. Therefore, it is very interesting to explore how this material behaves in nanostructure. In our present work, undoped and Ba doped BFO thin films are fabricated on Si (100) substrate by employing the pulse laser deposition (PLD) technique. Herein, the Si substrate is chosen considering its application in electronic devices. Undoped BFO film with thickness 115 nm and $Bi_{0.85}Ba_{0.15}FeO_3$ film (henceforth written as $Ba_{0.15}$BFO) with thickness 29, 46, 68 and 113 are prepared to study the structural, magnetic, dielectric and ferroelectric properties of the films. Detail study shows that Ba doped films show better multiferroic properties compare to the undoped BFO film. It is found that magnetization and electric polarization changes significantly with the film thickness. Impact of the film thickness on the dielectric properties is also discussed.

4.1.2 Results and Discussion

4.1.2.1 Morphology and Crystal structure of $Bi_{1-x}Ba_xFeO_3$ thin films

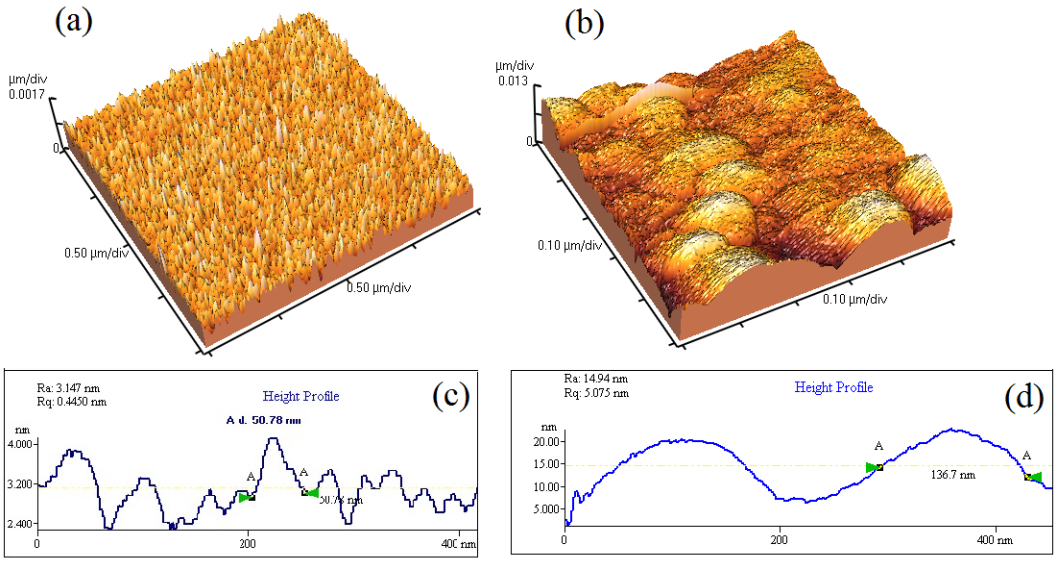

Figure 4.1: AFM image of the surface of $Bi_{0.85}Ba_{0.15}FeO_3$ films with thickness (a) 29 nm and (b) 113 nm. Grains size distribution of (c) 29 nm and (d) 113 nm films.

Figure 4.1 is an AFM image of the surface of $Bi_{0.85}Ba_{0.15}FeO_3$ ($Ba_{0.15}$BFO in short) films with thickness 29 nm (Fig 4.1(a)) and 113 nm (Fig 4.1(b)) prepared on Si substrate kept at 650°C during deposition. It can be seen clearly that the microstructure of the films are very different from each other. Fig 4.1(c-d) shows the distribution of grains size in 29 and 113 nm film respectively. The thinner film shows a more dense and homogeneous distribution of grains (size∼50-60 nm) compared to thicker film. In 113 nm film, we observe that small grain accumulation leads to the formation of larger grains with a subsequent increase in the measured lateral grain size (∼120-150 nm) leading to an overall rougher surface. Films, with thickness varying from 17 to 113 nm, show different surface topography with a change in RMS roughness from 0.16 nm to 5.07 nm (Fig 4.2). The RMS roughness does not change much up to a thickness ∼46 nm, but

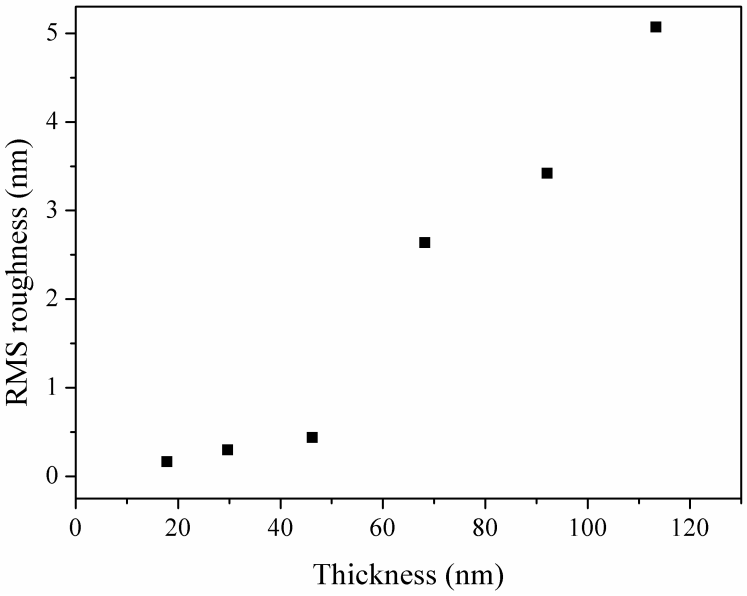

Figure 4.2: Dependence of surface roughness of $Bi_{0.85}Ba_{0.15}FeO_3$ films on the thickness of the films.

above that, it increased dramatically. These results indicate S-K growth mode (layer by layer growth plus island growth) of $Ba_{0.15}$BFO film [13]. Annealing of the films after deposition also has an influence on grain size. Though surface roughness remains almost the same, grain size increases by 10-20 nm on annealing at 300°C.

Figure 4.3 shows the XRD profile of $Ba_{0.15}$BFO thin films with thickness 29, 46, 68 and 113 nm and of BFO thin film with thickness 115 nm. All the films show a rhombohedral structure with space group R3m in contrast to the Ba doped BFO nanoparticle, reported earlier [14]. $Ba_{0.15}$BFO thin films with thickness upto 68 nm is crystallized preferably along (100) direction while 113 nm $Ba_{0.15}$BFO and 115 nm BFO film show a strong orientation along (110)/($1\bar{1}0$) direction. No other impurity phase, such as $Bi_2Fe_4O_9$, is observed [15]. Direction of lattice growth in thin films strongly depends on the lattice parameter of the substrates. Mismatch in lattice parameter between Si and BFO gives rises to strain which might be the reason behind (100) directional growth in thinner films. With the increase in deposition time crystalline quality of the films also

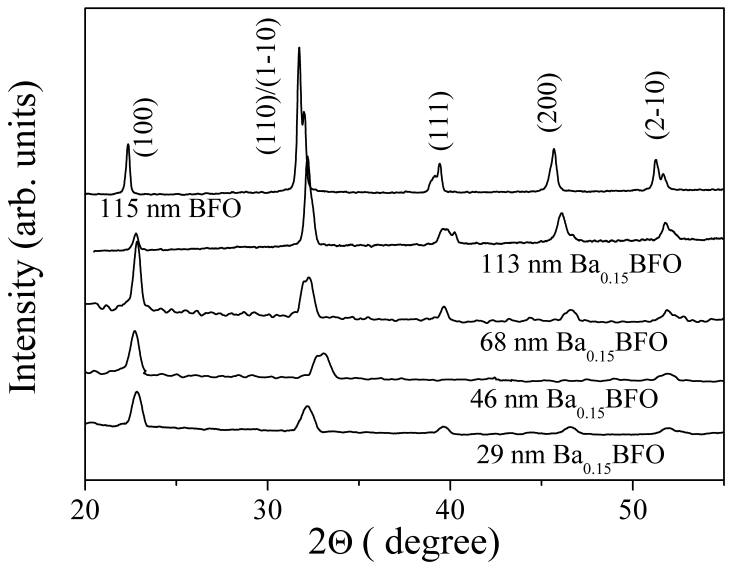

Figure 4.3: XRD pattern of $BiFeO_3$ and $Bi_{0.85}Ba_{0.15}FeO_3$ films deposited on Si substrate.

increases.

4.1.2.2 Ferroelectric properties of $Bi_{1-x}Ba_xFeO_3$ thin films

Fig 4.4 shows that BFO and $Ba_{0.15}$BFO films are ferroelectric in nature. Ba doped films with thickness higher than 46 nm shows better polarization value compared to the undoped 115 nm BFO film. Only 29 nm $Ba_{0.15}$BFO film shows leakage nature. This might be due to the presence of dead layers in the Si substrate and film interface. Ba doping reduces the oxygen vacancies, which is one of the main sources of movable charges in BFO, leading to a more insulating film. Room temperature P-E hysteresis loops of $Ba_{0.15}$BFO films with different thickness are shown in Fig 4.4. All the films shows well saturated P-E loop. The remanent polarization (P_r) is 4.2, 17.1 and 21.79 μC/cm^2 of the $Ba_{0.15}$BFO films with thickness 46, 68 and 113 nm, respectively. Coercive field (E_C) of 46, 68 and 113 nm films is 27.1, 9.61 and 11.53 kV/cm, respectively. 115 nm undoped BFO film shows lower polarization (P_r=9.19 μC/cm^2) compared to the 113 nm $Ba_{0.15}$BFO film. The low P_r value of 46 nm $Ba_{0.15}$BFO film may be due to the following

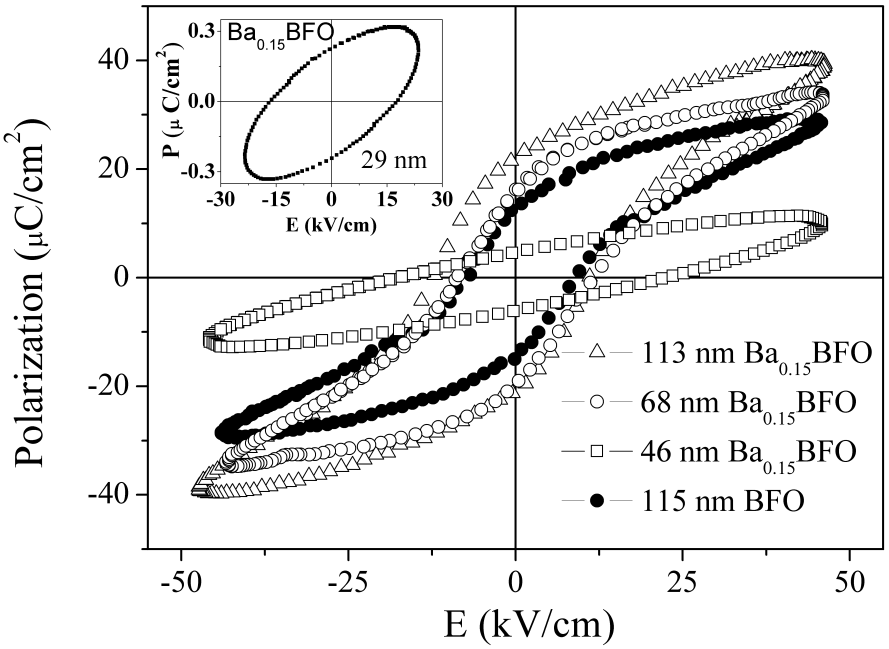

Figure 4.4: Ferroelectric hysteresis loop of $BiFeO_3$ and $Bi_{0.85}Ba_{0.15}FeO_3$ films at room temperature.

reasons (i) absence of its crystal orientation along (111) direction, as the spontaneous polarization is oriented in the direction $[111]_c$ of the pseudocubic perovskite BFO unit cell [16], (ii) poor electrical properties in dead layers. However the large ferroelectricity in the doped films compared to pure BFO may also be attributable to the tilting of FeO_6 octahedra derived from the substitution of Ba^{2+} on the Bi^{3+} site, as Ba^{2+} (1.49 Å) has bigger radius compared to Bi^{3+} (1.17 Å)).

4.1.2.3 Dielectric properties of $Bi_{1-x}Ba_xFeO_3$ thin films

Thickness dependent dielectric constant (ε) of the BFO (115 nm) and $Ba_{0.15}$BFO films (46, 68 and 113 nm) as a function of frequency in the range from 40 Hz to 1.2 MHz at RT is shown in Fig 4.5. It shows strong frequency dependence in the low frequency range, while relaxation of the dipoles is observed in the 0.2 MHz to 1.2 MHz frequency range. All curves obey the Debye relaxation expression. It is found that the 113 nm

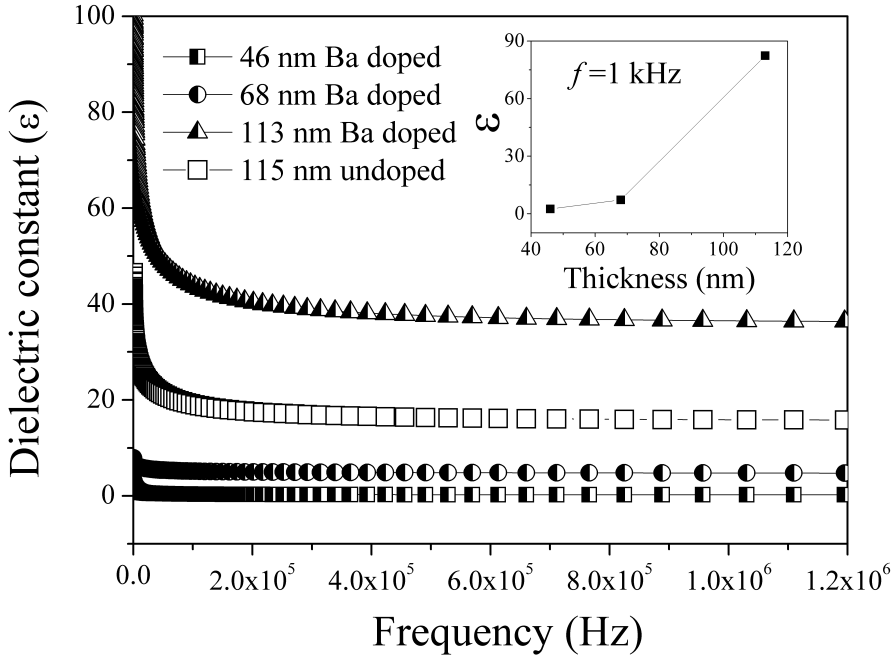

Figure 4.5: Dielectric constant (ε) of $BiFeO_3$ and $Bi_{0.85}Ba_{0.15}FeO_3$ films with different thickness at room temperature. Inset: thickness dependent ε value of the $Bi_{0.85}Ba_{0.15}FeO_3$ films at f= 1 kHz.

$Ba_{0.15}$BFO film exhibits higher value of dielectric constant compared to the 115 nm BFO film and other $Ba_{0.15}$BFO thin films. The value of ε was found to be almost 40 times higher ($\varepsilon = 82.36$) in 113 nm film than the 46 nm film at a frequency of 1 kHz (Inset of Fig 4.5). The ε value of 46 nm and 68 nm film is very close (2.44 and 7.18 respectively at 1 kHz frequency) to each other. Better dielectric properties in Ba doped film might be due to the further distortion in the FeO_6 due to the Ba doping on Bi site. On the other hand, huge ε value in 113 nm film compared to other $Ba_{0.15}$BFO films indicates the possible existence of dead layers (layers having weak capacitance value) on the film-substrate interface. Existence of dead layer in series with the $Ba_{0.15}$BFO film reduces the dielectric constant value dramatically [9, 17]. Dead layers in thin films could arise from growth induced defects, strains and grain boundaries [18]. As grain size is higher in thicker films (Fig 4.1), high value of ε in the thicker film can occur due to the charge

carrier accumulation in the interface of the grain and grain boundaries [19].

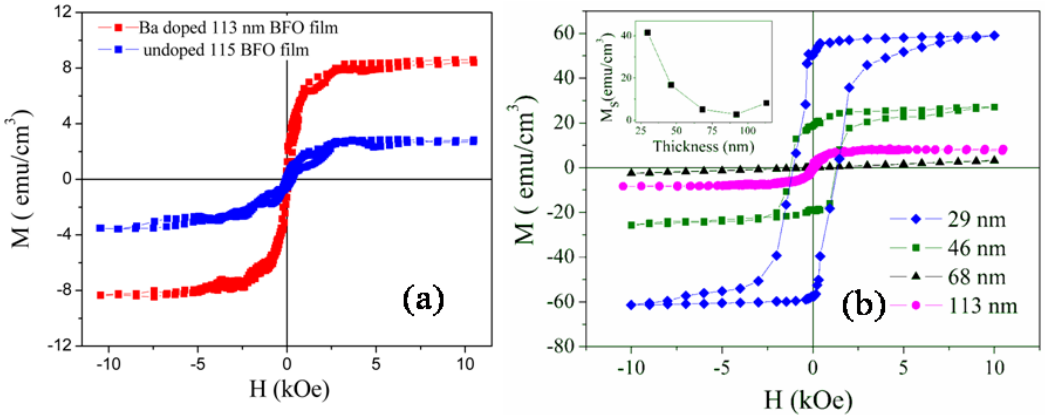

Figure 4.6: (a) In-plane magnetic hysteresis loops of $BiFeO_3$ and $Bi_{0.85}Ba_{0.15}FeO_3$ thin films and (b) M-H loops of $Bi_{0.85}Ba_{0.15}FeO_3$ thin films with different thicknesses at room temperature. Inset: the thickness dependent M of $Bi_{0.85}Ba_{0.15}FeO_3$ thin films at 10 kOe.

4.1.2.4 Magnetic properties of $Bi_{1-x}Ba_xFeO_3$ thin films

Room temperature (RT) magnetization (M) versus magnetic field (H) data of the BFO and $Ba_{0.15}$BFO films with different thickness is shown in Fig 4.6, after subtracting diamagnetic contribution of Si substrate. Field is applied parallel to the films surface. Considering that the magnetic behaviour of the films depends on the deposition parameters, all the films are synthesized under same conditions. From our experimental data, (Fig 4.6(a)) it is very clear that, both BFO and $Ba_{0.15}$BFO films with similar thickness shows ferromagnetic behaviour at RT. But, $Ba_{0.15}$BFO film shows better magnetic properties compared to the undoped film. Fig 4.6(b) shows that all the Ba doped $Ba_{0.15}$BFO films, except one with 68 nm thickness shows ferromagnetic behaviour at room temperature. Replacing Bi with different ions changes the canting angle of spins which might be a significant reason behind strong ferromagnetic property in Ba doped BFO thin films. With increasing film thickness, the following effects are noted: (i) Film

with thickness 29 nm have highest saturation magnetization (M_S) ∼41.1 emu/cm^3 (corresponds to ∼0.33 μB per unit cell); as film thickness increases to 46 nm magnetization decreases to ∼16.66 emu/cm^3. (ii) 68 nm films show linear M-H behaviour with very low H_C (∼ 2 Oe) value, (iii) Film with thickness > 68 nm shows ferromagnetic loop. M_S again enhances with further increase in film thickness (Inset of Fig 4.6). Figure 4.7(a) shows that the influence of film thickness on coercivity (H_C) of $Ba_{0.15}$BFO films. 46 nm thick films show maximum H_C (∼1.25 kOe), while H_C value of films with higher thickness reduces dramatically.

In BFO, magnetic ions are coupled ferromagnetically within the (111) planes and anti-ferromagnetically between adjacent planes. Nanostructures of antiferromagnetic BFO show magnetic moment mainly due to the incomplete magnetic compensations between these planes. This incomplete magnetic orderings in thin films occurs as the long- range antiferromagnetic order is frequently interrupted at the grain surfaces [20]. From our experimental data it is very clear that magnetic properties of the films increases with decrease in film thickness. Increase in the grain size with film thickness (Fig 4.1) reduces the interruption of long range antiferromagnetic order at the grain surface. Therefore magnetization drops noticeably when film thickness increases above 29 nm. Néel attributed [21, 22, 23] that in case of single domain antiferromagnetic particles susceptibility was expected to scale as ∼1/d (surface to volume ratio). Fig 4.7(b) shows a plot of the magnetization as a function of 1/d at an applied field of 10 kOe. Magnetization of the films with thickness 29 to 68 nm shows linear behaviour with 1/d indicating that the Néel model is applicable in these films. Linear M vs H behaviour in 68 nm film where film thickness is very close with the wavelength of complicated cycloidal spin structure of BFO along the $[110]_h$ axis, emphasize that the Néel model is more applicable in our case.

Induced magnetic moment in thin films due to epitaxial strain is a controversial issue

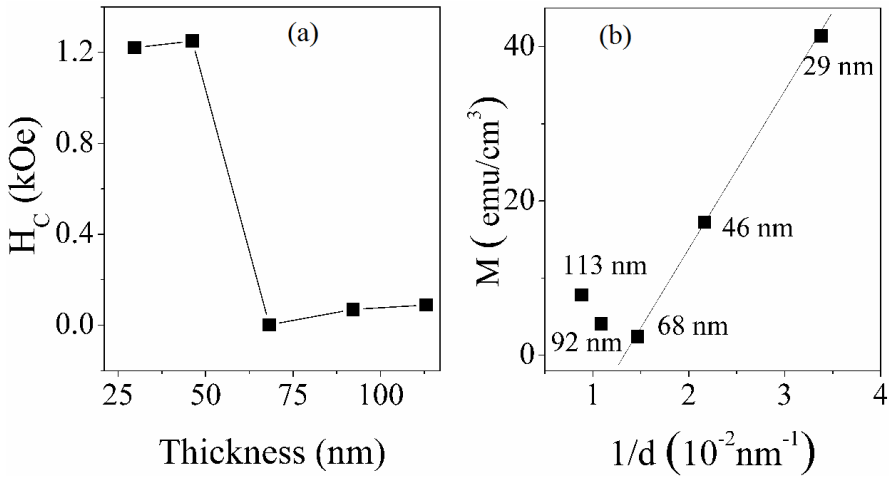

Figure 4.7: (a) Thickness dependent coercivity (H_C) of the films, (b) corresponding magnetization values at 10 kOe as a function of 1/d of $Bi_{0.85}Ba_{0.15}FeO_3$ thin films.

among different groups as there is no agreement between theory and experiments. The theory predicts that the polar displacements cannot enhance the magnetic moment [24]. However recently, decrease in magnetization value with the increase in pure BFO film thickness deposited on different substrates is reported due to the lattice misfit between the film and the substrate [25, 26]. In our case, the Ba doped film is polycrystalline. So the substrate stress might not play any role in the large change of magnetization of Ba doped film. Existence of Fe^{2+} state also increases magnetic properties [27, 28]. J. Wang, et al reported that [27] in 30 nm BFO film ratio of Fe^{2+}(oct):Fe^{3+}(oct):Fe^{3+}(tet) is 1:1:1 while amount of Fe^{2+} decreases with the increase in film thickness. All these observations together explain the reason of highest magnetic behaviour in the 29 nm film and comparatively lower magnetic property for thicker films.

However, the above mentioned approaches fail in case of the films with thickness above 68 nm as small increase in M_S and H_C value is observed in films with higher thickness. This result is consistent with that reported for other magnetic nanomaterials [29]. Monte Carlo simulations [30] of magnetic particles shows that the magnetization

at high fields becomes lower with the increasing particle concentration i.e. the inter particle interaction in thin films. Exchange interaction in ferromagnetic core plays a role in increasing M_S value with film thickness. Magnetization in nanostructure in less compared to the bulk due to the spin disorder on the surface which is consider as a non magnetic layer. Therefore, the increase of the magnetization in the films with thickness above 68 nm could be explained by considering a nonmagnetic layer on the surface, the thickness of which decreases as the grain size goes up.

4.2 Conclusion

Multiferroic $BiFeO_3$ and $Bi_{0.85}Ba_{0.15}FeO_3$ thin films are successfully prepared on Si(100) substrate by PLD techniques. Ba doped film with thickness 113 nm shows better magnetic, ferroelectric and dielectric properties compare to the undoped $BiFeO_3$ film with thickness 115 nm. The remanent polarization and saturation magnetization of polycrystalline Ba doped $Bi_{0.85}Ba_{0.15}FeO_3$ thin films are higher compared to the earlier reported Ba (x=0.25) doped Bismuth ferrite thin films [5]. Ferroelectic properties of the films depend on the crystallization direction and surface morphology which can be controlled by the substrate temperature during film deposition. Thinner films show weak dielectric properties perhaps due to the existence of dead layers in the interface of substrate and the film. While thicker film exhibit better P-E hysteresis loop and dielectric properties. Magnetic property (coercivity, saturation magnetization) is very sensitive to the film thickness. Films with thickness close to $\sim$62 nm which is the wavelength of spiral magnetic spin structure of antiferromagnetic BFO, shows antiferromagnetic behaviour. Films with lower or higher (less than double of 62 nm) thickness shows ferromagnetic nature. These findings suggest that the results could be correlated with (i) the suppression of long range spiral spin structure in films with thickness $<$ 68 nm and (ii) influence

of the thickness of non magnetic layer (random spin ordering on the film surface) on the magnetic property of thicker (> 68 nm) films.

References

[1] Y. H. Lee, J. M. Wu, and C. H. Lai, Appl. Phys. Lett. 88, 042903 (2006).

[2] B. Yu, M. Li, Z. Hu, L. Pei, D. Guo, X. Zhao, and S. Dong, Appl. Phys. Lett. 93, 182909 (2008).

[3] H. D. Zhou, J. C. Denyszyn, Phys. Rev. B 72 (2005) 224401.

[4] Z.Cheng, X. Wang, S. Duo, Phys. Rev. B 77 (2008) 092101.

[5] Sosnowska, N.T. Peterlin, E. Steichele, J. Phys C: Solid State Phys. 15, 4835 (1982).

[6] F. Bai, J. L. Wang, M. Wuttig, J. F. Li, N. G. Wang, A. P. Pyatakov, A. K. Zvezdin, L. E. Cross, D. Viehland, Appl. Phys. Lett. 86, 032511 (2005).

[7] J. Wang, H. Zheng, V. Nagarajan, B. Liu, S. B. Ogale, D. Viehland, V. Venugopalan, D.G. Schlom, M.Wutting, R. Ramesh, J.B.Neaton, U.V. Waghmare, N. A. Hill, and K.M. Rabe, Science 299, 1719 (2003).

[8] Chia-Ching Lee and Jenn-Ming Wu, Appl. Phys. Lett. 91, 102906 (2007).

[9] Glenda Biasotto, Francisco Moura, Cesar Foschini, Elson Longo, Jose A. Varela, Alexandre and Z. Simes, Processing and Application of Ceramics 5, 3139 (2011).

[10] Z. H. Chen, L. You, C. W. Huang, Y. J. Qi, J. L. Wang, T. Sritharan, and L. Chen, Appl. Phys. Lett. 96, 252903 (2010).

[11] D. Mazumdar, V. Shelke, M. Iliev, S. Jesse, A. Kumar, S. V. Kalinin, A. P. Baddorf, and A. Gupta, Nano Lett. 10, 2555 (2010).

[12] Meiya Li, Min Ning, Yungui Ma, QibinWu and C K Ong, J. Phys. D: Appl. Phys. 40, 16031607 (2007).

[13] M. Okuyama, Y. Ishibashi, Ferroelectric Thin Films, Topics Appl. Phys. 98, 59-75 (2005).

[14] B Bhushan, A Basumallick, S K Bandopadhyay, N Y Vasanthacharya and D Das, J. Phys. D: Appl. Phys. 42, 065004 (2009).

[15] Y. H. Lin, Q. H. Jiang, Y. Wang, C.W. Nan, L. Chen, J. Yu, Appl. Phys. Lett. 90, 172507 (2007).

[16] Yu.I. Golovko, V.M. Mukhortov, O.A. Bunina, I.N. Zakharchenko, A.S. Anokhin, V.B. Shirokov, Yu.I. Yuzyuk, Physics of the Solid State 7, 1432 (2010).

[17] Massimiliano Stengel & Nicola A. Spaldin, Nature Lett. 443, 679-682 (2006).

[18] L. J. Sinnamon, M. M. Saad, R. M. Bowman, and J. M. Gregg, Appl. Phys. Lett. 81, 703-705 (2002).

[19] Y. Chen, X. Y. Zhang, C. Vittoria, and V. G. Harris, Appl. Phys. Lett. 94, 102906 (2009).

[20] F. Huang, X. Lu, Weiwei Lin, Yi Kan, J. Zhang, Q. Chen, Zhe Wang, Liben Li and J. Zhu, Appl. Phys. Lett. 90 (2010) 222901.

[21] Néel, L. Compt. Rend. 252, 4075-4080 (1961).

[22] Néel, L. Compt. Rend. 252, 9-12 (1961).

[23] J. T. Richardson, D. I. Yiagas, B. Turk, K. Forster and M. V. Twigg J. Appl. Phys. 70 6977 (1991).

[24] C. Ederer and N. A. Spaldin, Phys. Rev. B 71, 060401(R) (2005).

[25] Y. Wang, Y. H. Lin, C. W. Nan, J. Appl. Phys. 104, 123912 (2008).

[26] D. S. Rana, K. Takahashi, K. R. Mavani, I. Kawayama, H. Murakami, M. Tonouchi, T. Yanagida, H. Tanaka, and T. Kawai, Phys. Rev. B 75, 060405 (2007).

[27] J. Wang, A. Scholl, H. Zheng, S. B. Ogale, D. Viehland, D. G. Schlom, N. A. Spaldin, K. M. Rabe, M. Wuttig, L. Mohaddes, J. Neaton, U. Waghmare, T. Zhao, and R. Ramesh, Science 307, 1203 (2005).

[28] F. Huang, X. Lu, Weiwei Lin, X. Wu, Yi Kan, and J. Zhu, Appl. Phys. Lett. 89, 242914 (2006).

[29] Sujoy Roy, Igor Dubenko, Dossah D. Edorh, and Naushad Ali, J. Appl. Phys. 96, 1202 (2004).

[30] S. Lamba, S. Annapoorni, Eur. Phys. J. B 39, 19-25 (2004).

5 $BiFeO_3$ nanowires and nanotubes: an advance multiferroic oxide material

Recent approaches have focused on developing one-dimensional nanostructures such as nanowires, nanofibers and nanotubes mainly due to their relevant applications in mesoscopic physics, strong size dependent effect and nanoscale device fabrication such as magnetic memory devices and sensors. As the magnetic and ferroelectric properties of $BiFeO_3$ (BFO) are dependent on structure and size, BFO nanowires (NWs)/nanotubes (NTs) could be ideal choice to tailor the magnetic ordering and electrical properties [1, 2, 3, 4]. The high aspect ratio NTs having large surface to volume ratios are morphologically more advantageous than other nanostructures in order to obtain long range magnetic ordering. In this chapter, the effect of the Pr and Cr doping and Pr-Cr co-doping on the multiferroic properties of BFO NWs and NTs is discussed. Studies on Pr-Cr co-doped BFO Nws/NTs have not been reported yet to the best of our knowledge. We have prepared doped NWs and NTs with compositions $Bi_{0.9}Pr_{0.1}FeO_3$, $BiFe_{0.9}Cr_{0.1}O_3$ and $Bi_{0.9}Pr_{0.1}Fe_{0.9}Cr_{0.1}O_3$ (henceforth written as $Pr_{0.1}$BFO, $Cr_{0.1}$BFO

and $Pr_{0.1}Cr_{0.1}$BFO, respectively). The co-doped BFO NWs and NTs has been found to exhibit enhanced ferroelectric property and magnetic ordering at room temperature (RT) due to the reduction of oxygen vacancies and for the broken spiral spins structure. Significant improvement in the magnetoelectric response in the co-doped BFO NTs is also observed. Anomalous photovoltaic effects and switchable photovoltage generation in the NTs are also studied. We have investigated the diameter dependent optical and magnetic properties of the Pr-Cr co- doped BFO NWs. Blue shift of the band edge emission is observed in the Pr-Cr co-doped BFO NWs due to quantum confinement effect. A giant increase in the magnetization is demonstrated by modifying the NWs diameter.

5.1 Magnetic, Ferroelectric and Magnetoelectric properties of undoped and doped $BiFeO_3$ nanotubes

5.1.1 Background

The enhancement of the multiferroic properties in BFO thinfilms doped with Pr and La have been reported, where the improvement of the ferromagnetic and ferroelectric properties are attributed to the structural deformations or modifications induced by the high valance Pr/La ion substitution and reduction of the oxygen vacancies with the Pr ion substitution for Bi, respectively [5, 6, 7, 8]. The transition metal ions such as Cr^{+3} and Mn^{+3} doped BFO thin films and nanostructures provide better ferroelectric properties due to the enhancement of the resistance caused by the better electrical stability of the dopent ions [1, 9, 10]. Lower leakage current along with the enhanced saturation magnetization is also reported in Cr doped BFO thin films and nanostructures [1, 9, 10, 11].

In this regard, considering the continuous search for the multiferroic materials for

their multifunctional applications and interesting physics, in the present work, we report the fabrication of the arrays of Pr and Cr doped and Pr-Cr co-doped BFO NTs via an easy wet chemical liquid phase deposition (LPD) template assisted route and the study of their structural, ferroelectric, magnetoelectric and magnetic properties. Here we used AAO template assisted route which is the most widely used method for the fabrication of NWs and NTs compared to other template approaches such as nuclear track-etched polycarbonate membranes, nanochannel array glasses, mesoporous channel hosts etc. It allows the synthesis of NWs ranging in size from less than 20 nm to greater than 200 nm. NWs is synthesized using AAO template with pore diameter less than ∼250 nm. NTs is synthesized in AAO template having 250 nm pore diameter. There are limited reports on the studies of the doped BFO nanostructures.

5.1.2 Results and Discussion

5.1.2.1 Morphology and Crystal structure of $Bi_{1-x}Pr_xFe_{1-x}Cr_xO_3$ nanotubes

Figure 5.1(a) shows the SEM micrograph of the Pr and Cr co-doped BFO ($Pr_{0.1}Cr_{0.1}BFO$) NTs released from the pores of AAO by dissolving the template in 2 M NaOH solution. It is evident from the figure that the outer surface wall of the NTs is very smooth. It is found that all the NTs have very similar average length (∼4-5 μm) and uniform outer diameter (∼250 nm) and tube wall thickness of about ∼50 nm. The aspect ratios of the NTs are in the range of 16-20. EDAX spectra analysis of the co-doped BFO NTs (Fig 5.1(b)) conducted to study their chemical composition clearly confirms the presence of Bi, Fe, Pr, Cr and O in the NTs, where the atomic ratio of Bi : Fe and Pr : Cr are close to 1 : 1, for spectrum taken from different positions of the NTs. For a better understanding of the microstructure and topography, HRTEM analysis of the NTs released from the AAO template is conducted. Figure 5.1(c) shows the representative TEM image

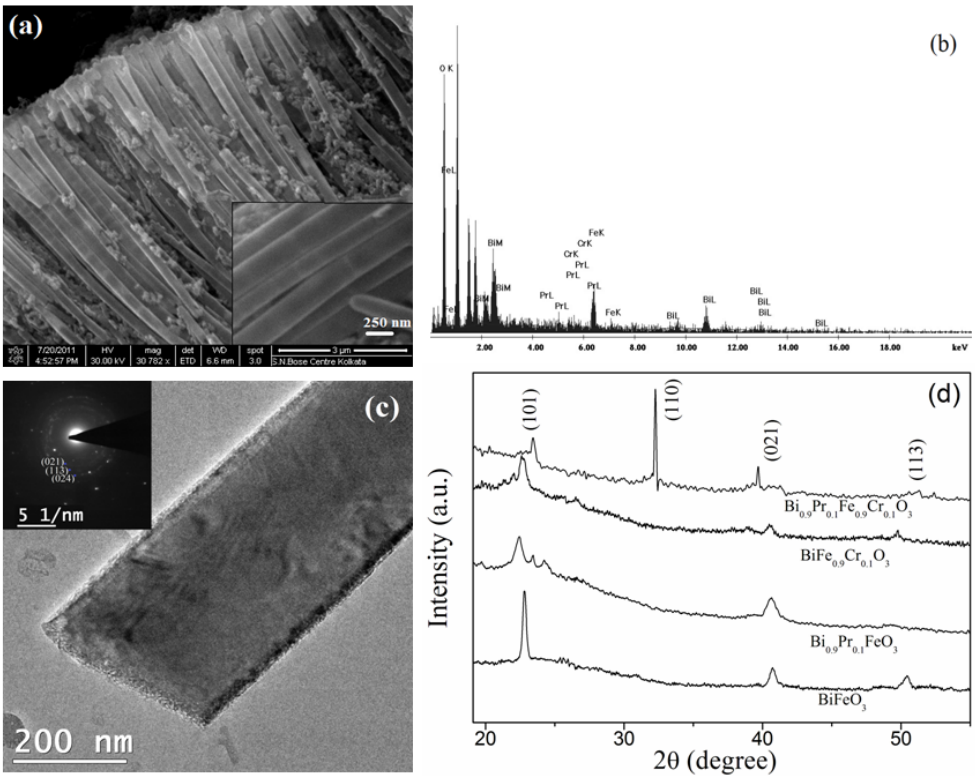

Figure 5.1: (a) SEM image of the $Pr_{0.1}Cr_{0.1}$BFO NTs. Inset of (a) shows the high magnification SEM image of the same NTs. (b) EDAX spectra and (c) TEM micrograph of the of the $Pr_{0.1}Cr_{0.1}$BFO NTs. Inset of (c) shows the SAED pattern of the same NTs. (d) XRD pattern of the undoped and doped BFO NTs.

of the $Pr_{0.1}Cr_{0.1}$BFO NTs of ∼250 nm outer diameter. The inset of Fig 5.1(c) shows the selected area electron diffraction (SAED) pattern of the NTs, which clearly indicates the polycrystalline nature of the NTs. Three major bright diffraction rings in the SADE pattern correspond to the (021), (113) and (024) crystallographic planes of the co-doped BFO NTs. The XRD patterns of the undoped and doped BFO NTs are shown in Fig 5.1(d). The rhombohedral structure of the undoped and doped BFO NTs with R-3m space group is evident from the XRD pattern. The XRD pattern of the undoped BFO NTs shows no considerable impurity peaks, which confirms the formation of single phase BFO NTs.

5.1.2.2 Ferroelectric properties of $Bi_{1-x}Pr_xFe_{1-x}Cr_xO_3$ nanotubes

The nature of the inherent electrical polarization of the undoped and doped BFO NTs is investigated by the *P-E* hysteresis loop measurements. Figure 5.2(a) shows the RT *P-E* hysteresis loops of the single doped and co-doped BFO NTs at the frequency of 50 Hz and a maximum field of ±80 kV cm^{-1}. In general, undoped BFO ceramics exhibits weak ferroelectric properties due to its leakage current problem, [12, 13]. But, in our experiment undoped BFO NTs exhibits no *P-E* hysteresis loop hence, no ferroelectric characteristics. However, it is expected that with suitable doping better ferroelectric properties could be achieved in BFO. In this work, the *P-E* hysteresis loops for all the doped BFO NTs are not saturated under the application of the voltage as high as ±80 kV, which indicates that much higher electric field is required for saturation. The application of higher field is not possible in our experiment due to the limitation of the instrument. Here, all doped BFO NTs samples exhibit a kind of leaky paraelectric type unsaturated *P-E* hysteresis loop within our measurement limit. Hence, it is difficult to confirm the ferroelectric character of the doped BFO NTs from the *P-E* hysteresis loop measurements only. Obtaining *P-E* hysteresis loops for nanostructures is challenging because of their leakage and low voltage range of dielectric breakdown. The $Cr_{0.1}$BFO NTs show a roundish lossy type *P-E* loop indicating the existence of leakage current in a high electric field region, whereas the $Pr_{0.1}Cr_{0.1}$BFO and $Pr_{0.1}$BFO NTs samples show improved electrical properties with comparatively low leakage current. The co-doped BFO NTs exhibits maximum polarization and lowest electric coercivity among the doped BFO NTs. The values of the remanent polarization (P_r) and the coercive electric field (E_c) of the $Pr_{0.1}Cr_{0.1}$BFO NTs are 0.55 $\mu C/cm^2$ and 6 kV cm^{-1}, respectively. The maximum polarization and E_c values of all the doped BFO NTs are summarized in Table 5.1. However, the reduced leakage conduction in $Pr_{0.1}Cr_{0.1}$BFO NTs permits the

application of a high electric field to the NTs, hence achieving large P_r. It is worth noticed that the value of the E_c is less in case of the $Pr_{0.1}Cr_{0.1}$BFO NTs. This indicates that the oxygen vacancy concentration in the co-doped BFO NTs is expected to reduce considerably as the coercive field in BFO is related to the pinning effects of space charge originated due to the presence of the oxygen vacancies [14]. Therefore, with the reduction of the oxygen vacancies the coercive field will decrease in ferroelectrics.

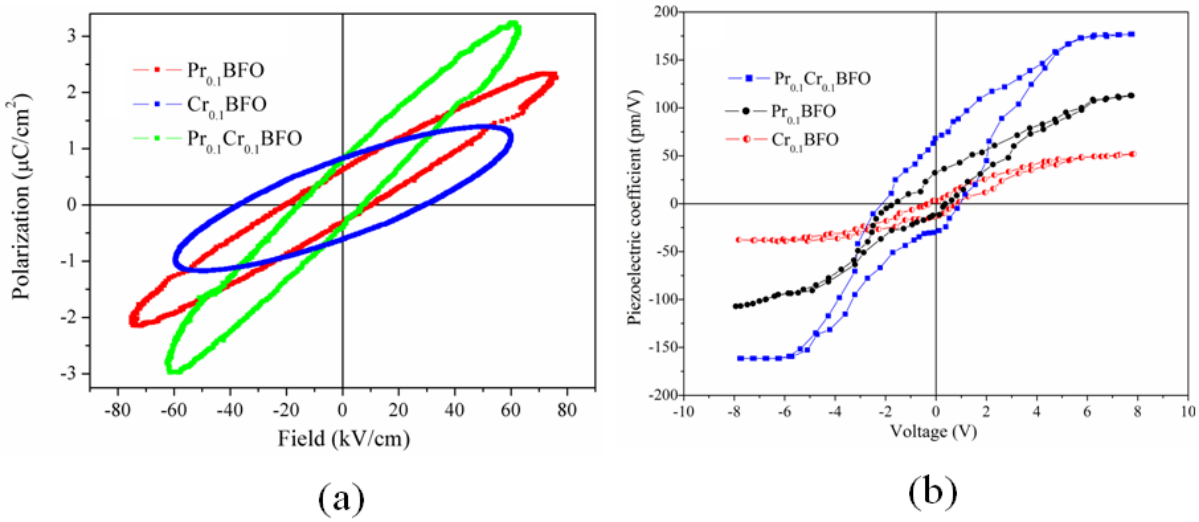

Figure 5.2: (a) Ferroelectric hysteresis loops and (b) the piezoresponse force microscopy (PFM) hysteresis loops of the doped BFO NTs measured at RT.

In general, leakage current in BFO appears due to the presence of oxygen vacancies and Fe^{+2} ions which are the reason behind the weak electric ordering in this material. Volatility of Bi plays a big role in appearance of oxygen vacancy in undoped BFO. Therefore Pr^{+3} doping in place of Bi^{+3} reduces oxygen vacancies in the BFO structure [6]. Furthermore, atomic radius of Pr (1.828 Å) is larger than Bi (1.55 Å), which causes more distortion in oxygen octahedral by relative displacement of the equatorial and apical oxygens in the doped sample. On the other hand, Cr doping in BFO NTs causes less distortion in FeO_6 as the atomic radius of Cr (1.249 Å) is comparable with Fe

(1.24 Å) and therefore Cr doped BFO NTs provide less polarization value compared to Pr doping in BFO NTs at higher field [15]. The high value of polarization in the co-doped NTs samples can occur due to the charge carrier accumulation in the interface of the grain and grain boundaries [16]. To confirm the ferroelectric character of the doped BFO NTs, the NTs are investigated by piezoresponse force microscopy (PFM) in several randomly chosen surface areas of different dimensions. Figure 5.2 (b) shows the PFM hysteresis loops of the doped BFO NTs measured on $1\mu m^2$ surface area using a conductive AFM tip. The observed piezoelectric hysteresis loops confirm the presence of the ferroelectric polarization and hence the ferroelectric character of all the doped BFO NTs [17, 18]. It is evident from Fig 5.2(b) that the co-doped BFO NTs exhibit significantly enhanced PFM hysteresis loop, hence better ferroelectic response. Whereas, the ferroelectric signal from the $Cr_{0.1}$BFO NTs is weakest amongst the NTs. Recently, it has been reported that the BFO nanostructures show ferroelectricity even when the dielectric leakage is present [19]. In our study also, the PFM investigation clearly reveals the ferroelectric behaviour of the doped BFO NTs although, the *P-E* hysteresis loop measurement of the doped BFO NTs signifies the existence of leakage.

5.1.2.3 Dielectric and Magnetodielectric properties of $Bi_{1-x}Pr_xFe_{1-x}Cr_xO_3$ nanotubes

Figure 5.3 shows the dielectric constant (ε) of the arrays of undoped and doped BFO NTs as a function of frequency from 40 Hz to 90 MHz at RT. Fig 5.3 indicates strong frequency dependence in low frequency range, while relaxation of the dipoles is observed in the 100 kHz to 90 MHz frequency range. Inset of Fig 5.3 shows the change of ε at low frequency region. All curves obey the Debye relaxation expression. It is found that the $Pr_{0.1}$BFO NTs exhibits highest value of dielectric constant. The value of ε is found to be almost 3 times higher in $Pr_{0.1}$BFO NTs than that of the undoped BFO NTs at a

Table 5.1: Ferroelectric and magnetic parameters of the undoped and doped BFO NTs at RT.

Sample	Maximum Polarization $\mu C/cm^2$	E_C (kV/cm)	Remanant magnetization (memu/g)	Coercive field Oe	M at at 3 kOe (memu/g)
BFO	–	–	0.37	93	25.1
$Cr_{0.1}$BFO	1.33	33	0.54	23	29.3
$Pr_{0.1}$BFO	2.32	15	2.64	207	38.4
$Pr_{0.1}Cr_{0.1}$BFO	3.19	11	12.58	103	48.7

frequency of 620 Hz.

Since in multiferroics magnetic and electric domains are coupled with each others, electric order parameter of the material can be manipulated by the application of magnetic field and vice versa. The variation of the dielectric constant (ε) with the applied magnetic field is a popular way to check the magnetoelectric coupling of the multiferroics. A material gets strained with the application of a magnetic field. This strain induces stress inside the material and generates an electric field on the ferroelectric domain. Hence, the dielectric behaviour of the material is modified. Figure 5.4 shows the RT magnetic field dependence of the magnetodielectric (MD) effect, expressed by $[\varepsilon_r(H)\text{-}\varepsilon_r(0)]/\varepsilon_r(0)$ at the frequency (f) of 1 kHz for the undoped and doped BFO NTs array. It is clear from Fig 5.4 that the undoped BFO NTs does not show any variation in the MD effect up to the maximum applied field of 6 kOe. For $Cr_{0.1}$BFO NTs there is a change in MD around 5.5 kOe. The $Pr_{0.1}$BFO and co-doped BFO NTs show noticeable increase in MD effect at a lower field (1-2 kOe). It is evident that the co-doped BFO NTs exhibits maximum enhancement in ε value with the applied magnetic field.

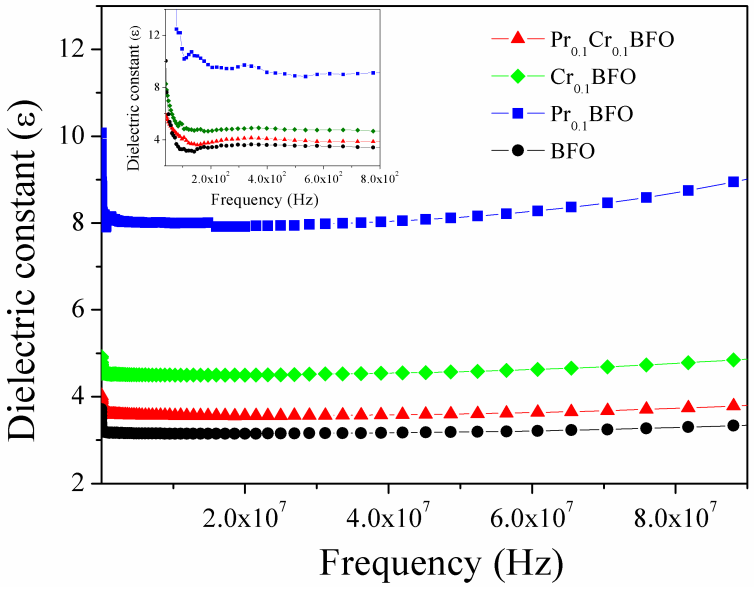

Figure 5.3: Frequency dependence of the dielectric constant (ε) of the undoped and doped BFO NTs at RT. Inset shows the same plot at low frequency region.

Though the value of ε of co-doped BFO NTs is lower than single doped BFO NTs, it shows maximum positive MD effect, which is comparable with the MD value reported in case of Ba doped BFO thin film and other multiferroic materials [13, 20, 21].

5.1.2.4 Magnetic properties of $Bi_{1-x}Pr_xFe_{1-x}Cr_xO_3$ nanotubes

The RT magnetic ordering of the arrays of AAO template embedded undoped and doped BFO NTs are investigated by conducting the magnetic measurements. The RT magnetic hysteresis (M-H) loops of the NTs are shown in Fig 5.5, after subtracting the diamagnetic contribution of the AAO template. Still looking at the M-H plot for the co-doped BFO NTs it seems that the weak FM signal is embedded in a diamagnetic background. Most probably, this diamagnetic response is coming from the diamagnetic sample holder used for SQUID measurement or even from the AAO template itself as a background diamagnetic noise as the effective mass of the NTs is very small compared with that of the template. However, it is evident that the undoped BFO NTs shows

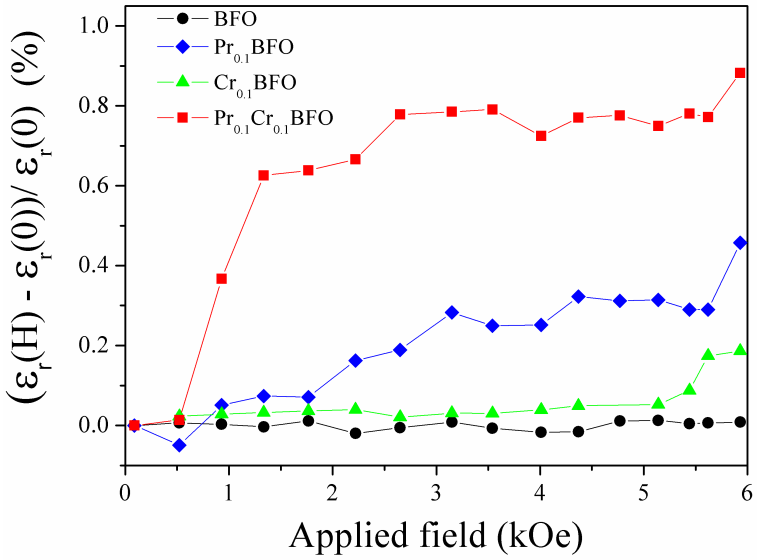

Figure 5.4: Magnetic field-induced change in the dielectric constant (ε) of the undoped and doped BFO NTs measured at frequency (f) of 1 kHz at RT.

very weak ferromagnetic (FM) ordering in RT, whereas, the Cr and Pr single doped BFO NTs also exhibit weak but little enhanced magnetization than the undoped BFO NTs. It is well known that the bulk undoped BFO ceramics show an antiferromagnetic nature at RT because of its complicated cycloidal spin structure with a wavelength of about 62 nm along the $[110]_h$ axis [22]. However, weak FM is reported for BFO thin films, nanoparticles, nanowires and nanorods [1, 3]. In our experiment the wall thickness of the BFO NTs is ∼50 nm, which is less than the wavelength of the corresponding spiral spin structure in BFO. Therefore, the collapse of the spiral spin structure is believed to be the origin of the weak FM signal in the undoped BFO NTs [3]. It is clear from the inset of Fig 5.5 that the NTs shows a shift in the magnetization curve. This phenomenon mainly occurs due to the exchange bias effect between the FM and AFM phase in the samples.

It is evident from the magnetization curve that the $Pr_{0.1}$BFO NTs shows little enhanced magnetization than the $Cr_{0.1}$BFO NTs (Table 5.1). Only the $Pr_{0.1}Cr_{0.1}$BFO NTs

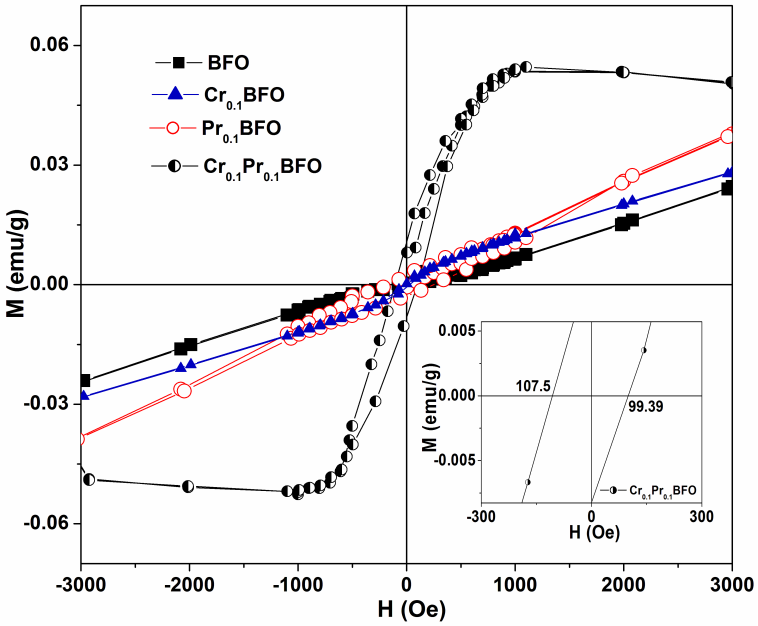

Figure 5.5: Field dependence of magnetization over ±3 kOe at RT (300 K) for the undoped and doped BFO NTs.

exhibits enhanced FM ordering with saturation near 1 kOe. Highest magnetic properties are also observed in the $Pr_{0.1}Cr_{0.1}$BFO NTs with the saturation magnetization (M_s), remanant magnetization (M_R) and coercive field (H_c) values of 0.049 emu/g, 0.012 emu/g and 103.3 Oe, respectively. The values of the different magnetic parameters for different NTs are summarized in Table 5.1. The increase in magnetic response in bulk Cr-doped BFO and Pr-doped BFO ceramics have been reported earlier [6, 23]. It is believed that the suppression of spiral spin structure induced by the substitution of the Pr atom in A site in Pr-doped BFO [6] as well as the strong superexchange coupling interaction between the Fe^{+3} and Cr^{+3} in the Cr-doped BFO [23] are playing the key role behind the enhancement of the magnetization in doped BFO ceramics. Herein, the huge increase in the magnetization of the arrays of co-doped BFO NTs is attributed to the change in canting angle [24] or the spiral spin modulation in the BFO nanostructures along with coupling interaction between the Fe^{+3} and Cr^{+3} ions in doped BFO due to the co-doping

both at the A and B sites.

5.2 Effect of metal-doping on highly efficient photovoltaics and switchable photovoltage in $BiFeO_3$ nanotubes

5.2.1 Background

$BiFeO_3$ (BFO), well known for its remarkable intrinsic multiferroic properties is considered as a perspective candidate for applications in memory, actuators, transducers, spintronic and logic devices [25, 26, 27]. Recently, the anomalous photovoltaic (PV) effect is reported in the thin films and bulk BFO single crystals with favourable band-gap energy (∼2.74 eV) compared to other ferroelectric oxides [28, 29, 30, 31]. The bulk photovoltaic effects observed in semiconductor ferroelectric (SF) materials have some different charge separation mechanism in comparison to the conventional junction-based interfacial PV devices. In SFs the photo-generated charge carriers of both polarities are separated and driven toward the respective electrodes due to the polarization-induced internal electric field within the material. This unique PV effect in SF materials opens the new possibility for optoelectronics, solar energy harvesting and optical information storage applications [32, 33, 34, 35]. In this regard, the study of the PV effect in BFO is very exciting considering its multifunctional applications and continues search for the new PV materials for green energy. Diode like unidirectional electric current flow and photovoltages several times higher than the band-gap energy is reported in BFO [29, 30, 31]. Here, we investigate the PV properties of the undoped and doped polycrystalline BFO NTs. In our recent work [36], discussed in the previous section, we have found that Pr, Cr

and Pr-Cr co-doped BFO NTs exhibit enhanced multiferroic properties compared to the undoped BFO NTs. In this regard, herein, we study the unknown PV property of the undoped BFO NTs and also the effect of Pr and Cr-doping on its PV effect considering its versatile applications. The PV properties of the BFO nanostructures have not been examined yet in details. Doping of metal ions into semiconductors can tailor the PV properties by changing the position of the conduction bands and defect levels within it. Here, we observe significant changes of the open-circuit voltage (V_{oc}) and short- circuit current density (J_{sc}) as a result of metal-doping in BFO NTs both under dark and light illumination. The role of doping on the parameters like power conversion efficiency (η) and fill factor (FF) of the NTs are also studied. The value of η is found to enhance by several orders of magnitude compare to the bulk BFO heterostructures. The role of metal-doping on tuning of photocurrent in the NTs upon illumination is also examined.

5.2.2 Results and Discussion

5.2.2.1 Current-voltage (I-V) characteristics of $Bi_{1-x}Pr_xFe_{1-x}Cr_xO_3$ nanotubes

The dark and illuminated current-voltage ($I-V$) curves for the undoped and doped BFO NTs measured at room temperature are shown in Fig 5.6 (a) and (b), respectively. All the NTs show a typical PV effect with good response to the incident photons. The photocurrent is significantly increased under illumination and becomes positive at zero bias. For a better understanding of the change in PV effect under light-illumination the $I-V$ plot of the Ag/ BFO NTs/Ag structure is shown in the inset of Fig 5.6(b). The change of V_{oc}, the voltage at which the current becomes zero, for all the NTs under illumination is plotted in Fig 5.6(c). Similarly, the change of the short-circuit current (I_{sc}), determined as the current at zero bias, for the NTs under illumination is shown in Fig 5.6(d).

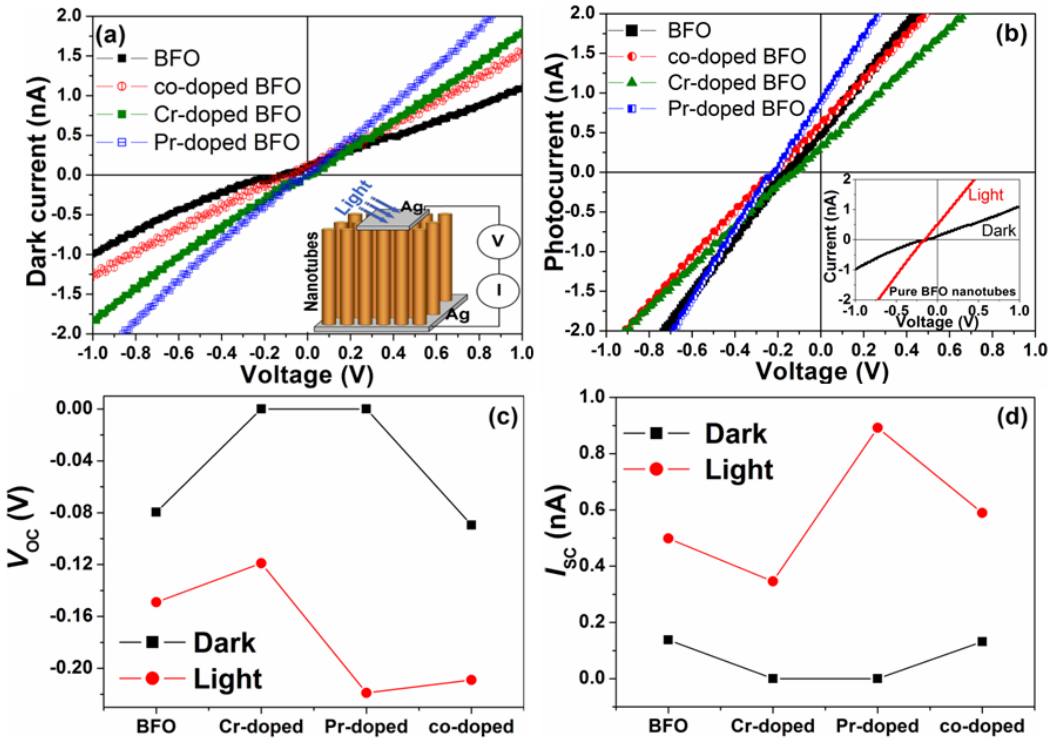

Figure 5.6: (a) Dark current-voltage and (b) photocurrent-voltage characteristics of the undoped and doped BFO NTs. Inset of (a) shows the measurement setup schematically. Inset of (b) shows the current-voltage characteristics of undoped BFO NTs under dark and illuminated condition. The change in V_{oc} (c) and I_{sc} (d) of the NTs with metal-doping under white-light illumination.

It is evident from Fig 5.6 (c) and (d) that the doping of Pr and Cr in BFO NTs have changed the values of V_{oc} and I_{sc} significantly both in dark and illuminated conditions. At dark condition the value of V_{oc} for undoped and Pr-Cr co-doped BFO NTs are -0.075 and -0.089 V, respectively, whereas the V_{oc} for the singly-doped BFO NTs are zero. On the other hand, the values of I_{sc} for undoped and Pr-Cr co-doped BFO NTs are 0.11 and 0.09 nA, respectively at dark. The singly-doped BFO NTs provide no I_{sc} under dark condition. Pr-doped BFO NTs shows highest values of I_{sc} and V_{oc} of about 0.89 nA and -0.21 V, respectively under light-illumination. Under light-illumination the Cr-doped BFO NTs provide the weakest photoresponse having lowest I_{sc} and V_{oc} values

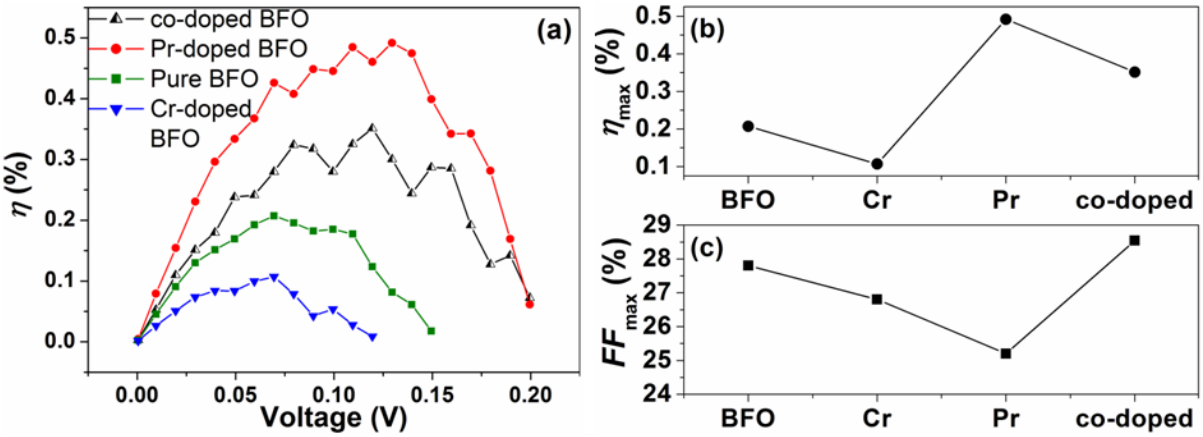

Figure 5.7: (a) Light-to-electricity power conversion efficiency (η) as a function of the terminal voltages for different NTs. Change of (b) η_{max} and (c) fill factor (FF) for different NTs with metal-doping

among all the NTs samples. This is most probably because of the enhanced electrical resistance due to Cr-doping [37]. However, significant increase in the values of V_{oc} and I_{sc} is observed by applying the standard solar white-light illumination of average power 10 mW/cm^2 (AM 1.5) to all the NTs. Hence, it is expected that we can achieve different values for V_{oc} and I_{sc} by changing the intensity of the incident photons as the PV effects in FSs is related to the light-induced carrier generation and carrier separation under the internal electric field [38, 39]. The change of the PV effect in the BFO NTs with metal-doping is because of the incorporation of the defect levels in the optical band-gap [40] which could provide paths for electron recombination or improved electron transport, leading to change in photocurrent [41]. The change of electron mobility (also V_{oc} and I_{sc}) as a result of metal-doping is related to the concentration of defect level which is entirely dependent upon the type of metal ions and doping concentration [41] although, the variation of defect levels with Pr/Cr doping in BFO is yet not studied properly. Furthermore, BFO NTs having high surface-to-volume ratio, the surface charge density is found to increase compared with bulk because of the surface phase transition [42, 43].

Hence, more expectedly the doping of metal ions in BFO NTs might further tailor the surface phases in BFO leading to a significant change in their photovoltaic response.

The light-to-current power conversion efficiency (η) of the NTs can be calculated as $\eta = P_{out}/P_{in}$, where P_{out} is the photovoltaic output power density and the input power density, P_{in} is the radiation intensity (mW/cm^2) received over the electrode surface at a certain point of the $J-V$ plot. The maximum value of η is calculated by determining the maximum output electrical power, $P_{out}^{max} = J_{sc} \times V_{oc}$. The variation of the calculated values of η at different points of the $J-V$ plot as a function of voltage (V) for the NTs are plotted in Fig 5.7(a). The value of η is found to change significantly upon doping. The η is found to be maximum for the Pr-doped BFO NTs and minimum for the Cr-doped BFO NTs. The quantum efficiency of Pr-Cr co-doped BFO NTs is in between undoped and Pr-doped BFO NTs. The change in the value of η_{max} with metal-doping in BFO NTs is shown in Fig 5.7(b). The values of η_{max} for undoped, Pr and Cr-doped BFO NTs are 0.207, 0.50 and 0.106 %, respectively. It is evident that the value of η increases with Pr-doping in BFO NTs, whereas, with Cr-doping the value of η is reduced. However, it is important to notice that the values of η for undoped and doped BFO NTs are found to be enhanced by several orders of magnitude than the theoretically predicted limit (10^{-6}-10^{-7}) of the power conversion efficiency for FSs. The value of η is also higher compare to the previously reported experimental values of different BFO heterojunctions: like BFO/$NbSrTiO_3$ ($\sim 3\times10^{-2}$ %) [44] and graphene/polycrystalline BFO/Pt heterojunctions (2.5×10^{-3} %) [45], the preferentially oriented BFO (001) thin films ($\sim 7\times10^{-2}$ % and $\sim 7\times10^{-4}$ %) [46, 39], single crystal BFO palate ($\sim 3\times10^{-3}$ %) [37], ITO/polycrystalline BFO thin films/Pt capacitor ($\sim$0.125 %) [38] and the other oriented ferroelectric thin films [47, 48]. Another important parameter for PV devices known as FF which is related to η as,

$$FF = \eta P_{in}/V_{oc} \times J_{sc} = P_{out}^{max}/V_{oc} \times J_{sc} = J_{max} \times V_{max}/V_{oc} \times J_{sc}$$

is also calculated for different NTs. The values of FF_{max} calculated using η_{max} values for the sets of NTs are plotted in Fig 5.7(c). For the singly-doped NTs the FF values are found to reduce. FF is found to decrease noticeably in Pr-doped BFO NTs but increases a little in the co-doped sample compare to undoped BFO. The significant increase of η value in the undoped BFO NTs over the bulk BFO is because of the particular nanoscale dimensional morphology of the NTs under the Ag electrode which can produce large number of photoexcited carriers under illumination and hence large photocurrent to exhibit enhanced light-to-electricity power conversion efficiency. The change in the values of η upon metal-doping can be explained based on the change in the concentration and mobility of the photogenerated non-equilibrium carriers in the NTs because of the incorporation of the dopant ions.

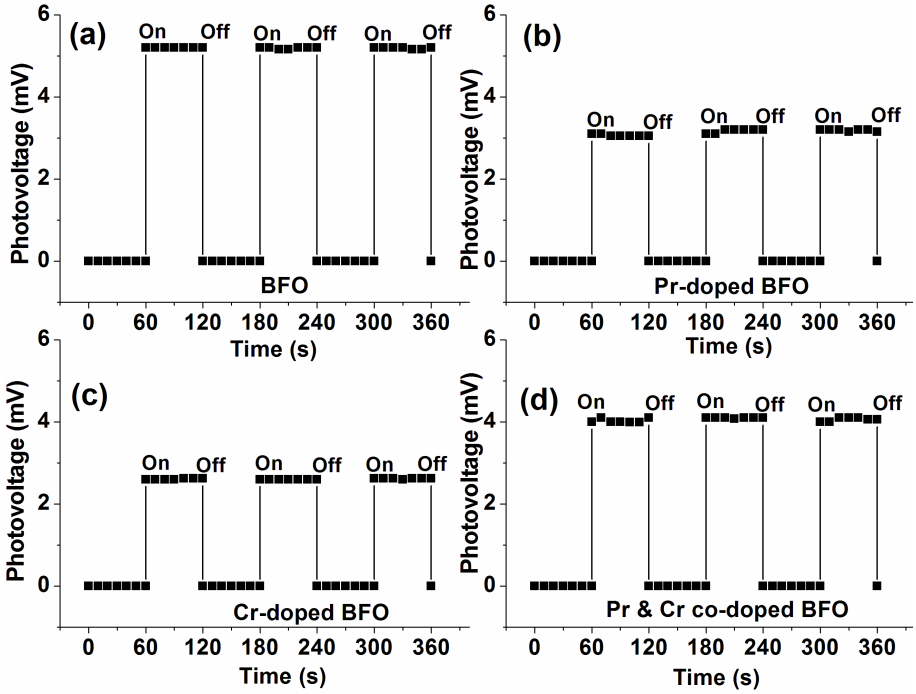

Figure 5.8: The zero-bias photovoltage of the NTs as a function of time with incident light intensity of 10 mW/cm^2

5.2.2.2 Switchable photovoltage in $Bi_{1-x}Pr_xFe_{1-x}Cr_xO_3$ nanotubes

The generation of photovoltage/photocurrent by light-illumination is observed for all the NTs. Fig 5.8 (a)-(d) shows the time dependence of the open-circuit photovoltage measured on the undoped and doped BFO NTs by illumination with a AM 1.5 white-light. All the NTs exhibit instantaneous response to the incident photons by showing a repeatable and stable On/Off states of the photovoltage, which clearly indicates the production and polarization-induced separation of the photogenerated charge carriers in the material. Interestingly metal-doping also has important influence in the photovoltage production. The open-circuit photovoltage is found to be highest for the undoped BFO NTs and it decreases upon Cr and Pr-doping. The switchable photovolatge in the undoped and doped BFO NTs makes them possible material for the potential photosensitive resistor application.

5.3 Diameter dependent Optical, Magnetic and Dielectric properties of $Bi_{0.9}Pr_{0.1}Fe_{0.9}Cr_{0.1}O_3$ nanowires

5.3.1 Background

Recently, it is found that the size effect has very strong influence specially on the magnetic behavior of $BiFeO_3$ (BFO), which exhibits weak room temperature ferromagnetism (RTFM) in nanometer scale dimension [1, 12]. The improvement of the ferroelectric and magnetoelectric properties is also reported in BFO nanostructures [49, 50]. In previous section, we have demonstrated the enhanced multiferroic performance of the Pr-Cr co-doped BFO NTs [36], where significant improvement of the RTFM is observed. Fur-

thermore, we also have evidenced substantial visible-light photovoltaic effect in BFO NTs [51]. Bulk BFO is a semiconductor ferroelectric material with the direct band gap energy of 2.7 eV [52] exhibiting diode-like characteristics. Therefore, considering the multifunctionality in semiconductor ferroelectric BFO, great interest has been focused in the fabrication of the BFO based novel optoelectronic devices having good carrier transport and large absorption of visible light. Recently, optical properties of the BFO thin films are studied [52, 53] but the optical properties of BFO NWs and NTs are still unknown. Furthermore, the tuning of the RTFM in BFO nanostructures seems to be very exciting as well as challenging too for their successful application in magnetoelectric devices. In this present work, we investigate the diameter (18, 35, 55, 100, 150 and 200 nm) dependent optical, magnetic and magnetodielectric properties of the $Bi_{0.9}Pr_{0.1}Fe_{0.9}Cr_{0.1}O_3$ ($Pr_{0.1}Cr_{0.1}$BFO) NWs grown via wet chemical template assisted route. The effect of quantum confinement on the optical, magnetic and magnetoelectric properties of the co-doped BFO NWs have been demonstrated. Co-doped BFO NWs are found to exhibit enhanced multiferroic properties, recently [36]. The 1D nanostructures having large surface to volume ratios are morphologically more advantageous in order to obtain long range magnetic ordering as well as they are interesting too considering their optical properties. Blue shift of the band edge emission is observed in the Pr-Cr co-doped BFO NWs due to quantum confinement effect. A giant increase of the magnetization is demonstrated for the NWs by modifying the diameter of the NWs.

5.3.2 Results and Discussion

5.3.2.1 Morphology and structural analysis of $Bi_{0.9}Pr_{0.1}Fe_{0.9}Cr_{0.1}O_3$ nanowires

Fig 5.9 (a) and (b) presents the TEM image of a single $Pr_{0.1}Cr_{0.1}$BFO NWs with diameter 100 and 18 nm, respectively. Fig 5.9(c) shows the TEM image of bunch of NWs (diameter

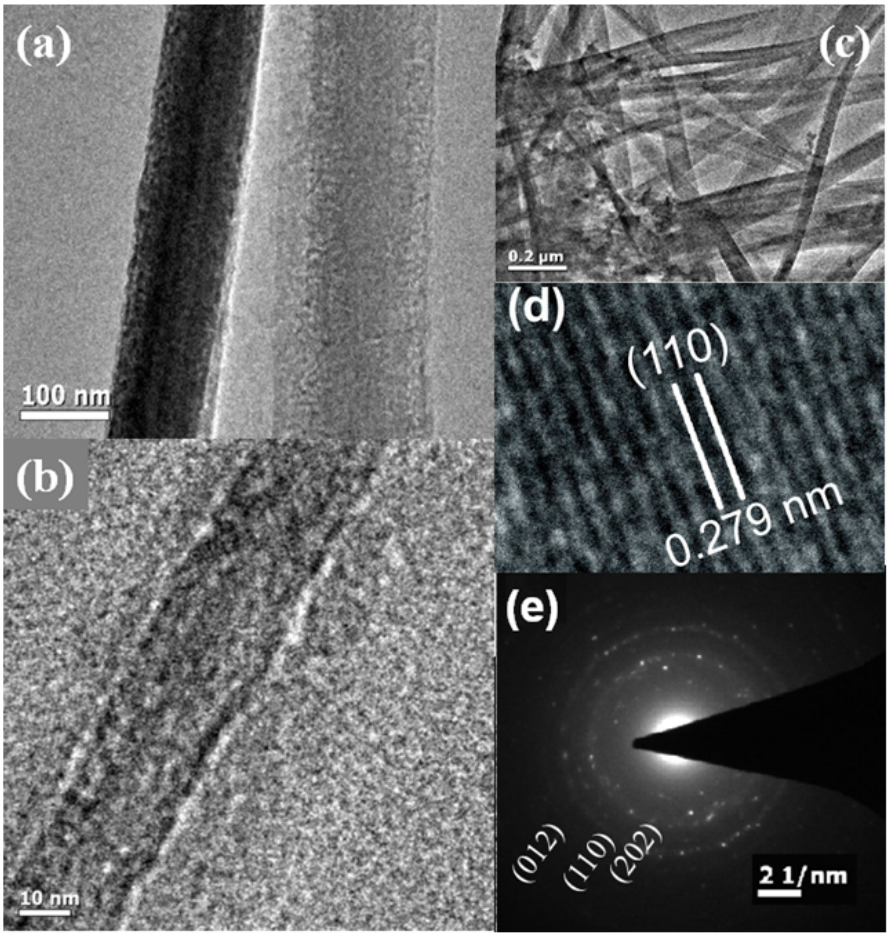

Figure 5.9: (a)-(c) TEM micrographs of the different diameter Pr-Cr co-doped BFO NWs. (d) HRTEM image and (e) the SAED pattern of the Pr-Cr co-doped BFO NWs.

55 nm) with uniform outer surface. HRTEM image (Fig 5.9(d)) shows the polycrystalline nature of the NWs. HRTEM image shows that the d-spacings of 0.279 nm are consistent with the d-values of (110) lattice planes of BFO. Major bright diffraction rings in the selective area electron diffraction (SAED) pattern (Fig 5.9(e)) corresponds to the (012), (110), and (202) crystallographic planes of the co-doped BFO NWs with d-spacing of 2.81, 2.79 and 1.98 Å. All these observations confirm that the co-doped BFO NWs are well crystallized with a single-phase rhombohedral perovskite structure with R3m space group.

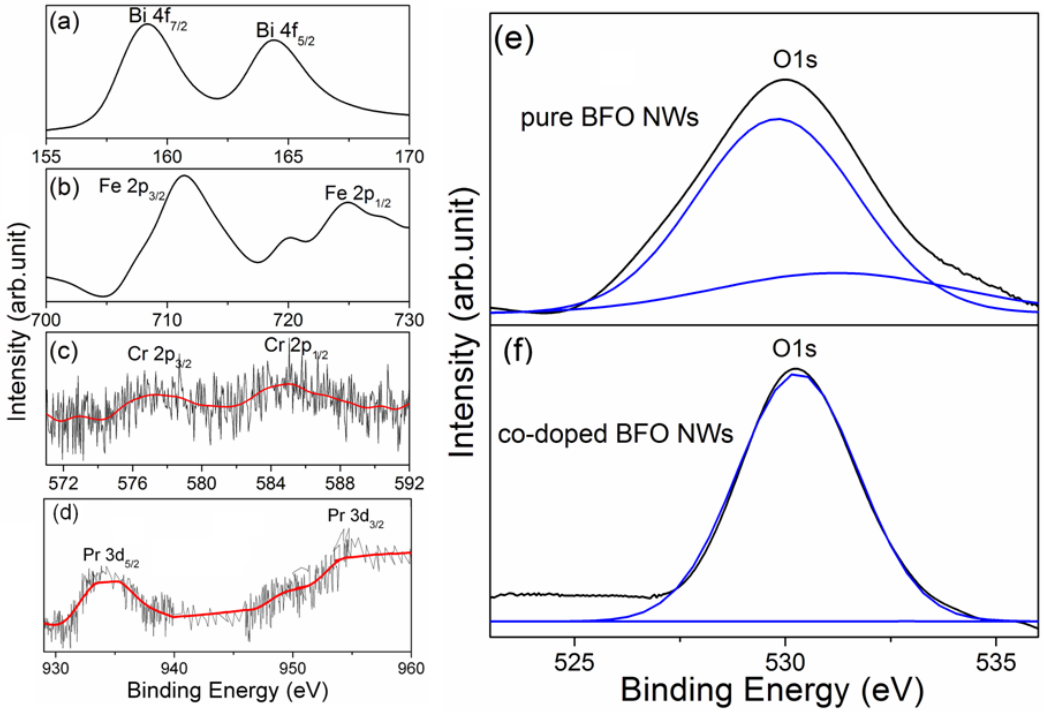

Figure 5.10: XPS spectra for (a) Bi 4f, (b) Fe 2p, (c) Cr 2p and (d) Pr 3d core level of the co-doped BFO NWs. XPS spectra for O 1s core level of (e) undoped BFO and (f) co-doped BFO NWs.

The XPS studies for the undoped and doped BFO NWs are conducted to achieve information about the chemical state and elemental composition. Figure 5.10(a) shows the representative XPS spectra of Bi 4f orbital for the doped BFO NWs. The peaks located at binding energies of 159.0 and 164.3 eV correspond to the Bi $4f_{7/2}$ and Bi $4f_{5/2}$ orbitals, respectively. The doublet peaks of the Bi 4f spectrum clearly suggest the trivalent oxidation state of Bi without the presence of any metallic Bi in the matrix [54, 55]. The representative high-resolution XPS spectrum of the Fe 2p orbital in the co-doped BFO NWs is shown in Fig 5.10(b). The Fe $2p_{3/2}$ and Fe $2p_{1/2}$ peaks located at 711.2 and 724.7 eV, respectively and the tiny peak appears at 719.3 eV corresponds to the satellite peak of Fe^{+3} oxidation state of iron in BFO [55, 56]. Here, no apparent Fe^{+2} related peak (708.2 eV) is observed, hence it is expected that Fe is in 3+ valance state in

the BFO NWs [37, 54]. The chemical state of the dopant elements is also investigated by XPS. The Cr 2p core level spectrum is shown in Fig 5.10(c). The doublet peaks for Cr $2p_{3/2}$ and $2p_{1/2}$ appears at 577.1 and 585.6 eV, respectively, indicate that the doped Cr ion is in trivalent oxidation state where no metallic Cr is present in the doped BFO NWs [57, 58]. This also signifies that the doped Cr ions substitute the Fe site in the BFO NWs. Figure 5.10(d) shows the Pr 3d core level spectrum, where the doublet peaks for Pr $3d_{5/2}$ and $3d_{3/2}$ appears at 933.5 and 954.2 eV, respectively, indicate that the doped Pr ion is in trivalent oxidation state [59, 60]. Furthermore, the information about the presence of oxygen vacancy related defects in the BFO NWs can also be obtained from the XPS studies. The O 1s core level spectra of the undoped and co-doped BFO NWs are shown in Fig 5.10 (e) and (f), respectively situated close to 530 eV. It is worth noticed that for undoped BFO NWs the O 1s spectrum is broad compared to that of the co-doped BFO. Hence, the broad O 1s curve of the undoped BFO NWs can be fitted with two Gaussian peaks centred at 529.7 and 531.5 eV. The lower binding energy peak (529.8 eV) is ascribed to the O 1s binding energy of the BFO phase [61], while the higher binding energy peak (531.5 eV) is attributed to the deficiency of oxygen in the BFO NWs. In co-doped BFO NWs this O 1s peak becomes much sharper and intense one compared to the undoped BFO NWs and this peak can be fitted with two Gaussian peaks at 530.0 and 531.7 eV, where the close examination indicates that the area covered under the higher binding energy peak is very small. Hence, it is found that the area ratio of the peaks (higher binding energy peak/lower binding energy peak) decreases in the co-doped BFO NWs compare to the undoped BFO NWs. This indicates that the concentration of oxygen vacancy related defects in the undoped BFO NWs is much higher than that of the co-doped BFO NWs [61, 62].

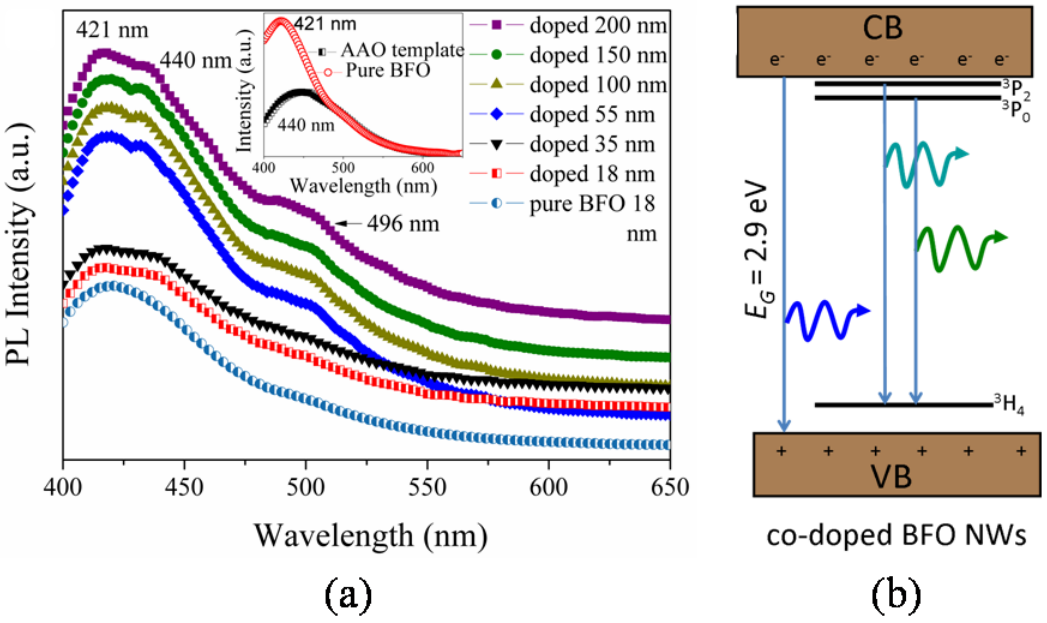

Figure 5.11: (a) Diameter dependent variation of the room-temperature PL spectra of the aligned arrays of template embedded co-doped BFO NWs. Inset of (a) shows the room- temperature PL spectra of the template embedded undoped BFO NWs and the AAO template. (b) Schematic model proposed for the different transitions in the co-doped BFO NWs.

5.3.2.2 Optical properties of $Bi_{0.9}Pr_{0.1}Fe_{0.9}Cr_{0.1}O_3$ nanowires

Photoluminescence spectroscopy

The photoluminescence properties of the different diameter template embedded Pr-Cr co-doped BFO NWs are studied compared to the undoped BFO NWs. Fig 5.11(a) shows the room temperature PL spectra of the different diameter Pr-Cr co-doped BFO NWs samples with respect to the undoped 18 nm BFO NWs, recorded using an excitation of 350 nm light from a Xe lamp source. In the inset of Fig 5.11(a), the PL spectrum of the template embedded undoped BFO NWs are shown compared to the AAO template. AAO template exhibits broad blue emission centred at 440 nm due to the presence of some oxygen vacancy defects [63]. undoped BFO NWs provides strong blue emission

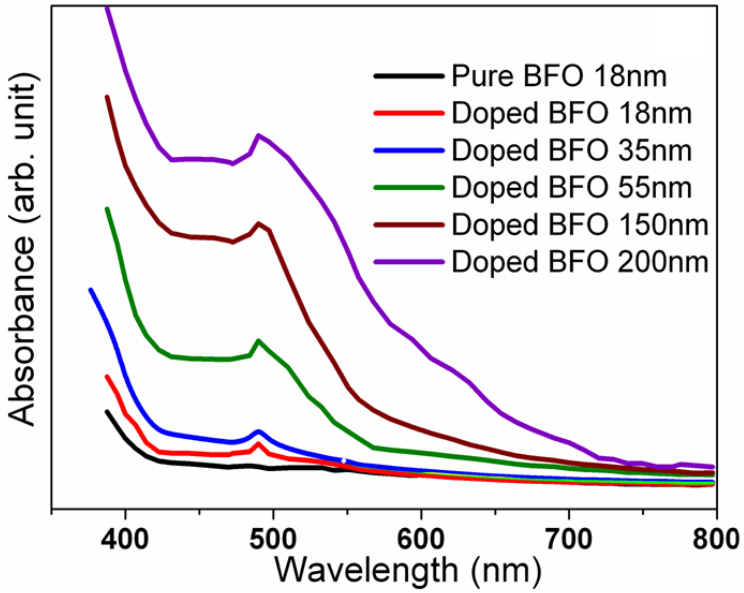

Figure 5.12: Diameter dependent variation of the room-temperature UVvis spectrum of the undoped and co-doped BFO NWs.

peak at 421 nm which is attributed to the band to band electronic transition in BFO NWs. The estimated band gap energy (2.9 eV) for the BFO NWs clearly indicates the blue shift of the band gap emission compared to the reported values (2.7 eV) for the thin films or bulk BFO counterpart [28, 53]. The band gap emission is also observed for all the other doped samples as shown in Fig 5.11(a). For the larger diameter co-doped NWs the band gap emissions becomes more prominent compared to the low diameter NWs. However, the quantum confinement effect observed in all the NWs is most probably because of the polycrystalline nature of BFO NWs, which might contain many crystals of few nm scale dimensions.

All the co-doped NWs exhibit another broad emission band in the visible wavelength region around 490 nm. This blue emission band becomes sharper in case of the large diameter NWs compare with the low diameter NWs. It is worth mentioning that this blue emission is only observed in Pr-doped and Pr-Cr co-doped BFO NWs, hence the

emission band at 490 nm is ascribed to the $^3P_0 \rightarrow {}^3H_4$ transitions of Pr^{+3} ions [64, 65]. In this work, the PL characteristics of the Cr-doped BFO NWs are found to be identical to that of the undoped BFO NWs. Figure 5.11(b) shows the schematic diagram of the PL emission from the co-doped BFO NWs for a better understanding of the light emission mechanism.

UV-vis spectroscopy

Figure 5.12 shows the room temperature UV-vis absorption spectra of the undoped and co-doped BFO NWs. All the NWs samples show a sharp absorption edge at $\sim$ 424 nm, which corresponds to the band to band transition for BFO. The estimated bang gap of BFO (2.9 eV) is in good agreement with the values obtained from the PL investigation. The increase of the band gap energy of the NWs compared with the bulk BFO [53, 28] is because of the quantum confinement effect at nano dimension. The sharpness of the absorption edge corresponds to the band to band transition indicates the good crystalline nature of the undoped and co-doped BFO NWs. For all the doped NWs there is another absorption edge at 492 nm, which is believed to be due to the electronic transitions of Pr^{3+} ions [30,31] as for the undoped BFO NWs there is no absorption edge around 492 nm.

Raman spectroscopy

For further insight on the lattice properties and spin-phonon coupling Raman scattering studies are also carried out on the undoped and co-doped BFO NWs. Figure 5.13(a) shows the comparison of the Raman spectra of the undoped and co-doped BFO NWs at RT by parallel polarization using a laser with an excitation wavelength of 488 cm (LABRAM HR). The shift of the Raman peaks in the co-doped NWs with respect to

Table 5.2: Position of the Raman modes (cm^{-1}) in our study on BFO NWs in comparison with the reported values.

Raman modes	Our work	Fukumura *et al*[66]	Jaiswal *et al*[68]
$A_1 - 1$	124	147	139
$A_1 - 2$	158	176	169
$A_1 - 3$	223	227	216
$A_1 - 4$	409	490	425
E	239	265	260
E	268	279	276
E	313	351	321
E	–	375	348
E	469	437	467
E	533	473	529
E	598	525	598
E	–	77	72
E	109	136	98

the undoped BFO NWs is because of the change in the bond length between the atoms in the BFO crystal due to doping. Here, both the undoped and doped NWs exhibit similar Raman phonon modes, which is quite expected as both the undoped and doped BFO NWs belong to same crystal structure. Figure 5.13(b) shows the Raman spectra of the aligned arrays of the as prepared co-doped BFO NWs with different diameters at RT. Group theoretical analysis predicts 13 (4A1+9E phonon modes) Raman phonon modes are associated with R3c structure of undoped BFO ceramics. All the 13 Raman active phonon modes for bulk BFO ceramics with slight differences in the peak positions due to the changes in oxygen bonding and disorder have also been detected experimentally [66, 67]. Here, the observed natural frequency (cm^{-1}) of each peak position can be assigned as different Raman active modes. Table 5.2 shows the position of the Raman modes of 200 nm undoped BFO NWs and a comparison with the earlier reported data on BFO single crystal and nanoparticles [66, 68].

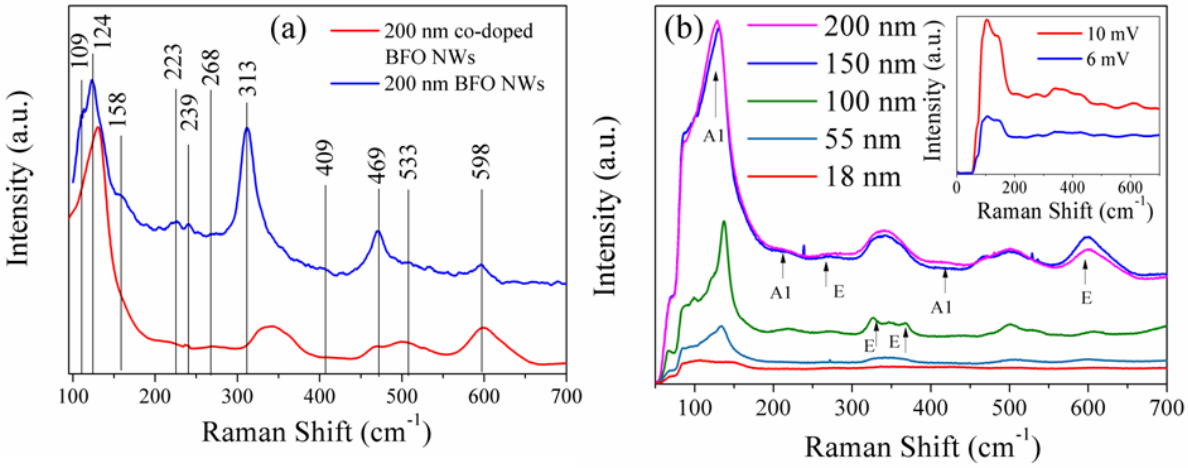

Figure 5.13: (a) Raman spectra of the undoped and co-doped BFO NWs. (b) Diameter dependence of the room-temperature Raman spectra of the co-doped BFO NWs (the asymmetric modes are shown by arrows). Inset of (b) shows the effects of laser power on the Raman spectra of 18 nm co-doped BFO NWs.

For the co-doped NWs (Figure 5.13(b)), in our experiment, the Raman active modes are found to be prominent for the larger diameter (∼100-200 nm) NWs. The 4 peaks at 128, 170, 212, 416 cm^{-1} can be assigned as the longitudinal-optical (A_1) phonon modes A_1-1, A_1-2, A_1-3 and A_1-4, respectively [69]. The broad nature of the A_1-1 peak clearly indicates the presence of A_1-2 mode around 170 cm^{-1} in the spectra. The subsequent five peaks situated at 269, 326, 348, 499 and 598 cm^{-1} are related to the transverse-optical (E) phonon modes [70]. Some of the Raman peaks are absent here may be due to the higher local stress in the NWs and existence of point defect in the co-doped NWs [71]. Here, the spectra reported is for the parallel polarization configuration as the sample is polycrystalline. Therefore, it is expected that intensity of A_1 modes will not reduce significantly for cross polarization configuration too [66]. However, the peak positions are found to be diameter independent.

Bi-O1 vibrational peak at 130 cm^{-1} (for 200 nm co-doped NWs) is responsible for the magnetoelectric coupling in the samples. This Bi-O1 peak (A_1-1 mode) is found to

shift towards the lower frequency as the diameter of the NWs increases, which might be due to the change of force constant in the co-doped NWs because of the micro-structural changes related to doping [12]. Moreover, the broadening of the peaks is also observed with the decrease in the diameter of the NWs. The peak intensity of 200 and 150 nm NWs are almost equal but the peak intensity decreases gradually with further decrease in the diameter of the NWs is mainly due to the smaller physical dimension of the scattering crystalline NWs. The gradual decrease of the peak intensity (lowest for 18 nm NWs) indicates the suppression in the contribution of the Bi-O1 vibrational mode, probably due to the more lattice distortion or increased coupling between the ferroelectric and magnetic order parameters due to the quantum confinement effect [12]. Inset of Fig 5.13(b) shows the thermal effects on the Raman spectra of 18 nm co-doped NWs observed at 10 and 6 mW laser power. The laser heating is expected to increase the width of the Raman modes as observed in this study. Laser heating occurs during the energy transfers from the excited electron to lattice via electron-phonon scattering. But no signature of bond weakening is observed in our experiment with the application of high concentration excited electrons on the co-doped NWs. The increase in intensity of Raman modes with higher laser power is because of the more photon flux.

5.3.2.3 Magnetic properties of $Bi_{0.9}Pr_{0.1}Fe_{0.9}Cr_{0.1}O_3$ nanowires

Figure 5.14(a) shows the room temperature hysteresis (M-H) loops of the different diameters co-doped BFO NWs. The magnetic signal of the aligned arrays of co-doped BFO NWs is obtained after subtracting the diamagnetic response of the AAO template. It is observed that all the co-doped BFO NWs exhibit RTFM. Interestingly, magnetic response is found to enhance with decrease in the diameter of the BFO NWs. The maximum saturation magnetization (M_S) of 0.57 emu/g has been obtained for the 18 nm diameter NWs. Fig 5.14(b) shows the M-H loops for the undoped and co-doped

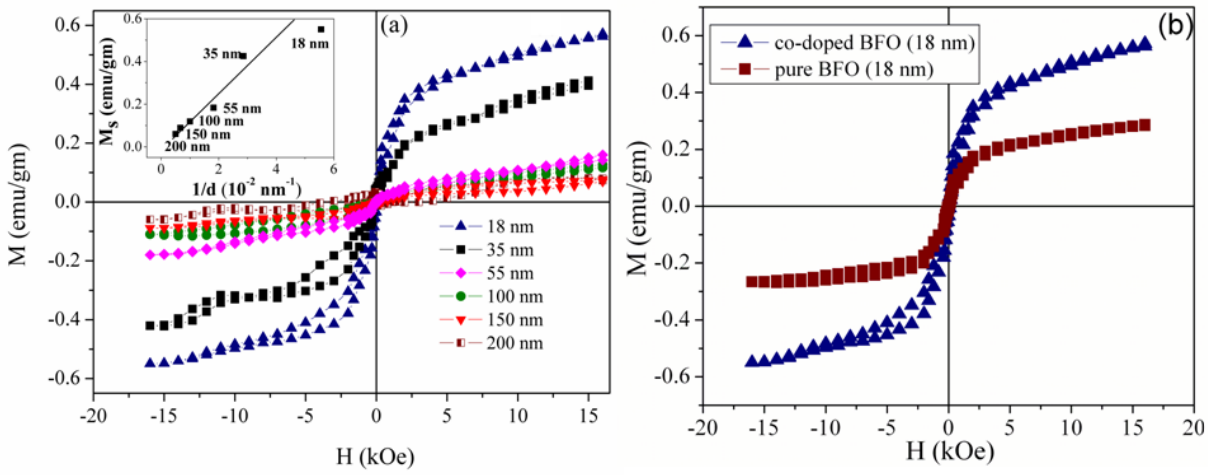

Figure 5.14: (a) Diameter dependent variation of the hysteresis loops of the co-doped BFO NWs measured at 300 K. The inset of (a) shows the change in the values of saturation magnetization of the co-doped BFO NWs as a function of 1/d (surface to volume ratio). (b) Hysteresis loops of the 18 nm diameter undoped and co-doped BFO NWs measured at 300 K.

18 nm diameter BFO NWs for a comparison. Significant enhancement of the magnetic signal of the doped NWs is evident from Figure 5.14(b).

Between, 200 to 55 nm of diameter the magnetization increases very insignificantly with the decrease of the NWs diameter. The variation of M_S with diameter of the NWs is shown in the inset of Fig 5.14(a), which demonstrate the effect of quantum confinement on magnetization. The diameter dependent variation of magnetization, coercive field and remanence in co-doped BFO NWs is summarized in Table 5.3.

The origin of the enhanced ferromagnetic signal from the Pr-Cr co-doped BFO NWs can be demonstrated based on the following discussions. Here, replacing Bi with Pr ion and Fe with Cr ion changes the canting angle and increases the degree of the distortion resulting in a smaller bond angle of antiferromagnetic Fe-O-Fe chain of spins leading to enhanced magnetization, might be one of the significant reason behind strong ferromagnetic property in the co-doped NWs compared to the undoped BFO samples

Table 5.3: The diameter dependent variation of remanant, coercive field and magnetization in co-doped BFO NWs.

Diameter of NWs (nm)	Remanant magnetization (memu/g)	Coercive field (Oe)	Magnetization at 15 kOe (memu/g)
18	19.2	50	570
35	20.1	200	410
55	4.5	45	180
100	3.2	160	127
150	4.0	240	89
200	15	330	59

[5, 72]. Doping of Pr ion in BFO is found to increase its magnetization [5]. Furthermore, the $3d^{+3}$ for Cr^{+3} ions with S = 3/2 present in the doped BFO NWs (as indicated by XPS study) can also introduce an effective magnetic moment of $\sim$3.87 μ_B, which can introduce local FM ordering at the dopant ion site and introduce a net moment through superexchange [22, 73]. It is known that the increase in the FM in BFO-based materials sometimes attributed to the existence of double exchange interaction between Fe^{+2} and Fe^{+3} ions through oxygen [24, 74]. However, in our experiment, XPS study indicates that only Fe^{+3} ion is present in the samples, hence the contribution of the Fe^{+2} ions to FM could be neglected here. In BFO, magnetic ions are coupled ferromagnetically within the (111) planes and anti-ferromagnetically between adjacent planes. Nanostructures of antiferromagnetic BFO show magnetic moment mainly due to the incomplete magnetic compensations between these planes. This incomplete magnetic orderings in nanostructures occur as the long-range antiferromagnetic order is frequently interrupted

at the grain surfaces [75]. Hence, the weak FM order in the co- doped BFO NWs has been ascribed to the size effect [3]. This work presents the direct evidence of the size effect on the magnetic order, which is antiferromagnetic in bulk BFO, due to the complicated spiral spin structure of wavelength 62 nm. Here, the increase of the magnetic signature in the NWs with the decrease of the diameter agrees well with the reports on the thickness dependence magnetization in BFO thin films [75] and size dependent magnetization of BFO nanoparticles [12]. With decrease of diameter in the NWs, the surface to volume ratio increases which enhances the effect of the antiferromagnetic-order interruption at the grain surfaces and thus the magnetization increases remarkably [12, 22]. It is believed that the uncompensated ferromagnetic surface spins of the NWs increases with the increase of their surface to volume ratio leading to enhance FM in the quantum confined structures. According to the Néel model [76, 77] in case of single domain antiferromagnetic particles susceptibility is expected to scale as $\sim 1/d$ (surface to volume ratio). Inset of Fig 5.14(a) shows a plot of the magnetization as a function of $1/d$ at an applied field of 15 kOe. Magnetization of the NWs with diameter 35 to 200 nm shows linear behaviour with $1/d$ indicating that the Néel model is applicable here. Therefore except the NWs with 18 nm diameter others can be modelled as the superposition of ferromagnetic surface/shell and an antiferromagnetic core. But the enhanced magnetization in 18 nm diameter NWs can not be explained with this model. The large magnetization in the NWs of 18 nm diameter might be a combination of structural distortion, large surface to volume ratio, higher magnetic anisotropy due to strain [78] and a strong interaction between lattices and spin [79]. Furthermore, in such quantum confined structures there is a possibility of the appearance of the Fe^{+2} ions in the NWs during the high temperature annealing leading to huge increase of the saturation magnetization [74].

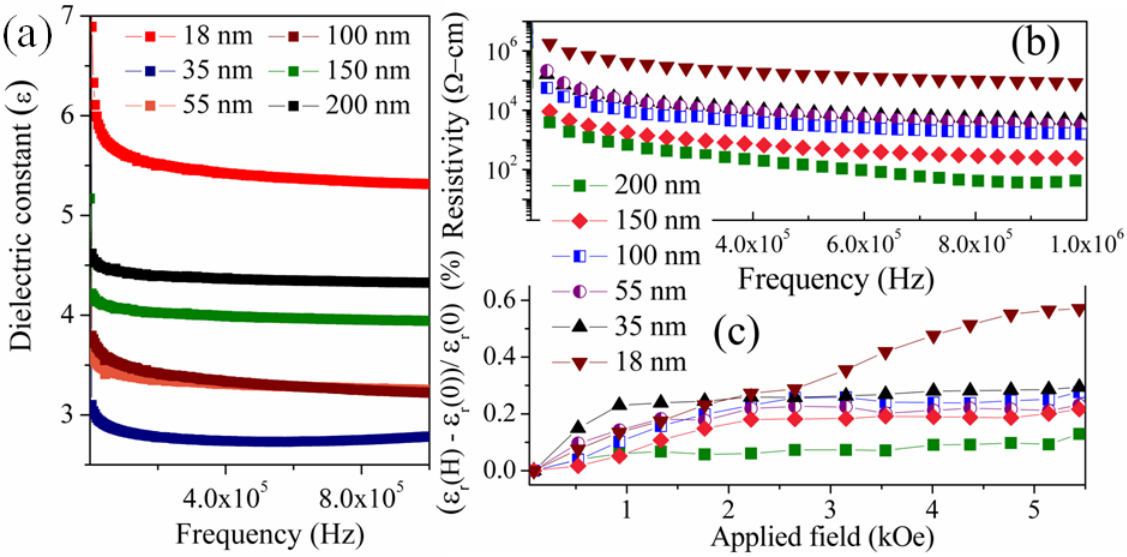

Figure 5.15: Frequency dependence of the dielectric constant (a) and resistivity (b) of the different diameter co-doped BFO NWs. (c) Magnetic field-induced change in the dielectric constant in the different diameter co-doped BFO NWs measured at frequency of 1 kHz at room-temperature.

5.3.2.4 Magnetodielectric effect in $Bi_{0.9}Pr_{0.1}Fe_{0.9}Cr_{0.1}O_3$ nanowires

Figure 5.15(a) shows the variation of the dielectric constant (ε) of the co-doped BFO NWs grown in AAO template, measured at 10^2-10^6 Hz frequency range at RT. In case of NWs with 35 to 200 nm diameter ranges, ε decreases with the decrease of the diameter, which is also observed in case of thin films [80]. Here, the 18 nm diameter NWs exhibit maximum ε value compare to others. It can be explained from the grain or grain boundary phase induced polarization which occurs due to the obstruction of charge carriers at the grain boundaries [16]. It is observed that when the diameter of the NWs decreases below a critical value there is a possibility of the appearance of mixed phases or the phase transition can take place, which leads to a build up of charges at the interface resulting the large polarization and subsequently high dielectric constant. Resistivity plot (Fig 5.15(b) of the NWs samples indicates that the resistivity of the NWs increases with the decrease of the diameter. High resistivity and the grain boundary scattering effect in

the NWs give rise to the high Magnetodielectric effect, expressed by $[\varepsilon_r(\mathrm{H})\text{-}\varepsilon_r(0)]/\varepsilon_r(0)$. Fig 5.15(c) shows the RT magnetic field dependence of the magnetodielectric (MD) effect at the frequency (f) of 1 kHz for all of the NWs. Here, the 18 nm diameter NWs shows maximum magnetoelectric coupling. The NWs with diameter between 35 to 200 nm exhibits enhanced magnetoelectric coupling with the decrease of the diameter of the NWs.

5.3.3 Conclusion

In summary, undoped, Pr and Cr doped and Pr-Cr co-doped BFO NTs are successfully fabricated within the pores of the AAO template by a facile wet chemical liquid phase deposition template assisted route. High aspect ratio NTs having very smooth wall surface with uniform outer diameter of ∼250 nm and wall thickness of ∼50 nm are synthesized. The XRD study confirms the formation of single phase polycrystalline NTs with a perovskite type structure. The PFM studies confirm the ferroelectric nature of all the doped BFO NTs. Substantial improvement in the ferroelectric property is observed in the $Pr_{0.1}Cr_{0.1}$BFO NTs with high electrical polarization and low coercive electric field, which might be attributed to the reduction of the concentration of oxygen vacancies. In the co-doped BFO NTs, polarization could be easily tuned by the application of magnetic field. It is found that the dielectric properties are enhanced by Pr substitution in BFO NTs, where the ε is increased by three orders of magnitude than that of the undoped BFO NTs at 621 Hz. Significant enhancement in the magnetodielectric behavior of the $Pr_{0.1}Cr_{0.1}$BFO NTs is also observed, which signifies the magnetoelectric coupling. The $Pr_{0.1}Cr_{0.1}$BFO NTs also exhibits the substantial increase in the ferromagnetic properties, which is attributed to the structural distortion of the spiral spin induced by the large size Pr ion substitution in A site and the strong coupling interaction between the Fe^{+3} and

Cr^{+3} ions. The study reveals that the co-doped BFO NTs exhibit enhanced ferroelectric, magnetoelectric and ferromagnetic properties, which makes it more suitable for device applications.

Along with better multiferroic properties, undoped and Pr-Cr co-doped BFO NTs also show better PV effects over the singly doped NTs under dark condition whereas, the Pr-doped BFO NTs is found to exhibit highest photosensitivity by showing highest value of photocurrent under white-light illumination. Pr-doped BFO NTs is characterized by highest V_{oc} ∼0.21 V, I_{sc} ∼0.89 nA and $\eta \sim 0.5$ % values amongst the other NTs under illumination. The PV property of the Cr-doped BFO NTs is the weakest among all the NTs samples. For all NTs the values of photovoltaic efficiency is found to be enhanced by several orders of magnitude higher than the bulk BFO. In the doped NTs the switchable open-circuit photovoltage is reduced from the undoped BFO NTs. In principal, variation of the concentration and the mobility of the photoexcited carriers induced by metal-doping can contribute in the change of photocurrent and hence PV effects. The enhanced PV properties are because of the special nano-dimensional geometry of NTs, which can induce substantially large photocurrent. Experiments suggest that the BFO NTs are potential candidate for applications in photo-sensitive, energy-harvesting and memory devices.

Different diameter Pr-Cr co-doped BFO NWs are also fabricated in similar method to study the size effect on the physical properties of the NWs. Pore diameter of AAO template is varied to synthesize the NWs with diameter 18, 35, 55, 100, 150 and 200 nm. The XPS investigations confirm that oxygen vacancy related defects in BFO NWs is reduced significantly by Pr-Cr ion co-doping. All the NWs exhibit intense blue band edge light emission, where interesting blue shift of the band gap emission is observed because of the quantum confinement effects in the nanoscale dimension. The green emission of the co-doped BFO NWs is ascribed to the electronic transitions of Pr^{+3} ions. It is to

infer that the quantum confinement effect in large diameter NWs may be originated from the polycrystalline NWs, where the dimensions of some of the crystals are much smaller than the diameter of the NWs. The room temperature ferromagnetic signature of the NWs is found to improve with the decrease of the diameter of the NWs, which indicates that the quantum confinement effect (increase of the surface to volume ratio with the decrease of the NWs diameter) has significant influence on their magnetic properties. The magnetoelectric coupling in the NWs is found to enhance with the decrease in the diameter too.

References

[1] D. P. Dutta, O. D. Jayakumar, A. K. Tyagi, K. G. Girija, C. G. S. Pillaia, and G. Sharma, Nanoscale 2, 1149 (2010).

[2] X. Y. Zhang, C. W. Lai, X. Zhao, D. Y. Wang, and J. Y. Dai, Appl. Phys. Lett. 87, 143102 (2005).

[3] F. Gao, Y. Yuan, K. F. Wang, X. Y. Chen, F. Chen, J.-M. Liu, and Z. F. Ren, Appl. Phys. Lett. 89, 102506 (2006).

[4] Y. Du, Z. X. Cheng, S. X. Dou, D. J. Attard, and X. L. Wang, J. Appl. Phys. 109, 073903 (2011).

[5] B. Yu, M. Li, Z. Hu, L. Pei, D. Guo, X. Zhao, and S. Dong, Appl. Phys. Lett. 93, 182909 (2008).

[6] P. Uniyal, and K. L. Yadav, J. Phys.: Condens. Matter. 21, 405901 (2009).

[7] C. Lan, Y. Jiang, and S. Yang, J. Mater. Sci. 46, 734 (2011).

[8] Y. H. Lee, J. M. Wu, and C. H. Lai, Appl. Phys. Lett. 88, 042903 (2006).

[9] H. Naganuma, J. Miura, and S. Okamura, Appl. Phys. Lett. 93, 052901 (2008).

[10] Y. Du, Z. X. Cheng, S. X. Dou, M. Shahbazi, and X. L. Wang, Thin Solid Films 518, e5 (2010).

[11] P. Kharel, S. Talebi, B. Ramachandran, A. Dixit, V. M. Naik, M. B. Sahana, C. Sudakar, R. Naik, M. S. R. Rao and G. Lawes, J. Phys.: Condens. Matter 21, 036001 (2009).

[12] T.-J. Park, G. C. Papaefthymiou, A. J. Viescas, A. R. Moodenbaugh, and S. S.Wong, Nano Lett. 7, 766 (2007).

[13] D. H. Wang, W. C. Goh, M. Ning, and C. K. Ong, Appl. Phys. Lett. 88, 212907 (2006).

[14] Y. Noguchi, and M. Miyayama, Appl. Phys. Lett. 78, 1903 (2001).

[15] T. Kojima, T. Sakai, T. Watanabe, H. Fanakubo, K. Saito, and M.Osada, Appl. Phys. Lett. 80, 2746 (2002).

[16] Y. Chen, X. Y. Zhang, C. Vittoria, and V. G. Harris, Appl. Phys. Lett. 94, 102906 (2009).

[17] 36R. Nechache, C. V. Cojocaru, C. Harnagea, C. Nauenheim, M. Nicklaus, A. Ruediger, F. Rosei and A. Pignolet, Adv. Mater. 23, 17241729 (2011).

[18] H.W. Jang, A. Kumar, S. Denev, M. D. Biegalski, P. Maksymovych, C.W. Bark, C. T. Nelson, C. M. Folkman, S. H. Baek, N. Balke, C. M. Brooks, D. A. Tenne, D. G. Schlom, L. Q. Chen, X. Q. Pan, S.V. Kalinin, V. Gopalan and C. B. Eom, Phys. Rev. Lett. 104, 197601 (2010).

[19] K. Vasudevan, K. A. Bogle, A. Kumar, S. Jesse, R. Magaraggia, R. Stamps, S. B. Ogale, H. S. Potdar and V. Nagarajan, Appl. Phys. Lett. 99, 252905 (2011).

[20] M. Li, M. Ning, Y. Ma, Q. Wu, and C. K. Ong, J. Phys. D: Appl. Phys. 40, 1603 (2007).

[21] T. Kimura, S. Kawamoto, I. Yamada, M. Azuma, M. Takano, and Y. Tokura, Phys. Rev. B 67, 180401 (2003).

[22] Z. X. Cheng, X. L. Wang, Y. Du, and S. X. Dou, J. Phys. D: Appl. Phys. 43, 242001 (2010).

[23] B. -C. Luo, C. -L Chen, and K. -X. Jin, Solid State Communications 151, 712 (2011).

[24] J. Wang, A. Scholl, H. Zheng, S. B. Ogale, D. Viehland, D. G. Schlom, N. A. Spaldin, K. M. Rabe, M. Wuttig, L. Mohaddes, J. Neaton, U. Waghmare, T. Zhao, and R. Ramesh, Science 307, 1203 (2005).

[25] J. Wang et al., Science 299, 1719 (2003).

[26] W. Eerenstein et al., Nature 442, 759 (2006).

[27] M. Fiebig et al., Nature 419, 815 (2002).

[28] J. F. Ihlefeld et al., Appl. Phys. Lett. 92, 142908 (2008).

[29] T. Choi et al., Science, 324, 63 (2009).

[30] S. Y. Yang et al., Nat. Nanotechnol., 5, 143 (2010).

[31] M. Alexe, and D. Hesse, Nat. Commun. 2, 256 (2011).

[32] L. Pintilie et al., J. Appl. Phys. 101, 064109 (2007).

[33] J. F. Scott, and C. A. Araujo, Science 246, 1400 (1989).

[34] R. Nechache et al., Appl. Phys. Lett. 98, 202902 (2011).

[35] K. Yao et al., Appl. Phys. Lett. 87, 212906 (2005).

[36] R. Das et al., J. Appl. Phys. 111, 104115 (2012).

[37] J. K. Kim et al., Appl. Phys. Lett. 88, 132901 (2006).

[38] B. Chen et al., Nanotechnology, 22, 195201 (2011).

[39] W. Ji et al., Adv. Mater. 22, 1763 (2010).

[40] X. Yu et al., Solid State communication 149, 711 (2009).

[41] X. Lu et al., Adv. Funct. Mater. 20, 509 (2010)

[42] A. Kumar et al., Phys. Status Solidi A, (DOI 10.1002/pssa.201228154)

[43] R. Jarrier et al., Phys. Rev. B 85, 184104 (2012).

[44] T. L. Qu et al., Appl. Phys. Lett. 98, 173507 (2011).

[45] Y. Zang et al., Appl. Phys. Lett. 99, 132904 (2011).

[46] S. Y. Yang et al., Appl. Phys. Lett. 95, 062909 (2009).

[47] M. Ichiki et al., Appl. Phys. Lett. 87, 222903 (2005).

[48] M. Qin et al., Appl. Phys. Lett. 95, 022912 (2009).

[49] Y.-Q. Kang, M.-S. Cao, J. Yuan and X.-L. Shi, Mater. Lett., 63, 13441346 (2009).

[50] S. M. Selbach, T. Tybell, M.-A. Einarsrud, and T. Grande, Chem. Mater., 19, 6478 (2007).

[51] G. G. Khan, R. Das, N. Mukherjee and K. Mandal, Physica Status Solidi - RRL, 6, 312 (2012).

[52] A. J. Hauser, J. Zhang, L. Mier, R. A. Ricciardo, P. M. Woodward, T. L. Gustafson, L. J. Brillson and F. Y. Yang, Appl. Phys. Lett. 92, 222901 (2008).

[53] X. Chen, H. Zhang, T. Wang, F. Wang, W. Shi, Phys. Status Solidi A 209, 1456-1460 (2012).

[54] W. B. Luo, J. Zhu, Y. R. Li, X. P. Wang, D. Zhao, J. Xiong, and Y. Zhang, Appl. Phys. Lett. 91, 082501 (2007).

[55] S-W. Chen, C-C. Lee, M-T. Chen and J-M. Wu, Nanotechnology 22, 115605 (2011).

[56] F. Yan, M-O Lai, L Lu, and T-J Zhu, J. Phys. Chem. C, 114, 6994-6998 (2010).

[57] R. E. Kirby, E. L. Garwin, F. K. King, A. R. Nyaiesh, J. Appl. Phys. 62, 1400 (1987).

[58] W. Xiao, K. Xie, Q. Guo and E G Wang, J. Phys.: Condens. Matter 15, 1155 (2003).

[59] Y. Uwamino, I. Ishizuka, H. Yamatera, J. Electron. Spectrosc. Relat. Phenom. 34, 67-78 (1984).

[60] D. Wolfframma, M. Ratzke, M. Kappaa, M. J. Montenegro, M. Dbeli, T. Lippert, J. Reif, Materials Science and Engineering B 109, 24-29 (2004).

[61] L. Fang, J. Liu, S. Ju, F. Zheng, W Dong, and M. Shenc Appl. Phys. Lett. 97, 242501 (2010).

[62] L. R Shah, B. Ali, H. Zhu, W.G. Wang,Y. Q. Song, H W Zhang, S I Shah and J Q Xiao J. Phys.: Condens. Matter 21, 486004 (2009).

[63] Y. B. Li, M. J. Zhenga, and L. Ma, Appl. Phys. Lett. 91, 073109 (2007).

[64] G Lakshminarayana, J. Qiu, M G Brik and I V Kityk, J. Phys. D: Appl. Phys. 41, 175106 (2008). 31.

[65] Y. Liu, J. Ren,Y. Tong, T. Wang, W. Xu, and G. Chen, J. Am. Ceram. Soc. 95, 41 (2012).

[66] H. Fukumura, H. Harima, K. Kisoda, M. Tamada, Y. Noguchi and M. Miyayama, J. Magn. Magn. Mater. 310, e367 (2007).

[67] D. Kothari, V. R. Reddy, V.G. Sathe, A. Gupta, A. Banerjee, A.M. Awasthi, J. Magn. Magn. Mater. 320, 548552 (2008).

[68] A. Jaiswal, R. Das, K. Vivekanand, P. M. Abraham, S. Adyanthaya, P. Poddar, J. Phys. Chem. C, 114, 2108-2115 (2010).

[69] M. K. Singh, H. M. Jang, S. Ryu, and M.-H Jo, Appl. Phys. Lett. 88, 042907 (2006).

[70] R. Guo, L. Fang, W. Dong, F. Zheng, and M. Shen, J. Phys. Chem. C, 114, 21390 (2010).

[71] J.M.Calderon-Moreno, M.Yoshimura, Solid State Ionics, 154-155, 125 (2002).

[72] Jiagang Wu and John Wang, J. Appl. Phys. 106, 054115 (2009).

[73] J. B. Goodenough, Phys. Rev. 100, 564 (1955).

[74] Yao Wang, Qing-hui Jiang, Hong-cai He, and Ce-Wen Nan, Appl. Phys. Lett. 88, 142503 (2006).

[75] F. Huang, X. Lu, W. Lin, Y. Kan, J. Zhang, Q. Chen, Z. Wang, L. Li and J. Zhu, Appl. Phys. Lett. 97, 222901 (2010).

[76] Neel in Low Temperature Ph & s, edited by C. Dewitt, B. Dreyfus, and P. b. DeGennes p. 411 (Gordon and Beach, London, 1962).

[77] J. T. Richardson, D. I. Yiagas, B. Turk, K. Forster and M. V. Twigg J. Appl. Phys. 70 6977 (1991).

[78] G. C. Papaefthymiou, J. Magn. Magn. Mater. 272 e1227 (2004).

[79] Ching-Jung Cheng, Chengliang Lu, Zuhuang Chen, Lu You, Lang Chen, Junling Wang, and Tom Wu, Appl. Phys. Lett. 98, 242502 (2011).

[80] L. Pálová, P. Chandra, and K. M. Rabe, Phys. Rev. B 76, 014112 (2007).

6 Conclusion and Scope for Future Study

In this thesis, we have investigated multiferroic properties of both bulk and nanostructured (thin film, nanowires and nanotubes) $BiFeO_3$ compounds. We have also studied the role of different magnetic ions such as transitional metal (TM) and rare-earth (RE) ions doping on the magnetic, ferroelectric, dielectric and magnetodielectric properties of $BiFeO_3$. We have found that R3c structure of $BiFeO_3$ remain unchanged after doping Ba and Gd in the ceramic. Ba doping enhances the magnetic properties dramatically but the ferroelectric properties are weak in Ba doped $BiFeO_3$ ceramics. However, Ba and Gd co-doped samples are better insulating and saturated P-E hysteresis loop is observed in these materials. Detail Rietveld and XPS study show that the enhancement in the magnetic properties is mainly influenced by the modification in the bond length and bond angle in the $BiFeO_3$ structure. Ferroelectric properties enhances due to the reduction in the oxygen vacancies. Magnetodielectric properties also show significant increment in the co-doped samples. Compare to the Ba doped bulk samples Ba doped thin film shows better ferromagnetic behaviour and the thin film shows no leakage nature. Ferroelectic properties of the films depend on the crystallization direction and surface morphology

which can be controlled by the substrate temperature during film deposition. However, all these properties can be tailored by changing the thickness of the films. Though the film with minimum thickness (18 nm) shows better magnetic properties, electrical properties is very difficult to measure here due to the presence of dead layer. One should have eliminate the effect of dead layers to get best FE and magnetic behaviour in the same film. Finally, we studied one-dimensional nanostructures (such as nanowires (NWs) and nanotubes (NTs)) of $BiFeO_3$. Effect of Pr and Cr ions doping on the magnetic, ferroelectric, dielectric and magnetodielectric properties of $BiFeO_3$ NTs is also studied. co-doped $BiFeO_3$ NTs shows photovoltaic effect. Similar with the ceramics here also co-doping enhances the multiferroic properties. Co-doped NWs shows maximum band gap compared to bulk $BiFeO_3$. Apart from multiferroic properties In case of nanowires also magnetic and ferroelectric properties highly depend on the diameter of the NWs. However, magnetic and ferroelectric properties enhances when the diameter of the NWs is reduced. Our study gives a proper comparison of the multiferroic properties in bulk and nanostructures and the effect of doping and size modulation in the material.

Scope for future study :

In this thesis, so far we have studied effect of Ba^{2+} and Gd^{3+} doping replacing Bi^{3+} and Fe^{3+} in the structure, respectively. We have seen that co-doping enhances all the multiferroic properties. It would be interesting to study the effect of trivalent or tetravalent ion doping on Bi site. Doping Ba^{2+} enhances the probability of oxygen vacancy formation in the structure as Fe is in 3+ state in all the samples. So keeping Gd fix in the Fe-site, we can vary A-site doing ions having different valance state to study the ferroelectric and conductivity properties of $BiFeO_3$.

From the present study it is clear that thin film serves better magnetic properties.

Besides that Ba doping also enhances magnetic properties keeping the crystal structure same. To achieve a noticeable ferroelectric properties, one can prepare a ferromagnetic layer (suppose Ba-doped $BiFeO_3$) on a substrate, then deposit a ferroelectric layer ($BaTiO_3$ or PZT) on it and then again deposit another ferromagnetic layer above it and study the composite multi-layered system and the magnetoelectric coupling in the composite system.

Except the enhanced magnetoelectric properties in the $BiFeO_3$ NWs and NTs, it also shows interesting optical and photovoltaic properties. In recent years, magnetic and ferroelectric properties of $BiFeO_3$ have been studied intensively. However, very less attention has been paid to its optical properties, especially in practical aspects. So a detailed study on the optical properties on $BiFeO_3$ NWs and NTs may establish $BiFeO_3$ as a promising material for the use as an optical filter and as a part of communication devices.